University of Kentucky
UKnowledge

University of Kentucky Doctoral Dissertations

Graduate School

2010

CHARACTERIZATION AND OPTIMIZATION OF MICROELECTRODE ARRAYS FOR GLUTAMATE MEASUREMENTS IN THE RAT HIPPOCAMPUS

Pooja Mahendra Talauliker
University of Kentucky, pmtala2@uky.edu

Right click to open a feedback form in a new tab to let us know how this document benefits you.

Recommended Citation

Talauliker, Pooja Mahendra, "CHARACTERIZATION AND OPTIMIZATION OF MICROELECTRODE ARRAYS FOR GLUTAMATE MEASUREMENTS IN THE RAT HIPPOCAMPUS" (2010). *University of Kentucky Doctoral Dissertations*. 759.
https://uknowledge.uky.edu/gradschool_diss/759

This Dissertation is brought to you for free and open access by the Graduate School at UKnowledge. It has been accepted for inclusion in University of Kentucky Doctoral Dissertations by an authorized administrator of UKnowledge. For more information, please contact UKnowledge@lsv.uky.edu.

ABSTRACT OF DISSERTATION

Pooja Mahendra Talauliker

The Graduate School

University of Kentucky

2010

CHARACTERIZATION AND OPTIMIZATION OF MICROELECTRODE ARRAYS FOR GLUTAMATE MEASUREMENTS IN THE RAT HIPPOCAMPUS

ABSTRACT OF DISSERTATION

A dissertation submitted in partial fulfillment of the
requirements for the degree of Doctor of Philosophy in the
College of Medicine
at the University of Kentucky

By
Pooja Mahendra Talauliker

Lexington, Kentucky

Director: Dr. Greg A. Gerhardt, Professor of Anatomy and Neurobiology

Lexington, Kentucky

2010

Copyright © Pooja Mahendra Talauliker 2010

ABSTRACT OF DISSERTATION

CHARACTERIZATION AND OPTIMIZATION OF MICROELECTRODE ARRAYS FOR GLUTAMATE MEASUREMENTS IN THE RAT HIPPOCAMPUS

An overarching goal of the Gerhardt laboratory is the development of an implantable neural device that allows for long-term glutamate recordings in the hippocampus. Proper L-glutamate regulation is essential for hippocampal function, while glutamate dysregulation is implicated in many neurodegenerative diseases. Direct evidence for subregional glutamate regulation is lacking in previous *in vivo* studies because of limitations in the spatio-temporal resolution of conventional experimental techniques. We used novel enzyme-coated microelectrode arrays (MEAs) for rapid measurements (2Hz) of extracellular glutamate in urethane-anesthetized rats. Potassium-evoked glutamate release was highest in the cornu ammonis 1 (CA1) subregion and lowest in the cornu ammonis 3 (CA3). In the dentate gyrus (DG), evoked-glutamate release was diminished at a higher potassium concentration but demonstrated faster release kinetics. These studies are the first to show subregion specific regulation of glutamate release in the hippocampus.

To allow for *in vivo* glutamate measurements in awake rats, we have adapted our MEAs for chronic use. Resting glutamate measurements were obtained up to six days post-implantation but recordings were unreliable at later time points. To determine the cause(s) for recording failure, a detailed investigation of MEA surface characteristics was conducted. Scanning electron microscopy and atomic force microscopy showed that PT sites have unique surface chemistry, a microwell geometry and nanometer-sized features, all of which appear to be favorable for high sensitivity recordings. Accordingly, studies were initiated to improve enzyme coatings using a computer-controlled microprinting system (Microfab Technologies, Plano, TX). Preliminary testing showed that microprinting allowed greater control over the coating process and produced MEAs that met our performance criteria.

Our final studies investigated the effects of chronic MEA implantation. Immunohistochemical analysis showed that the MEA produced minimal damage in the hippocampus at all time points from 1 day to 6 months. Additionally, tissue attachment to the MEA surface was minimal. Taken together with previous electrophysiology data supporting that MEAs are functional up to six months, these studies established that our chronic MEAs technology is capable of maintaining a brain-device interface that is both functional and biocompatible for extended periods of time.

KEYWORDS: Glutamate, Hippocampus, *In Vivo* Amperometry, Functional Biocompatibility, Brain-Microelectrode Interface

Pooja Mahendra Talauliker

01/28/2010

CHARACTERIZATION AND OPTIMIZATION OF MICROELECTRODE ARRAYS FOR GLUTAMATE MEASUREMENTS IN THE RAT HIPPOCAMPUS

By

Pooja Mahendra Talauliker

Greg A. Gerhardt
Director of Dissertation

Jane Joseph
Director of Graduate Studies

01/28/10

RULES FOR THE USE OF DISSERTATIONS

Unpublished dissertations submitted for the Doctor’s degree and deposited in the University of Kentucky Library are as a rule open for inspection, but are to be used only with due regard to the rights of the authors. Bibliographical references may be noted, but quotations or summaries of parts may be published only with the permission of the author, and with the usual scholarly acknowledgments.

Extensive copying or publication of the dissertation in whole or in part also requires the consent of the Dean of the Graduate School of the University of Kentucky.

A library that borrows this dissertation for use by its patrons is expected to secure the signature of each user.

Name	Date

DISSERTATION

Pooja Mahendra Talauliker

The Graduate School

University of Kentucky

2010

CHARACTERIZATION AND OPTIMIZATION OF MICROELECTRODE ARRAYS GLUTAMATE MEASUREMENTS IN THE RAT HIPPOCAMPUS

DISSERTATION

A dissertation submitted in partial fulfillment of the
requirements for the degree of Doctor of Philosophy in the
College of Medicine
at the University of Kentucky

By
Pooja Mahendra Talauliker

Lexington, Kentucky

Director: Dr. Greg A. Gerhardt, Professor of Anatomy and Neurobiology

Lexington, Kentucky

2010

Copyright © Pooja Mahendra Talauliker 2010

"There are two lasting bequests we can give our children.
One is roots, the other is wings." ~ Hodding Carter

Dedicated to my parents, Usha and Mahendra Talauliker

ACKNOWLEDGEMENTS

कायेन वाचा मनसेन्द्रियैर्वा बुद्धयात्मना वा प्रकृतेः स्वभावात् ।
करोमि यद्यत्सकलं परस्मै गुरुवरायेति समर्पयामि ॥

All I have accomplished, I offer to you, the One who guides us all.

I take this opportunity to recognize the support and guidance of several individuals who made the completion of my dissertation a reality. First, I would like to thank my Dissertation Advisor, Dr. Greg Gerhardt for providing guidance and the opportunity to pursue my graduate education in a stimulating research environment. I am also thankful for the honest feedback I received throughout my graduate training from Theresa Thomas and for her unswerving faith in me. Peter Huettl, Francois Pomerleau and Jorge Quintero were always willing to facilitate my learning experience and their constructive input has helped me develop my scientific writing skills. I thank Dr. Ingrid Strömberg for the opportunity to conduct exciting collaborative research. I also thank Drs. Bruce Maley, Randy Hunter, Chris Bjornsson and William Shain for taking the time to teach me about immunohistochemical techniques. The team of scientists at Microfab: David Silva, Patrick Cooley, Mark Christison, Hans-Jochen Trost and Paul Watson, provided much-needed technical support and were always committed to advancing my work with the Jetlab microprinter. Thanks to Larry Rice for providing training on electron microscopy and atomic force microscopy. My students, Edwin Apenbrinck, Janelle Geddes, Emily Cottrell, Kawthar Suleiman and Jacob Mason contributed to my research productivity. Finally, I thank my

Dissertation Advisory Committee and Outside Examiner: Drs. Wayne Cass, James Geddes, Paul Glaser, Kurt Hauser and Todd Hastings. Their mentorship facilitated the development of my research projects, my professional growth and the quality of this dissertation.

The unwavering support of my parents has always given me the confidence to dream big and pursue my ambitions, even if they take me far away from home. I thank my husband Prasad for his understanding, and emotional and intellectual support. I also thank my brother Raaj and the close friends who have shown support for my professional and personal endeavors over the years: Parul, Preeti, Aashish and Maitreyi. Lastly, I thank Drs. Gerry Chader, Richard Rovinelli and Jennifer Brueckner for their mentorship and for expecting the best of me in all my pursuits.

TABLE OF CONTENTS

ACKNOWLEDGEMENTS……………………………………………………………...iii
LIST OF TABLES………………………………………………………………….x
LIST OF FIGURES……………………………………………………………....xi
Chapter One: Introduction…………………………………………………….....1
1.1 Neuroanatomy and Physiology of the Hippocampus………………………...1
1.2 Glutamate Regulation and Hippocampal Function…………………….……...5
1.3 Glutamate Neurotransmission in the Aging Hippocampus……….………….8
1.4 Glutamate Dysregulation in Hippocampal Disease………….………......10
1.4.1 Alzheimer's disease……….…………………………………………….....10
1.4.2 Schizophrenia………………………………………………………………12
1.5 Rapid Glutamate Measurements using Microelectrode Arrays coupled with *In Vivo* Amperometry…………………………………………………..........13
1.6 Thesis Outline…………………………………………………………………16

Chapter Two: Materials and Methods……………………………………………….24
2.1 The Fischer 344 Rat as a Model for Studies of Human Hippocampal Function…………………………………………………………………………….24
2.2 Ethical Standards for the Care and Use of Animals…………………………25
2.3 Surgery Procedures…………………………………………………………..25
2.3.1 Studies in Anesthetized Animals……………………………….……25
2.3.2 Studies in Unanesthetized Animals……………………………………….26
2.4 Euthanasia and Tissue Recovery……………………………………………..28
2.5 *In Vivo* Amperometry Using Ceramic-based MEAs…………………………28
2.5.1 MEA Design and Fabrication……………………………….……......28
2.5.2 Amperometric Recording Instrumentation………………….…………29
2.6 Glutamate Measurements in Anesthetized Rats……………………………29
2.6.1 MEA Preparation…………………………………………………………29
2.6.2 *In Vitro* Calibration and MEA Selection Criteria…………………………30
2.6.3 Experimental Setup for Glutamate Recordings…….……………………31
2.6.4 Resting Glutamate Measurements…………………………..………32

2.6.5 Stimulus Evoked Glutamate Overflow……………………………………32
2.6.6 Clearance of Locally Applied Glutamate……………………………....33
2.6.7 Depth Profile Investigations of Glutamate Neurotransmission…………33
2.6.8 MEA Placement Verification……………………………………………34
2.7 Glutamate Measurements in Unanesthetized Rats…………………………35
2.7.1 Chronic MEA/Cannula Assembly………………………………………35
2.7.2 In Vitro Calibration and MEA Selection Criteria…………………………35
2.7.3 Experimental Setup for Glutamate Recordings…………………………35
2.7.4 Resting Glutamate Measurements……………………………………..36
2.7.5 Data Analysis…………………………………………………………..36
2.8 Scanning Electron Microscopy Studies of MEAs……………………………36
2.9 Atomic Force Microscopy Studies of MEAs…………………………………..37
2.10 Magnetic Resonance Imaging of the Brain – MEA Interface……………...38
2.11 Inkjet-based Microprinting Technology for Application of Enzymes on MEA Recording Sites……………………………………………………………………39
2.11.1 Principles of Piezoelectric Inkjet Printing……………………………..39
2.11.2 Preparation of Printing Assembly……………………………………..40
2.11.3 *In Vitro* Testing of Coated MEAs………………………………………40
2.12 Immunohistochemical Analysis of Brain Tissue and MEAs following Chronic Implantation……………………………………………………………...40
2.13 Drugs and Reagents…………………………………………………………..42

Chapter Three: Real-time Measurements of Glutamate Neurotransmission in the Hippocampal Trisynaptic Pathway of F344 Rats…………………………………..55
3.1 Introduction…………………………………………………………………55
3.2 Materials and Methods………………………………………………………59
3.3 Results (I): Glutamate Recordings in the Anesthetized Rat Hippocampus.59
3.3.1 Resting Levels of Extracellular Glutamate in the Hippocampal Trisynaptic Circuit…………………………………………………………………….59
3.3.2 KCl-evoked Glutamate Release in the Rat Hippocampus……………...60

3.3.3 Rise Time of Glutamate Signals following KCl Stimulation in Hippocampal Subregions……………………………………………………………61
3.3.4 Glutamate Clearance Capacity in Subregions of the Rat Hippocampus……………………………………………………………………62
3.3.5 Depth Profile of Resting Glutamate and Stimulus-evoked Glutamate Release in the Rat Hippocampus………………………………...…………...62
3.4 Discussion: Studies of Glutamate in the Anesthetized Rat Hippocampus..63
3.4.1 Resting Levels of Extracellular Glutamate are Similar throughout the Hippocampal Trisynaptic Circuit in Anesthetized Rats………………………...64
3.4.2 Capacity for Stimulus-evoked Glutamate Release is Different in Hippocampal Subregions……………………………………………………………64
3.4.3 Stimulus-evoked Glutamate Release is Faster in the DG Subregion…67
3.4.4 Rate of Glutamate Uptake is not Significantly Different in the Trisynaptic Circuit of Anesthetized rats……………………………………………………………68
3.5 Results (II): Glutamate Recordings in the Unanesthetized Rat Hippocampus……………………………………………………………………………68
3.5.1 Verification of Glutamate Signals in the CA1 Subregion of the Unanesthetized Rat Hippocampus……………………………………………68
3.5.2 Resting Levels of Extracellular Glutamate in the CA1 Subregion of the Unanesthetized Rat Hippocampus……………………………………………69
3.6 Summary of Glutamate Studies in the Unanesthetized Rat Hippocampus.69

Chapter Four: Surface Characterization and Topographical Analysis of MEAs..81
4.1 Introduction……………………………………………………………………81
4.2 Materials and Methods………………………………………………………….83
4.3 Results and Discussion………………………………………………………83
4.3.1 *In Vitro* Performance of W4 and S2 MEAs……………………………….83
4.3.2 Photolithography Produces Recording Sites with Microwell Geometry.84
4.3.3 Ceramic Topography is composed of Micro/nanoscale Surface Features………………………………………………………………………….85
4.3.4 Fabrication Errors and Defects from Photolithographic Processing…..86

4.3.5 Backscattered Electron Imaging (BSE) and Energy Dispersive Spectroscopy (EDS)……………………………………………………………………86
4.3.6 Platinum Sites are composed of Nanoscale Topographical Features...87
4.3.7 Machined Ceramic Faces are dominated by Nanometer–Sized Microgrooves……………………………………………………………………………90
4.4 Summary and Conclusion……………………………………………………90

Chapter Five: Investigations of Microprinting Technology as a Novel Protein - Coating Tool for MEA Recording Surfaces………………………………………..106
5.1 Introduction…………………………………………………………………..106
5.2 Materials and Methods……………………………………………………...106
5.3 Results and Discussion I: Nanoject Microplotter System for Application of Enzyme Coatings on MEAs……………………………………………………107
5.3.1 Coating Methodology for W4-MEAs……………………………………..107
5.3.2 Challenges of Coating Procedure………………………………………..108
5.4 Results and Discussion II: Jetlab® Microprinting Station for Application of Enzyme Coatings on MEAs……………………………………………………108
5.4.1 Calibration of Viewing Cameras and Translation Stages……………..109
5.4.2 Characterization of Pulse Parameters for Formation of Droplets…….109
5.4.3 Drying Behavior of Droplets on a Ceramic Substrate…………………110
5.4.4 Automation of Coating Process…………………………………………..111
5.4.5 *In Vitro* Performance of Microprinted MEAs……………………………112
5.5 Conclusion…………………………………………………………………...112

Chapter Six: Characterization of Tissue Responses to Chronic MEA Implantation in the Hippocampus…………………………………………………………121
6.1 Introduction…………………………………………………………………..121
6.2 Materials and Methods………………………..…………………………...124
6.3 Results………………………………………………………………………..124
6.3.1 Post-surgery Magnetic Resonance Imaging (MRI)…………………….124
6.3.2 Cresyl Violet Staining……………………………………………………..125

6.3.3 GFAP and Iba1 Immunoreactivity……………………………………….125
6.3.4 Surface Characterization of Explanted MEAs………………………….128
6.4 Discussion……………………………………………………………………129
6.4.1 MEAs are Well-Tolerated in the Rat Hippocampus……………………130
6.4.2 Hippocampal Tissue Response to Chronic MEAs Demonstrates Overlapping Acute and Chronic Phases………………………………………130
6.4.3 Tissue Responses to Chronic MEAs is Different in the PFC and Hippocampus……………………………………………………………………..132
6.4.4 Chronic MEAs Produce Minimal Tissue Damage in the Rat Hippocampus……………………………………………………………………..134

Conclusions 148
Appendix: Custom Script for Jetlab Printing Trials 151
References 152
VITA 174

LIST OF TABLES

Table 2.1 Stereotaxic Coordinates for Hippocampal Subregions 54
Table 4.1 Pt Site Sensitivity for Hydrogen Peroxide 103
Table 4.2 Sample Roughness Analysis of Platinum Recording Sites 104
Table 4.3 Sample Roughness Analysis of Reverse Ceramic Surface 105

LIST OF FIGURES

Figure 1.1: Glutamate synapse.. 20
Figure 1.2: Hippocampal trisynaptic pathway. 21
Figure 1.3: Serial and parallel excitatory connections in the hippocampus. 22
Figure 2.1: MEA fabrication using photolithography 44
Figure 2.2: W4-MEA configured for neurotransmitter recordings in anesthetized and unanesthetized animals.. 46
Figure 2.3: W4 MEA configured for self-referenced glutamate measurements.. 47
Figure 2.4: Calibration of W4-MEAs.. 48
Figure 2.5: Signal characteristics for MEAs.. 49
Figure 2.6: Electrode placement verification in the rat hippocampus.................. 50
Figure 2.7: MEA surface imaging using scanning electron microscopy.............. 51
Figure 2.8: Basic properties of piezo-based inkjetting of solutions. 52
Figure 2.9: Schematic illustration of JetLab4 microprinting system. 53
Figure 3.1: Average extracellular levels of resting glutamate in subregions of the hippocampal trisynaptic circuit.. 71
Figure 3.2: Comparison of glutamate release capacity in subregions of the rat hippocampus following stimulation with 70 mM KCl. 72
Figure 3.3: Comparison of glutamate release capacity in subregions of the rat hippocampus following stimulation with 120 mM KCl. 73
Figure 3.4: KCl concentration-dependent alteration in subregional glutamate release capacity.. 74
Figure 3.5: Rise times to maximum signal amplitude following local application of 70 or 120 mM KCl in the DG subregion.. 75
Figure 3.6: Average rates of glutamate uptake in the hippocampal trisynaptic pathway.. 76
Figure 3.7: Depth profile of resting glutamate in the anesthetized rat hippocampus. 77
Figure 3.8: Depth profile of KCl-evoked glutamate in the anesthetized rat hippocampus. 78
Figure 3.9 Validation of glutamate signals in the CA1 subregion of the unanesthetized rat hippocampus.. 79
Figure 3.10: Resting glutamate measurements over three days in the CA1 subregion of unanesthetized rats.. 80
Figure 4.1: Comparison of slope and LODs of W4 and S2-MEAs. 92
Figure 4.2: Secondary electron micrographs of front surface of the MEA. 93
Figure 4.3: Secondary electron micrographs of the back surface and sides of the MEA.. 94
Figure 4.4: Defects from photolithographic processing...................................... 95
Figure 4.5: Backscattered electron micrographs of MEA surfaces. 96

Figure 4.6: X-ray dispersive spectroscopy of Pt sites.. 97
Figure 4.7: Atomic force microscopy of Pt sites. 98
Figure 4.8: Three dimensional projections of Pt topography data 99
Figure 4.9: Representative polyimide coated connecting line. 100
Figure 4.10: Multiple line profiles and frequency distribution of surface features on Pt sites. 101
Figure 4.11: Frequency distribution of surface features on ceramic substrate. 102
Figure 5.1: Comparison of slope and LOD characteristics of manually-coated and microplotter-coated MEAs. 113
Figure 5.2: Vertical separation between jetting orifice and Pt Sites of MEA. 114
Figure 5.3: Calibration of Jetlab® cameras and translation stages. 115
Figure 5.4: Pulse waveforms used to control droplet size. Fine tuning of droplet size and shape was achieved by altering the voltage and dwell times for the piezoelectric pulse. A unipolar square waveform was used for gluteraldehyde solution while a bipolar waveform that contained features of a square wave and a sine wave was used for BSA/Enzyme Coatings. 117
Figure 5.5: Common droplet behaviors observed during microprinting. 118
Figure 5.6: Examples of high precision enzyme coatings using Jetlab microprinting devices. 119
Figure 5.7: Comparison of slope and LOD characteristics of manually-coated and Jetlab®-coated MEAs. 120
Figure 6.1: T_1-weighted magnetic resonance imaging of the brain-MEA interface. Images are shown in serial coronal sections (500 µm thickness). 137
Figure 6.2: Cresyl violet imaging of the MEA track at days 1 and 7 138
Figure 6.3: Cresyl violet imaging of microelectrode track at weeks 8 and 16.. 139
Figure 6.4: Tissue sections colabeled for GFAP and Iba1 at days 1, 3 and 7 after chronic MEA implantation.. 140
Figure 6.5: Tissue sections colabeled for GFAP and Iba1 at weeks 8 and 16 after chronic MEA implantation. 141
Figure 6.6: Quantitative analysis of mean GFAP and Iba1 immunoreactivity around MEA tracks in the rat hippocampus. 142
Figure 6.7: Scanning electron micrographs of biological material on MEA samples.. 143
Figure 6.8: GFAP staining of tissue material on MEAs. 144
Figure 6.9: Comparison of mean GFAP and Iba1 immunoreactivity around MEA tracks in the PFC of Long Evans rats and hippocampus of F344 rats.. 145
Figure 6.10: Chronic recordings of multiple single-neuron activity in the rat hippocampus using MEAs. 146
Figure A.1: General script that can be customized for jetlab-based enzyme coatings. 151

Chapter One: Introduction

For the last thirty years, the hippocampus has been intensively studied by neuroscientists for its vital role in cognitive learning and memory formation. Though much is known about the structural and functional properties of neurons found in this region of the brain, an understanding about how multimodal sensory information to the hippocampus is encoded into a new memory or learned behavior is necessary.

The hippocampus is one of the first structures to be affected in Alzheimer's disease (Braak and Braak, 1998; Du et al., 2004; van de Pol et al., 2007) while dysfunction of this brain region has been hypothesized to underlie disturbances in sensory gating in patients with schizophrenia (Miller et al., 1992). The hippocampus is also extremely vulnerable to tissue damage from hypoxic-ischemic injury (Ben-Ari, 1992; Del Bigio and Becker 1994) and recurrent seizures (During and Spencer, 1993). Knowledge about the molecular mechanism(s) responsible for the pathologies and cognitive deficits accompanying these diseases is needed to aid the development of diagnostic tools and treatments.

1.1 Neuroanatomy and Physiology of the Hippocampus

The mammalian hippocampus is composed of several cytoarchitectonically distinct subregions that are connected by a highly organized three-layer circuit named the trisynaptic pathway (Amaral et al., 1989). Synaptic communication within this pathway is unidirectional and widely suggested to be mediated by ionotropic receptors located on the post-synaptic cell membrane, specifically α – amino – 3 – hydroxyl – 5 – methyl – isoxaole – propionic acid (AMPA), and N – methyl – D – aspartate (NMDA) receptors (Figure 1.1). The ligand activating these receptors is L-glutamate, the chief excitatory neurotransmitter in the hippocampus and brain. After binding to glutamate, these receptors generate excitatory post-synaptic currents (EPSCs) that are propagated down the length of the neuron via transient changes in the resting potential of the cell membrane (Andersen et al., 1966).

Viewed in cross-section, the rodent hippocampus appears as a pair of interlocking U or V shaped structures (Pritchard and Alloway, 2002). The structure with its crest oriented towards the midline is the dentate gyrus (DG) while the other structure is called the hippocampal cortex or cornu ammonis (CA) field. The arms of the DG are called suprapyramidal and infrapyramidal blades based upon their proximity to the cortical surface of the brain. The hippocampal cortex also consists of supra and infrapyramidal blades; the former is commonly known as the CA1 field while the latter is the CA3. Each structure is composed of three cell layers. Starting at the pial surface and going outwards, these are the molecular, granule and polymorphic cell layers for the DG and stratum radiatum, stratum pyramidale (lucidum for the CA3) and stratum oriens for the CA fields.

The trisynaptic pathway is formed by neurons with cell bodies located in the principal cell layer of each subregion, i.e., granule and pyramidal cell layers because these are the only neurons giving rise to axons that innervate the adjoining hippocampal field. Figure 1.2 is a simplified illustration of the trisynaptic pathway and shows the relative anatomical location of these principal neurons. Axon terminals from layer II (and minor projections from layers V and VI) of the entorhinal cortex (EC) connect with dendrites of granule cells in the molecular layer of the DG, forming the first synapse of the trisynaptic circuit (Steward and Scoville, 1976). These afferent fibers also represent the major input to the hippocampus, known as the perforant pathway. Axons of granule cells, known as mossy fibers, form the second synapse by connecting to dendrites and soma of pyramidal cells in the CA3 through the mossy fiber pathway. Dendrites in the CA1 region receive their primary excitatory input from Schaffer collaterals, which are axons of CA3 pyramid cells. This connection forms the third synapse. Finally, the CA1 provides the extrinsic projection out of the hippocampus to the subiculum, ultimately closing the trisynaptic loop through direct and indirect synaptic connections with layer III of the EC.

Outside of the serial connections of the trisynaptic pathway, the principal neurons in each hippocampal field also receive ‘parallel’ excitatory (glutamatergic) inputs from intrinsic and extrinsic sources (Figure 1.3). For example, granule cells form reciprocal contacts with mossy cells located in the polymorphic layer of the ipsilateral and contralateral DG. These connections are believed to serve as a significant source of excitation for granule cells. Similarly, CA3 pyramidal neurons are heavily innervated by their own collaterals (associational inputs) while also forming reciprocal connections with pyramidal cells in the contralateral CA3 (commissural connections) (Ishizuka et al., 1990; Li et al., 1994). They also receive projections from layer II of the EC. In contrast to the DG and CA3, very few associational connections have been observed in the CA1 though it receives excitatory inputs from a separate set of EC terminals (layer III) (Witter, 1993).

Pyramidal cell response in the hippocampus is also modulated by other neurotransmitters and neuropeptides. Each subregion is populated by a wide variety of interneurons that provide monosynaptic and disynaptic inhibitory control of excitatory outputs. A study by Walker et al (2002) showed that at least some mossy fibers terminating in the CA3 are immunoreactive for GABA and dynorphin. Other than local interneurons, the DG receives cholinergic and GABA-ergic inputs from septal nuclei in the basal forebrain (Andersen et al., 2007). Similar projections to CA fields are both bilateral (to both brain hemispheres) and reciprocal. Of these, the cholinergic projections are powerful modulators of neuronal excitation. Both muscarinic and nicotinic choline receptor subtypes are known to influence glutamate release from pyramidal neurons (Chessell and Humphrey, 1995; Dijk et al., 1995). Finally, the hippocampus receives discrete noradrenergic, serotonergic and dopaminergic inputs from the basal forebrain and regions of the brainstem. While the functional implications of this complex circuitry are not completely understood, it appears that hippocampal subregions are not entirely dependent on the trisynaptic circuit for their function.

Almost all the neuronal projections mentioned up to this point follow a convergent-divergent type of connectivity that is unique to the hippocampus. For example, the axon of a single granule cell forms contacts with many CA3 pyramidal cells (divergence). Though each pyramidal cell only forms a few contacts with this axon, it receives similar projections from many granule cells (convergence). The nature of this connectivity has led researchers to hypothesize that each substructure functions semi-independently, while also operating in concert with other hippocampal fields (Kesner and Hopkins, 2006). Support for this theory comes from electrophysiological recordings where pharmacological inactivation of granule cells appears to have no effect on CA1 neuronal activity (Andersen et al., 2007). More recently, a study by Greene et al (2009) provided evidence for dissimilar gene expression profiles between principal neuron layers, shown by experiments of laser-capture microdissection and microarray hybridization. Their study showed that pyramidal neurons could be differentiated both from granule cells and from each other. Based on the number and type of mRNA transcripts expressed in each region, the authors proposed that functional differences between regions are more likely to be due to wide-ranging expression differences of modest magnitude than extreme differences in a few genes. Greene and colleagues also described specific differences in transcripts related to energy metabolism or cell survival that may have significant implications for the functional and physiological properties of each region. Collectively, these studies emphasize the importance of conducting discrete investigations in each subregion.

The cellular architecture and connections described in the preceding paragraphs correspond to the rat hippocampus, but can be used to model brain function in higher mammals for experimental purposes because of highly conserved phylogeny between species (Squire et al., 1992). Differences of note are the relatively thicker CA1 in humans and a greater number of EC subdivisions in humans. Rats also have substantial commissural projections that constitute nearly one sixth of the excitatory input to the rodent dentate gyrus (Raisman 1965, Gottlieb and Cowan, 1973). Hippocampal commissural connections are almost entirely absent in primates (Amaral et al. 1984). These are important considerations when extrapolating the results of animal studies to the clinical setting.

1.2 Glutamate Regulation and Hippocampal Function

As described earlier, glutamate is the predominant neurotransmitter for receptor-mediated excitatory transmission in the hippocampus. Glutamate synthesized in presynaptic nerve terminals is transported into vesicles by vesicular glutamate transporters (VGLUTs) and exocytosed into the extracellular environment following calcium-dependent release of glutamate from synaptic vesicles (Bellocchio et al., 2000). Astrocytes also release glutamate (Angulo et al., 2004; Volterra and Steinhauser, 2004), and are suggested to be an important modulator of hippocampal glutamate transmission, though their precise role is not completely understood (Araque et al., 1999). Glutamate receptors, both ionotropic and metabotropic subtypes, are widely distributed on neuronal and glial cell membranes, therefore high level control over neurotransmitter concentration is necessary to maintain targeted activation of post-synaptic glutamate receptors (Meldrum, 2001). Immediately following release, glutamate is rapidly removed from the synapse by a family of high-affinity, sodium-dependent transporter systems. Of the known subtypes, the most abundant glutamate transporter in the rodent hippocampus is GLT-1, followed by EAAC1 and GLAST (Rothstein et al., 1994; Danbolt, 2001). GLT-1 and GLAST are exclusively expressed in astrocytes while EAAC1 is found on pyramidal cell bodies and their post-synaptic dendrites. The corresponding human transporters are referred to as EAAT2, EAAT1 and EAAT3, respectively. In both species, over 90% of extracellular glutamate is actively transported out of the extracellular matrix by GLT-1 and GLAST, providing further evidence for the importance of glial cells in maintaining normal glutamate transmission in the hippocampus and other brain regions (Haugeto et al., 1996; Danbolt, 2001).

Glutamate is believed to contribute to hippocampal-dependent learning and memory through long-term potentiation (LTP), a form of increased synaptic strength that occurs following brief, high frequency electrical stimulation (100 Hz) of glutamatergic fibers (Kullmann et al., 1996). Indirect evidence for glutamate involvement comes from combined pharmacological and behavioral studies in rodents where NMDA receptor antagonists impaired behavioral learning while agonists for NMDA and AMPA receptors produced the opposite effect (Francis et al., 1993). Human studies of LTP are lacking for obvious reasons; however, lesioning of portions of the human hippocampus as a result of disease or injury resulted in cognitive deficits and variable levels of amnesia, similar to experimental findings (Andersen et al., 2007). It is important to mention here that much of our knowledge about LTP comes from electrophysiological studies of *ex vivo* hippocampal tissue (particularly in CA1) whereas our understanding of hippocampal-dependent learning processes is based on neuropsychological testing. Therefore, a major goal for *in vivo* electrophysiolgical studies has been to determine if the experimental paradigm of LTP truly represents memory encoding (Baudry and Lynch, 2001; Bliss and Collingridge, 1993). Until now, the overwhelming majority of evidence shows indirect associations. One explanation for this could be a lack of direct information about alterations in glutamate regulation during LTP processes.

Interestingly, LTP in the CA3 does not require synchronized pre- and postsynaptic activity at mossy fiber-CA3 pyramidal cell synapses (Synapse 2) (Daoudal et al., 2002) and receptor antagonists against AMPA and NMDA do not block this form of LTP (Bortolotto et al., 2005; Kwon and Castillo, 2008). The consensus is that mossy fiber LTP is mediated by a different set of glutamate receptors, specifically kainate-sensitive glutamate receptors (KARs) and metabotropic glutamate receptors (mGluRs) (Kwon and Castillo, 2008).

Glutamate involvement has also been suggested in the induction of long-term depression (LTD), a process where decreased synaptic strength is observed following prolonged low-frequency electrical stimulation (Mockett et al., 2002; Sajikumar and Frey, 2003; Sajikumar and Frey, 2004). Unlike LTP, LTD is not NMDA-dependent but is believed to be an important homeostatic mechanism that determines the stability of the hippocampal neuronal network. However, LTD is sensitive to AMPA or metabotropic glutamate (mGlu) receptor antagonists (Kemp and Bashir, 1999).

Apart from the different kinds of long-term plasticity changes, hippocampal synapses demonstrate numerous forms of short-term ‘memory’ that last for much shorter periods (minutes to hours) but may play an equally important role in real-time information relay between terminals (Thomson, 2000; Zucker and Regehr, 2002). Common substrates for investigations on this type of memory are the synapses formed by Schaffer collaterals and CA1 pyramidal neurons and those between principal neuron projections onto hippocampal interneurons. These synapses can show either depression or facilitation with repeated stimulation, depending on the identity of the postsynaptic terminal. Glutamate involvement in these transient processes is implied but the precise mechanism remains unknown.

Modulation of glutamatergic effects during active learning can be from multiple sources. One form of intrinsic control is by feedback inhibition or disinhibition by presynaptic glutamate receptors (iGluR and mGluR subtypes with variable distribution in different subregions) following synaptic glutamate release. Mossy fibers demonstrate an additional level of pre-synaptic control because they co-release GABA and dynorphin along with glutamate which can activate GABA autoreceptors (Andersen et al., 2007). Glia also contribute to intrinsic control by adjusting transporter efficacy. Other forms of feedback/feed-forward inputs arise from associational/commissural contacts (DG granule cells and CA3 pyramidal cells) or reciprocal connections (DG-mossy cells). Finally, cholinergic and GABA-ergic effects of extrinsic neuronal sources on hippocampal plasticity must be considered. Together, these studies support the view that regulation of glutamate is different in subregions of the hippocampus and thereofore, should be investigated separately.

1.3 Glutamate Neurotransmission in the Aging Hippocampus

Aging is not a medical condition; however aging is associated with structural and functional changes that can increase an individual's risk factor for certain diseases. The aging hippocampus, in particular, is an early target of physiological changes that have been correlated with mild cognitive impairment and diminished capacity for memory recall (de Toledo-Morrell et al., 1995). The aged hippocampus also demonstrates increased susceptibility to neurodegenerative diseases believed to have an excitotoxic component, such as temporal lobe seizures (Michaelis et al, 2001) and Alzheimer's disease (Greenamyre and Green, 1989). Because elderly individuals are the fastest growing sub-population in the United States, age-related alterations in hippocampal glutamate neurotransmission need to be identified and studied systematically.

Repeated experiments using high intensity stimulation protocols have demonstrated that LTP induction remains intact during aging in CA1 and DG tissues (Landfield and Lynch, 1977; Diana et al., 1994). However, time for LTP decay (Barnes and McNaughton, 1980) and LTD induction (Norris et al., 1996) was decreased in aged rats. These changes were correlated with behavioral testing suggesting that aged rats not only took longer than their young counterparts to encode new memories, but they also retained fewer new memories. Since LTP and LTD are NMDA-dependent processes, alterations in post-synaptic glutamate regulation can be expected in these regions.

As reviewed by Barnes and Rozensweig (2003), a majority of the basic cellular characteristics of DG granule cells, and CA pyramidal cells do not change with age, including resting membrane potential (Potier et al., 1992, 1993) and total neuron counts, though reduced hippocampal volume was observed in previous studies. These results suggest that age-related cognitive deficits are produced by other factors such as dendritic shrinkage, reduced synapse numbers, altered release kinetics or changes in the function of receptors and transporters. Again, these changes are not widespread but only affect some aged animals, indicating a mechanism for biological compensation. Indeed, a reduction in perforant path-granule cell synapse numbers and NMDA-mediated LTP was accompanied by increases in the strength of remaining synapses through AMPA receptors (Rao et al., 1994; Barnes et al., 1992). In contrast, the Schaffer collateral-CA1 circuit showed a decrease in synaptic contacts without compensation from NMDA or AMPA receptors. Rather, a decrease in postsynaptic response was correlated with impaired behavioral performance in aged rats. Age-related declines in the number of AMPA receptor binding sites, but not NMDA receptor binding sites were noted in the DG. Alterations in number of AMPA receptors with age have not been observed in the CA fields though a decrease in synaptic contacts was also noted in the CA3 (De Groot and Bierman, 1987).

Two important changes occur in astrocytes with aging. First astrocyte hypertrophy (or reactive gliosis) is observed in some studies, indicated by elevated levels of astrocyte-localized glial fibrillary acidic protein (GFAP) throughout the aging brain including the hippocampus (Linnemann et al., 1994). Typically considered an injury response, the presence of gliosis may be a sign of increased oxidative stress or inflammation in the aged hippocampus (Segovia, 2001). Astrocyte numbers are also diminished during aging along with a decrease in transporter number (Segovia et al., 2001) though the glutamate uptake and/or release capacity of reactive astrocytes is not well understood. Compensatory increases in transporter affinity or presynaptic release are possible (Saransaari and Oja, 1995) but until now a technique to investigate glutamate kinetics has been largely lacking. Prior scientific research has employed microdialysis to study changes in total hippocampal concentration of extracellular glutamate in the aging hippocampus. Even here, only two reports are available (Massieu and Tapia, 1997; Zhang et al., 2001), and their results are contradictory. The former reported an increase in tonic glutamate concentration with aging while the latter reported no change. Clearly, an improved methodology for studies of glutamate in discrete hippocampal subregions during aging is needed to correlate focal changes in excitatory transmission with hippocampal function.

1.4 Glutamate Dysregulation in Hippocampal Disease

1.4.1 Alzheimer's disease

The early involvement of hippocampal subregions in the pathophysiology of Alzheimer's disease (AD) is well-established. Specifically, a selective decline in numbers of pyramidal neurons and associated synapses is observed at all stages of the disease (Braak and Braak et al., 1998). Tissue samples examined in their study conained amyloid plaques and neurofibrillary tangles, which are now believed to be the hallmarks of AD pathology (Maragakis and Rothstein, 2001). Further evidence for loss of hippocampal function in AD is provided by memory deficits and impaired performance during cognitive tests (Vandenberghe and Tournoy, 2004), both of which are key diagnostic indicators in elderly patients.

Disruption of hippocampal glutamate transmission occurs early in the disease process. Axons from layer II and III of the entorhinal cortex (EC) carrying the excitatory inputs to the hippocampus via the perforant pathway are the first to develop AD pathology and undergo neurodegeneration. This causes the hippocampus to become disconnected from the EC, leading to a major reduction in glutamatergic input to all principal neurons in hippocampal subregions. Interestingly, neurodegeneration does not affect all regions equally. The CA1 region is primarily affected, followed by the CA3 and DG in advanced phases of AD. This is supported by histopathological observations of post-mortem brain tissue of early AD cases (Morrison and Hof, 1997). Neurons with positive immunoreactivity for glutamate are reduced in number and co-stain for neurofibrillary tangles in the CA1 field (Kowall and Beal, 1991). Again, glutamate synthesis by glutaminase appears to be unaffected in AD (Procter et al., 1988) but total numbers of glutaminase-containing neurons showed tangle formation and reduced numbers. These data suggest a role for pre-synaptic dysregulation of glutamate.

Studies using antibodies directed against the individual glutamate transporters reveal conflicting data. Reduced levels of GLT protein (but not mRNA) with normal levels of both GLAST and EAAC were reported by Li et al (1997) but not confirmed by Beckstrom et al (1999) though this may be due to differences in the handling of post-mortem tissue methodologies. A separate study by Duerson et al (2008) revealed changes in the detergent-solubility of neuronal glutamate transporter EAAC1. Selective loss of NMDA receptor is greater in AD than in aging (Greenamyre and Maragos, 1993). EAAC1 is not a major contributor for uptake of extracellular glutamate. However, it is implicated in the regulation of GABA transmission, which can have an indirect effect on glutamate through feedback inhibition. KARs are relatively spared in AD neurodegeneration but tissue levels of AMPA receptors are reduced (relative to disease-free aging) in several regions of the brain including the hippocampus (Yasuda et al., 1995; Armstrong and Ikonomovic, 1996). An emerging theory suggests that glutamate dysregulation precedes the pathology of AD because alterations in glutamate receptor content occur prior to the formation of neurofibrillary tangles (Armstrong et al., 2003).

The severe decrease in NMDA receptors in AD pathology has led to an interesting hypothesis on the mechanism of glutamate excitoxicity in the pathogenesis of AD (Greenamyre and Young, 1989). Excitotoxic damage from overexposure to glutamate generally occurs when the uncontrolled release of glutamate surpasses the capacity of astrocyte uptake mechanisms. The resulting overactivation of NMDA receptors triggers a cascade of signaling events that can cause downregulation of NMDA expression on the cell membrane, or in severe cases, cell death (Danbolt, 2001). Greenamyre and Young 1989) proposed that failure to remove non-pathological glutamate by the transporter system can also lead to glutamate accumulation and the aforementioned excitotoxicity pathway. Uptake failure can occur if the energy-dependent transporters do not receive sufficient adenosine tri-phosphate (ATP) or if the transporter protein is damaged by oxidative processes. Evidence for impaired energy metabolism, increased glucocorticoid accumulation (an oxidative stress indicator) and protein damage have been seen in several studies (Francis et al., 1993; Beal, 1998; Smith et al., 1996; Keller et al., 1992). Experimentally as well, application of excessive glutamate in neuronal culture induces simplification of the pyramidal cell's dendritic tree (Mattson, 1988; Mattson *et al.,* 1988), a feature of AD pathology (Mann *et al.,* 1986; Mehraein *et al.,* 1975). Biochemical data has shown decreased extracellular glutamate levels in AD (Hyman et al., 1987; Lowe et al., 1990). Accordingly, a more agreed-upon theory is glutamate hypoactivity in the AD-affected hippocampus caused by the selective death of pyramidal neurons (Keller et al., 1997), resulting in loss of normal trisynaptic pathway connections. Pyramidal neurons are also the site of hyperphosphorylation for protein Tau (responsible for tangle formation) and for the metabolism of amyloid precursor protein to Aβ (Francis et al., 2003). The main point of this discussion is the lack of availability of a technique that directly measures the time course of changes in glutamate transmission in Alzheimer's disease along with a lack of proper animal models for *in vivo* studies.

1.4.2 Schizophrenia

The pathophysiology of schizophrenia involves the prefrontal cortex (PFC) and mesial temporal lobe structures, including the hippocampus (for review, see Freedman and Goldowitz, 2009). Decreased hippocampal volume due to a reduction in neuronal size, not number has been reported in early stages of the disease (Nelson et al., 1998, Arnold et al., 2005). Abnormalities such as atypical orientation of CA pyramidal cells and absence of gliosis have led researchers to hypothesize that schizophrenia is a developmental disorder.

Theories about glutamate involvement in schizophrenia are not new. *In situ* hybridization of human hippocampal tissue obtained post-mortem showed that metabotropic receptor mGluR5 and glial transporter EAAT2 were similar for patients with schizophrenia and control tissue samples (Ohnuma et al., 2000). In contrast, diminished expression of VGLUT1 mRNA was noted in presynaptic terminals of hippocampal cells along with decreased activity of post-synaptic NMDA receptors (Eastwood and Harrison, 2004). A loss in AMPA receptors has also been observed, usually in the left hippocampus (Kerwin et al., 1988). To our knowledge, the functional implications of these changes have not been directly investigated. One study used magnetic resonance spectroscopy and found that total glutamate concentration was significantly higher in both prefrontal cortex and hippocampus of schizophrenic patients compared to other brain regions but behavioral correlates were only observed for the PFC (van Elst, 2005). Finally, a striking example of hippocampal involvement is observed in temporal lobe epilepsy where some patients demonstrate a psychosis that is indistinguishable from schizophrenia (Andersen et al., 2007)

Glutamate is also involved in many aspects of neuronal synaptic strength and function during development and throughout life. Synapse formation in early brain development, synapse maintenance, and synaptic plasticity are all influenced by the glutamate system. If schizophrenia is indeed determined to be the result of impaired neural development, dysregulation of glutamate can be conceived to play a major role.

1.5 Rapid Glutamate Measurements using Microelectrode Arrays coupled with *In Vivo* Amperometry

As discussed earlier, much of our present understanding about the neurotransmitter role of glutamate has come either from *ex vivo* electrophysiological investigations conducted in hippocampal tissue slices, isolated nerve terminals and cell cultures (Nicholls et al., 1993; Hjelmstad et al., 1997; Takeda et al., 2007) or from *in vivo* recordings using microdialysis probes (Bagley and Moghaddam, 1997). Data obtained from electrophysiology studies is often inconsistent, partly due to variations in the experimental methodology followed by different research groups, but more likely due to the inherent limitations of studying a brain region without its complete set of intrinsic and extrinsic connections. In addition, electrophysiology does not allow for direct measurement of glutamate concentration. The microdialysis technique has addressed some of these limitations; however, microdialysis investigations of the rodent hippocampus are limited to whole tissue studies because of restrictions in the spatial resolution (microdialysis probes are 1-4 mm in length while the rat hippocampus is only 5-6 mm wide in cross-section). Also, dynamic properties of glutamate neurotransmission cannot be investigated through microdialysis recordings because the slow sampling rates of this technique (seconds to minutes) cannot capture rapid glutamate release and uptake (milliseconds to seconds; Kinney et al., 1997) events. A detailed understanding about glutamate neurotransmission kinetics is needed because subtle changes in synaptic connectivity may be masked by biological compensation, possibly leading to unchanged levels of tonic glutamate.

The above mentioned limitations have warranted the development of new methods that can offer sensitive, reliable measurements of glutamate and other neurochemicals in the central nervous system (CNS). *In vivo* amperometry is one such recording technique that utilizes microelectrodes which can be targeted to different brain structures. The recording surface(s) or working sites of the MEA is usually composed of Platinum (Pt) or other inert metals. When a constant and sufficient potential is applied to the working sites against a reference electrode, the MEA is capable of oxidizing or reducing electroactive molecules. The current generated by the resulting Faradaic reaction can be monitored continuously and rapidly (≤1 ms) (for review, see Gerhardt and Burmeister, 2000). The current is also linear with respect to concentration of the electroactive molecule(s) in the tissue adjacent to the working sites, allowing for *in vitro* calibration for *in vivo* investigation. Finally, because the working electrode is continuously maintained at a fixed potential, the non-Faradaic background current detected by the MEA is extremely low, allowing for highly sensitive measurements (pA - nA).

Using these principles, we have developed ceramic-based microelectrode arrays (MEAs) that are capable of measuring rapid tonic and phasic neurotransmitter changes in the central nervous system (CNS) (Burmeister et al., 2001; Pomerleau et al., 2003). Our MEAs are composed of a 2 x 2 array of micron-sized Platinum (Pt) recording sites arranged in dorsal-ventral pairs on a smooth ceramic substrate (Coors Ceramic Co., Golden, CO) (Figure 1.4 A). A low noise, computer controlled, multi-input potentiostat (Fast16mkII recording instrumentation, Quanteon LLC, Nicholasville, KY) completes the external circuit and allows simultaneously recordings from all the Pt sites. To extend the recording capability of the MEAs to non-electroactive neurotransmitters such as glutamate and choline, our laboratory has pioneered the use of oxidase enzyme coatings (Burmeister et al., 2001, 2006, 2007). These enzymes oxidize the molecules of interest and convert them to hydrogen peroxide ‘reporter’ molecules. When a constant potential of +0.7 V is applied to the MEA vs. an Ag/AgCl reference, H_2O_2 donates two electrons to the Pt sites. The two step reaction for glutamate catalysis is given below:

$$\textit{L-glutamate} + H_2O + \textit{GluOx/FAD} \longrightarrow \alpha\textit{-ketoglutarate} + NH_3 + \textit{GluOx/FADH}_2$$

$$\textit{GluOx/FADH}_2 + O_2 \longrightarrow \textit{GluOx/FAD} + H_2O_2$$

Our standard MEA design (S2 MEA) (Figure 1.4 A) has a temporal resolution of 2 Hz, allowing subsecond detection of glutamate neurotransmission. Since *in vivo* glutamate release appears as a characteristic fast current spike lasting a few seconds, a change in glutamate signaling can be correlated to specific alterations in glutamate release or uptake. We have used this capability to study glutamate in discrete brain structures like the striatum and PFC of rats (Nickell et al., 2005; Day et al., 2006), the striatum and nucleus accumbens of mice (Thomas et al., 2008) and in the motor cortex of anesthetized rhesus monkeys (Quintero et al., 2008), under urethane anesthesia. For the studies presented in this dissertation, we developed a novel MEA design (W4 MEA), comprised of smaller Pt sites (20 X 150 μm) (Figure 1.4 B). The total recording area of the W4 MEA is approximately 40% smaller than the S2 MEA, making it more appropriate for discretely targeting the DG, CA3 and CA1 subregions of the rat hippocampus.

1.6 Thesis Outline

Since information relay in the hippocampal trisynaptic pathway takes places through synaptic connections using glutamate as their chief excitatory neurotransmitter, we believe that differential regulation of glutamate neurotransmission within the DG, CA3 and CA1 subregions contributes to differences in subregional hippocampal function. To investigate this hypothesis, the studies described in this dissertation used a novel MEA design (W4-MEA) in combination with amperometric measurements to gain novel insight into hippocampal regulation of glutamate neurotransmission. In addition, the present studies provided compelling evidence to support the superior biocompatibility of W4- MEAs for long term neurochemical and electrophysiological measurements. Chapter Two provides a detailed description of study designs, animal subjects, materials, instrumentation, methodology, data selection criteria and statistical analyses used in all experiments.

Chapter Three investigates the release and clearance characteristics of glutamate neurotransmission from excitatory nerve terminals in discrete DG, CA3 and CA1 subregions of the anesthetized rat hippocampus. *In vivo* measurements showed that subregional levels of resting glutamate were not significantly different in anesthetized F344 rats. However, the trisynaptic pathway does exhibit subregional differences in evoked glutamate release following local application of 70 or 120 mM KCl. Of the three subregions, capacity for glutamate release was highest in terminals localized to the CA1 field and least from the CA3 subregion.

These data suggest that less glutamate was found in the extracellular space around the MEA in the CA3 region. The most fascinating findings in this study were from KCl studies in the DG subregion. KCl-evoked glutamate release capacity in DG terminals was significantly diminished following high K^+ stimulation but demonstrated faster release kinetics, providing evidence for modulation of presynaptic glutamate release from local nerve terminals. Clearance of exogenous glutamate was not significantly different in the DG, CA3 or CA1 subregions, suggesting similar capabilities for glutamate clearance in the trisynaptic circuit. Finally, depth profile investigations of hippocampal layers in the CA1 and DG demonstrated cell layer-specific differences in evoked glutamate release capacity, as seen with local application of 70 mM KCl. Collectively, these findings validate the capability of the W4 MEA to target discrete cell layers of the rat hippocampus and provide direct evidence for subregion specific regulation of glutamate neurotransmission in the anesthetized rat hippocampus.

Chapter Three also evaluated the recording capability of chronic W4-MEAs in the CA1 subregion of unanesthetized F344 rats. These studies showed that the MEA was able to measure glutamate up on days 4, 5 and 6 post-surgery. Average levels of resting glutamate were not significantly different, indicating that W4-MEAs are capable of measuring hippocampal glutamate over multiple days and can be combined with behavioral experiments for future investigations in unanesthetized rats.

In Chapter Four, we characterized the ceramic and Pt surfaces of our MEAs. *In vitro* calibration showed that S2 and W4-MEAs were comparable with respect to recording sensitivity, though limit of detection was significantly higher for W4-MEAs. Scanning electron microscopy and atomic force microscopy of Pt sites showed that the photolithographic manufacturing process produces recording sites with microwell geometry and nanometer-sized surface features. In addition, x-ray dispersion spectroscopy showed that the Pt sites likely exist in their native metallic state and are not bound to oxygen atoms. These studies are the first to describe the surface properties of an implantable ceramic-based neural device and are expected to aid our ongoing efforts to improve and extend the recording performance of our MEA technology.

The studies in Chapter Five investigated the coating methodology and salient characteristics of two computer-controlled microprinting devices, namely the Nanoject microplotter (courtesy: Thom Coates) and the Jetlab® microprinter (Microfab Technologies, Plano, TX). Precise coatings of choline oxidase were applied on discrete Pt sites using a pressure-controlled fluid release system. We empirically determined that at least 8 serial applications of enzyme solution and 4 applications of gluteraldehyde were needed to produce a stable cross-linked enzyme layer. The performance of these MEAs was not significantly different from manually coated MEAs; however, these studies required extensive human involvement and had a longer operating time. Next, we characterized the operating parameters for the Jetlab® microprinting station. Specifically, we determined a range of operating parameters (calibration factors, drop size and drying behavior) that allowed for application of choline or xanthine oxidase solutions onto Pt sites of MEAs from a piezoelectric jetting device. For the very first time, we were able to apply uniform coatings of choline and xanthine oxidase onto separate Pt sites. Initial testing of MEA performance conducted at Microfab laboratories showed that Jetlab coated MEAs are comparable to their manually coated counterparts. High precision coatings were accompanied by lesser down time and high turnover of coated MEAs. At the present time, we were not able to replicate the necessary MEA performance at the University of Kentucky. We believe that the difference in results is due to a larger droplet size. Additional experiments are ongoing, however, our initial studies support that this coating methodology offers a greater range of coating capabilities, shorter coating time and greater control over the coating solution.

Finally, Chapter Six focused on the brain tissue reaction to W4-MEAs following implantation in the rat hippocampus. We demonstrated that MEA implants were well-tolerated up to six months, with few post-operative complications. At all time points, the MEA was surrounded by a highly active cellular sheath that was immunoreactive for GFAP (astrocytes) and Iba1 (microglia). Iba1 levels were significantly elevated from 1 to 8 weeks post-surgery but became diminished at later time points. GFAP immunoreactivity was also significantly higher by 1 week and remained high 6 months after surgery. However, the cellular sheath was less than 100 µm wide at early time points and was significantly contracted by 4 months (≤ 50 µm) suggesting that only a small amount of tissue in the immediate vicinity was affected. We also studied GFAP content on the surface of MEA implants. Two explanted probes (out of 30) showed limited GFAP immunoreactivity confirming a lack of astrocytic content on the ceramic surface. In addition, scanning electron microscopy found very little tissue adhered to the ceramic surface suggesting that cell attachment to the implant was much weaker than intercellular attachment within the sheath. Collectively, these results indicated that minimal tissue damage resulted from insertion of the MEA and its prolonged presence in the hippocampus.

Copyright © Pooja Mahendra Talauliker 2010

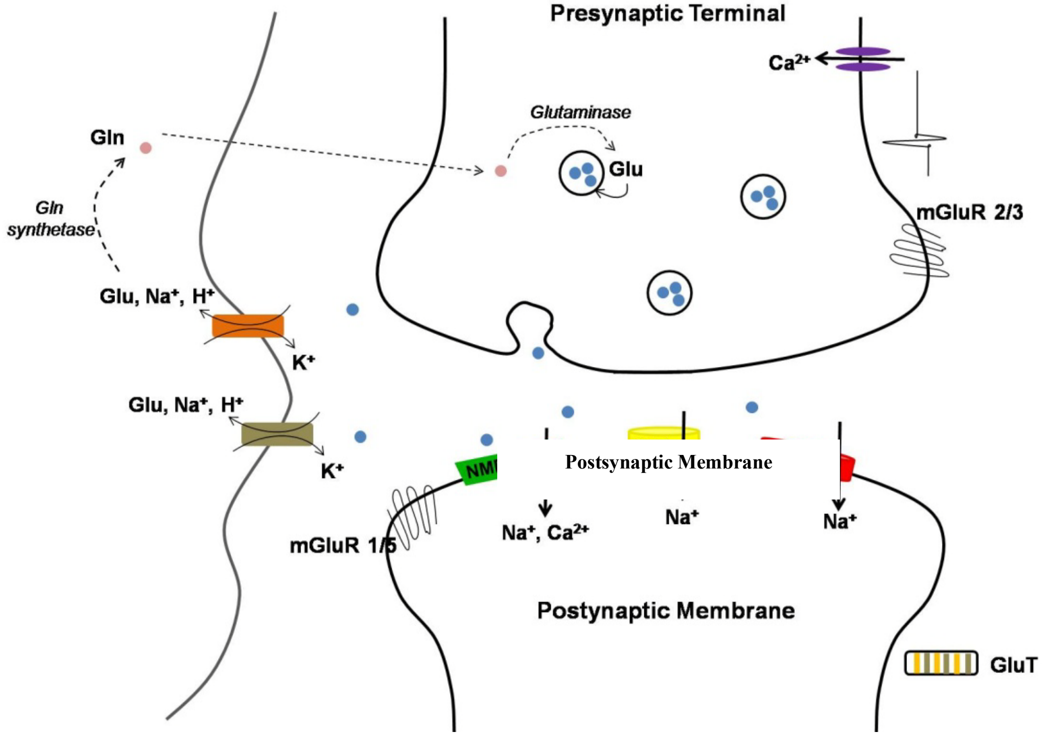
Presynaptic Terminal
Ca2+
Glutaminase
Gln
Glu
Gln synthetase
mGluR 2/3
Glu, Na+, H+
K+
Glu, Na+, H+
K+
NMI
Postsynaptic Membrane
Na+, Ca2+
Na+
Na+
mGluR 1/5
Postynaptic Membrane
GluT

Figure 1.1: Glutamate synapse. Glutamate synthesized in presynaptic nerve terminals is transported into vesicles by vesicular glutamate transporters and exocytosed into the extracellular environment following calcium-dependent depolarization of the cell membrane Glutamate receptors NMDAR, AMPAR, KAR and mGluR are widely distributed on neuronal and glial cell membranes. Immediately following release, excess glutamate is removed from the extracellular space by glutamate transporters (GluTs). Glutamate that is not recovered can diffuse to presynaptic mGluRs and auto-regulate glutamate release. Once internalized by glia, glutamate is converted to glutamine, transported to neurons and converted to glutamate for vesicle loading.

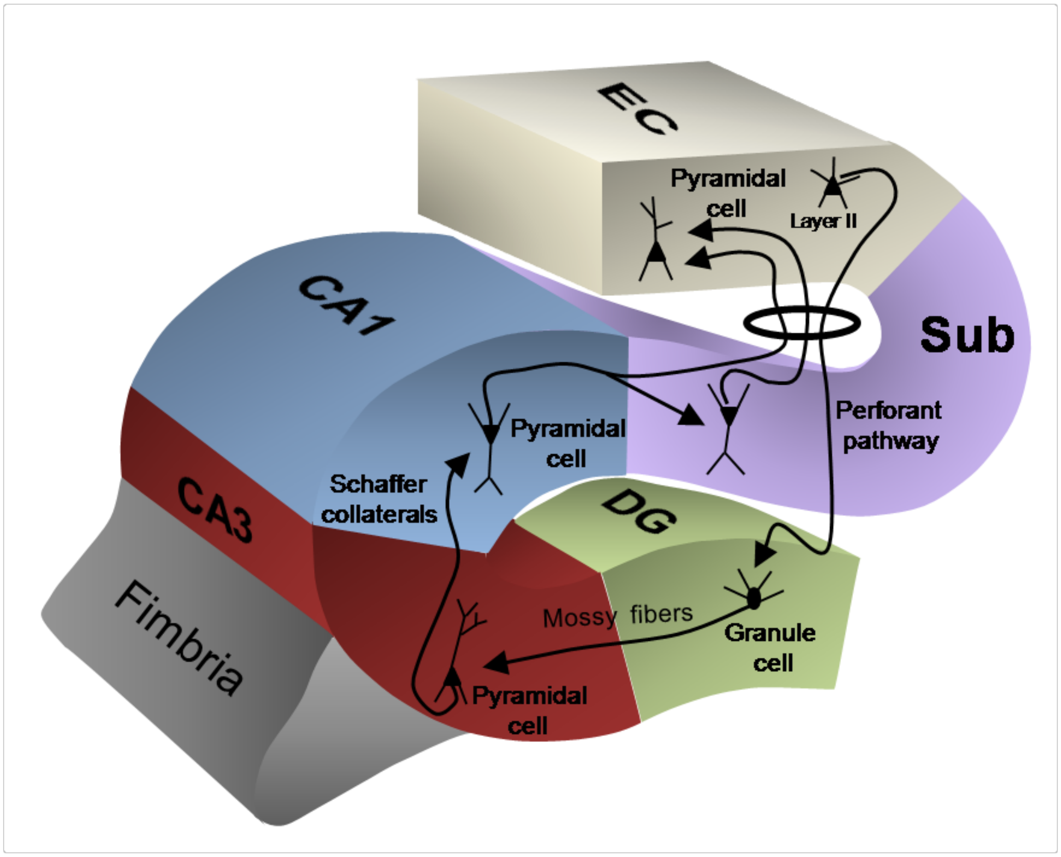
EC
Pyramidal cell
Layer II
CA1
Sub
Pyramidal cell
Perforant pathway
Schaffer collaterals
CA3
DG
Fimbria
Mossy fibers
Granule cell
Pyramidal cell

Figure 1.2: Hippocampal trisynaptic pathway. The trisynaptic pathway represents the unidirectional flow of excitatory glutamatergic neurotransmission throughout the hippocampal formation. The first synapse is at the terminal end of perforant path projections to granule cells of the dentate gyrus (DG) from the entorhinal cortex (EC), the second synapse is formed between mossy fiber projections and pyramidal cells in cornu ammonis 3 (CA3) field and the third synapse consists of CA3 Schaffer collateral projections and pyramidal cells in cornu ammonis 1 (CA1). (Figure adapted from Andersen et al., 2007)

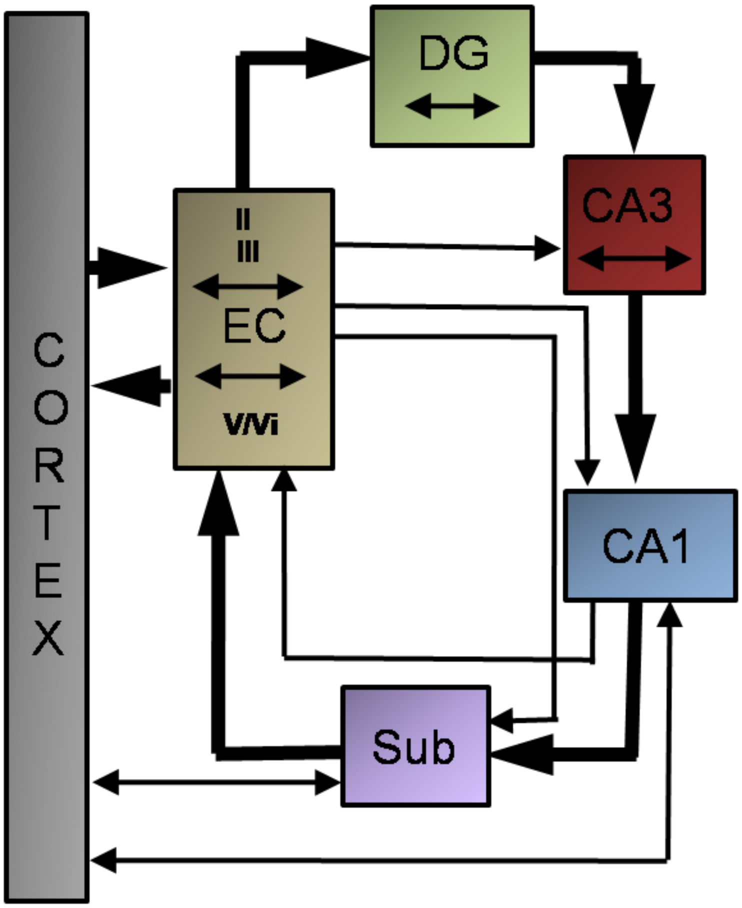

Figure 1.3: Serial and parallel excitatory connections in the hippocampus. Outside of the 'serial' connections of the trisynaptic pathway (thick black arrows), the principal neurons in each hippocampal field also receive 'parallel' excitatory inputs from intrinsic (double-headed arrows inside boxes) and extrinsic sources (thin black arrows). (Figure adapted from Andersen et al., 2007)

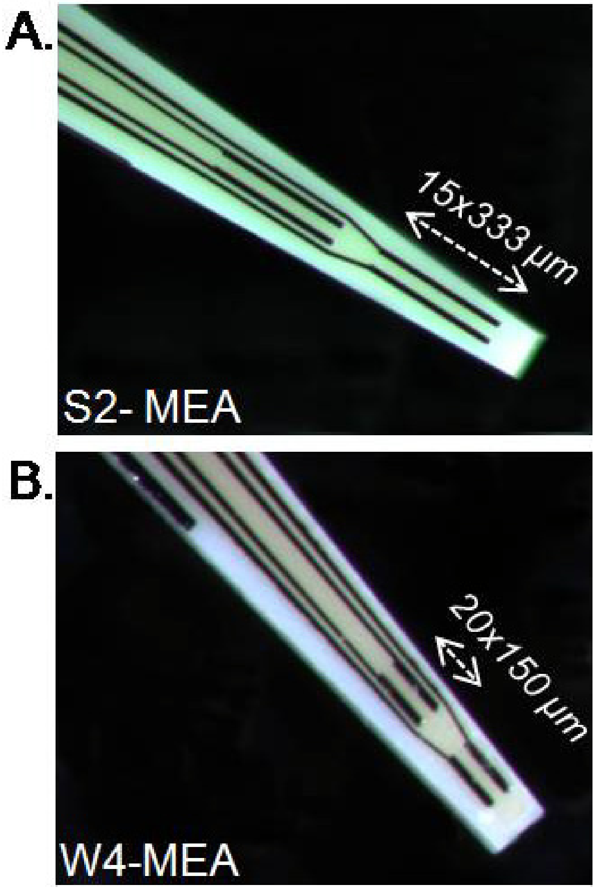
A.
15x333 µm
S2- MEA
B.
20x150 µm
W4-MEA

Figure 1.4: S2 and W4 MEA designs. Panel A shows the tip of our standard MEA design, the S2 MEA. Panel B shows the W4 MEA design which was specifically developed for *in vivo* hippocampal studies. Both designs consist of 2 pairs of Pt sites arranged in dorsal-ventral pairs though the W4-MEA has smaller site length.

Chapter Two: Materials and Methods

2.1 The Fischer 344 Rat as a Model for Studies of Human Hippocampal Function

Genetically-defined rodents have long been favored for studies of central nervous system development and function. Classical inbred rodent strains such as Fischer 344 (F344) and Brown Norway (BN) rats and C57BL/6 and BALB/C mice have been particularly useful for *in vivo* investigations in small sample sizes with low variance (Lipp et al, 2005; Witgen et al 2006). Of these, the F344 rat has traditionally been utilized in aging studies. As a result, much is known about the neuroanatomy, physiology and brain tissue morphology of this strain. The F344 rat central nervous system (CNS) has served as an excellent model for investigations of hippocampal-dependent learning (Fordyce and Farrar, 1991; Bickford et al., 1997) and dysfunction, particularly for Alzheimer's disease (Flood and Coleman, 1983; Pyapali and Turner, 1996) and temporal lobe epilepsy (Hattiangady, Rao and Shetty, 2004; Rao et al., 2007), where disease-associated neurodegeneration is known to have focal effects on the hippocampus. Based on this information as well as the relatively lower cost, ease of availability and low maintenance needs of this strain, we felt justified in choosing the F344 rat model for our investigations. It is important to note that some studies report poor behavioral performance in this strain during memory testing and spatial navigation tasks when compared to same-aged outbred rats (Lindner and Gribkoff, 1991). However, Rapp and Gallagher (1996) reason that since total neuron number is unchanged between the strains compared, this difference is likely due to reduced visual acuity, a common recessive trait in albino rats. This explanation is supported by behavioral data from their study where F344 rats showed improved performance during Morris water maze testing after extended periods of training.

The work presented in this dissertation describes novel studies of glutamate neurotransmission in substructures of the normal hippocampus, along with a detailed evaluation of the hippocampal tissue response to long term device implantation (6 months). Therefore, factors such as animal gender, age, lifespan and state of health were carefully considered. While both male and female F344 rats are used by researchers, we chose male rats to circumvent hormone-related variability in hippocampal glutamate signaling (Veng, Granholm and Rose, 2003). Also, to eliminate age-associated changes in hippocampal function (Kiang-ulrich and Horvath, 1984; Giovanni et al., 1994), we studied rats in the age group 3-5 months. F344 rats reach developmental maturity at 7 weeks (Source: National Institute of Aging); therefore the rats used in these studies are considered young adults. In addition, age-matched F344 rats demonstrate comparable body weights and brain size (Masoro et al., 1993). Finally, exposure to novel stimuli has been shown to alter hippocampal circuitry (Zhu et al., 1997; Rutishauser, Adam N. Mamelak and Erin M. Schuman, 2006). Inadvertent data bias of this kind was minimized by omitting environmental enrichment in these studies (Gagne et al., 1998; Andin et al., 2007).

2.2 Ethical Standards for the Care and Use of Animals

Male F344 rats (n = 72) were obtained at 12 weeks of age from Harlan Sprague-Dawley Inc. (Indianapolis, IN). All animal procedures were approved by the Institutional Animal Care and Use Committee at the University of Kentucky. Rats were maintained 1-2 per cage with unrestricted access to food and water per guidelines provided by the Association for Assessment and Accreditation of Laboratory Animal Care International (AAALACI). A 12-hour light / 12-hour dark cycle of illumination was maintained for all studies.

2.3 Surgery Procedures

2.3.1 Studies in Anesthetized Animals

For a detailed description of anesthesia procedures, please refer to Day et al (2006) and Hascup et al (2006). In brief, 25% w/v Urethane solution (1.25

mg/kg administered intraperitoneally) was used to induce a deep plane of anesthesia throughout the experiment. During surgery and experimentation, the rat was placed within a stereotaxic frame fitted with an adjustable arm and incisor bar (David Kopf Instruments, Tujunga, CA). Body temperature was maintained at 37°C with the aid of a re-circulating heating pad (Gaymar Industries, Orchard Park, NY) that was placed underneath the animal. The rat's eyes were coated with artificial tears (Medivet.com, #11970) to prevent dryness. Fur overlying the surgery site was shaved and the scalp was cleaned three times with alternating solutions of 70% isopropyl alcohol and povidone-iodine topical antiseptic. A 3 cm longitudinal incision was made over midline through the scalp to expose the skull. Skin and fascia were retracted with clamps. A craniotomy (4 x 6 mm) was performed over the hippocampal formation in each hemisphere. The dura was carefully pierced and dissected away to expose the cortical surface of the brain. A small burr hole was drilled over the left PFC for placement of an Ag/AgCl reference electrode. At regular intervals (20-30 minutes), saline solution (0.9%, pH = 7.4) was irrigated through the surgical site to flush away blood and debris, and to prevent drying of exposed brain matter.

2.3.2 Studies in Unanesthetized Animals

One day before surgery, animals received a subcutaneous injection of 5 mg/kg Rimadyl® (Carprofen, Pfizer Animal Health Products) to alleviate post-operative pain. Anesthesia was induced by placing the rat in a sealed chamber filled with a 2% mixture of Isoflurane (Baxter Healthcare, IL) and oxygen, after which the rat was transferred to a stereotaxic frame fitted with an anesthesia nose mask, adjustable arm and incisor bar (David Kopf Instruments, Tujunga, CA). Surgery was performed in a disinfected vertical laminar flow workstation (Microzone Corp., Ontario, Canada), using sterile surgical instruments. The rat's eyes were coated with artificial tears (Medivet.com, #11970) to prevent dryness and infection. Fur overlying the surgery site was shaved. The scalp was cleaned three times with alternating solutions of 70% isopropyl alcohol and povidone-iodine topical antiseptic. An incision (1.5 – 2.0 cm) was made along midline through the scalp to expose the skull overlying the hippocampus. The incised skin was retracted with clamps and the fascia was carefully moved aside. A craniotomy (3 mm x 3 mm) was performed over the right hippocampus. The dura was carefully dissected away to expose the cortical surface of the brain. Burr holes were drilled into the frontal cortex and left hippocampus for placement of three stainless steel bone screws (outer diameter = 0.5 mm). For glutamate recording studies, an additional burr hole was drilled for placement of a miniature Ag/AgCl reference electrode. After the skull was fitted with bone screws, the MEA assembly was slowly lowered into the brain at an approximate rate of (0.1 $mm \cdot s^{-1}$). The retraction clamps were removed and the entire surgical site was filled with a mixture of fast-setting cold cure dental cement (Lang Dental Manufacturing Co., Inc.) which adhered tightly to the skull screws. Additional dental cement was used to cover the MEA implant and close the surgery site. The entire surgical procedure lasted for approximately 1.5 hours.

Just before withdrawing anesthesia, rats received a subcutaneous injection of 3 ml saline and 5mg/kg Rimadyl®. Animals were placed on a heated pad to help maintain body temperature until fully conscious. For two days post surgery, a soft food diet was provided. Rimadyl® and saline were given as needed for management of post-operative pain and dehydration. Animals were monitored everyday for weight loss, distress, infection and problems with healing of the surgery site. For long term studies, the animal's health was routinely evaluated. Rats exhibiting prolonged discomfort or infection were euthanized immediately with an overdose of isoflurane anesthetic (5%) followed by decapitation and were excluded during data analysis. Overall, the surgical procedure was tolerated extremely well, indicated by a minimal loss of body weight (<5%) post-surgery.

2.4 Euthanasia and Tissue Recovery

At the end of an experiment, urethane-anesthetized rats underwent transcardial perfusion with 120 ml of saline followed by 60 ml of 4% paraformaldehyde. Rats used for freely moving studies were first anesthetized with isoflurane (5%), and then euthanized by transcardial perfusion. Depending on the type of study, brains were processed either for MEA placement verification (Figure 2.6) or histological analyses.

2.5 *In Vivo* Amperometry Using Ceramic-based MEAs

2.5.1 MEA Design and Fabrication

For a detailed description of design and fabrication procedures please refer to Burmeister et al (2000) and Hascup et al (2006). MEAs were manufactured on a large scale with high reproducibility using a series of photoresist layers and coating masks (Hybrid Circuits Inc., Sunnyvale, CA). Figure 2.1 illustrates the photolithographic procedure. High density fabrication was achieved by patterning multiple MEAs onto a single ceramic (Al_2O_3) wafer (Coors Ceramic Co., Golden, CO) measuring 2.5 cm x 2.5 cm X 37.5 µm. Ceramic substrates are known for rigidity, durability and inertness, making them a good choice for use as an indwelling implant. The 99% pure Titanium and Platinum layers were deposited onto the wafer to define recording sites, connecting lines, and bonding pads. With the exception of the Pt sites, all circuitry was protected from aqueous environments by spin-coating polyimide onto the surface. Recently this process has been improved by vacuum deposition of the polyimide, making it an integral component of the MEA surface. A diamond saw was used to pattern MEA tips with smooth edges (Hybrid Circuits, Inc., Sunnyvale, CA), a significant advancement over previous laser-cutting methods.

For the work presented in this dissertation, we utilized a novel MEA design (W4 MEA), comprised of four Pt surfaces (20 X 150 µm) arranged in dorsal-ventral pairs (Figure 2.2 A). The total recording area of this design is approximately 40% smaller than our standard MEA design. Detailed parametric studies have shown that the recording performance of the smaller Pt sites is comparable to our standard MEA. This geometry is ideal for targeted measurements in the DG, CA3 and CA1 subregions of the rat hippocampus. MEAs intended for use in anesthetized animals were attached to a printed circuit board (PCB) that was fitted with connections to the amperometric recording instrumentation (Figure 2.2 B). A shortened PCB was used for studies in unanesthetized animals (Figure 2.2 C). All assembled MEAs underwent intensive cleaning before *in vivo* use.

2.5.2 Amperometric Recording Instrumentation

A potentiostat (FAST16mark II system, Quanteon L.L.C, Nicholasville, KY) was used to maintain a constant voltage of +0.7 V between the Ag/AgCl reference electrode and the working sites of the MEA. Current generated at the Pt recording sites was recorded at sampling rates of 2 or 10 Hz. Current-to-voltage converters had a final gain of 2 $pA \cdot mV^{-1}$ for all experiments. The stored data was analyzed offline using custom designed Microsoft Excel spreadsheet and Matlab®-based software (courtesy Jason Burmeister, 2009).

2.6 Glutamate Measurements in Anesthetized Rats

2.6.1 MEA Preparation

W4 MEAs were prepared for *in vivo* use as described in our previously published methods (Burmeister et al., 2002; Hascup et al., 2006, Thomas et al., 2008). Since glutamate is non-electroactive, it is necessary to modify the Pt recording sites with glutamate oxidase coatings that allow for detection of glutamate. An enzyme solution of 1% glutamate oxidase, 1% bovine serum albumin and 0.125% gluteraldehyde was manually applied to the lower pair of Pt sites (marked A in Figure 2.3) for glutamate measurements. The ‘sentinel’ site pair (marked B in Figure 2.3) was similarly coated with an inactive protein of bovine serum albumin and gluteraldehyde without glutamate oxidase. This type of differential coating technique allowed for the validation of true glutamate signals though self-referenced signal comparisons with the sentinel sites. Coatings were cured for 48 hours to improve immobilization of the enzyme matrix to the Pt recording surfaces. Immediately prior to *in vitro* calibration, 1, 3-phenylenediamine (poly-mPD) was electropolymerized onto all Pt surfaces to create an interferent exclusion layer against electroactive molecules such as ascorbate, dopamine and DOPAC (Friedemann et al., 1996). The resulting poly-mPD matrix permitted diffusion of small molecules like NO and H_2O_2 (Figure 2.3).

2.6.2 *In Vitro* Calibration and MEA Selection Criteria

Calibrations were performed to determine the performance of MEAs by comparing the recording characteristics of each Pt site with standard criteria. Data obtained during calibration was used to correct slight differences between Pt sites caused either during photolithography or due to differences in the quality of manually applied coatings. During calibration, the MEA tip was submerged in 0.05 M phosphate-buffered saline (40 ml stirred solution, pH 7.4, 37°C) and maintained at a constant potential of +0.7 V vs. an Ag/AgCl reference by the FAST16*mkII* system. A standard response curve was generated by adding successive aliquots of 20 mM glutamate solution to produce final beaker concentrations of 20, 40 and 60 μM (Figure 2.4). The resulting increase in oxidation current (nA) was used to determine the coefficient of calibration that equated an observable change in electron current to a known change in glutamate concentration (Burmeister and Gerhardt, 2001). The slope ($nA \cdot \mu M^{-1}$) of the standard response curve was used to calculate the limit of detection for glutamate signals (LOD) which is the most important parameter for determining MEA usability. Note that a change in current was determined to be a signal only if the change in amplitude was at least 3 times greater than the root mean squared noise on the baseline current. MEA selectivity (ratio of glutamate molecules measured per molecule of ascorbate) was determined using a 250 μM ascorbic acid challenge. At the end of calibration, MEA sites were exposed to 2.0 μM Dopamine to confirm the interferent blocking capacity of the mPD layer (also a negative control) and 8.8 μM H_2O_2 to test the responsiveness of each working site (positive control). Sites were also tested for sensitivity to intracranial solutions to avoid false positive measurements *in vivo*. Standard selection criteria for W4 MEAs were defined as: Slope ≥ 5 pA·μM^{-1}, limit of detection ≤ 1.0 μM, Selectivity ratio ≥ 20:1 (glutamate:ascorbic acid) and response linearity to glutamate ≥ 0.997.

2.6.3 Experimental Setup for Glutamate Recordings

A pre-pulled glass micropipette (internal diameter: 0.58 mm, A-M Systems Inc., Everett, WA) was attached to the PCB holder such that the tip (internal diameter: 10 - 12 μm) of the micropipette was 70 ± 10 μm away from the MEA surface, between all four recording sites. Through this micropipette, solutions of KCl (70 or 120 mM; Day et al, 2006) or glutamate (100 μM prepared in 0.09% Saline) were delivered to study stimulus-evoked glutamate overflow and extrasynaptic glutamate clearance in the DG, CA3 and CA1 fields of the rat hippocampus. A Picospritzer II pressure ejection system was used to control solution volumes by adjusting the applied pressure (5–20 psi) for a fixed period of time (0.5 s).

Stereotactic coordinates for DG, CA1 and CA3 were calculated using the rat brain atlas of Paxinos and Watson (2005) where anterior–posterior (AP), medial-lateral (ML) and dorsal-ventral (DV) measurements were taken from *bregma*, midline and surface of the skull, respectively (refer to Table 2.1 for exact coordinates; locations shown in Figure 2.6). The subregions were targeted in random order during experiments to avoid bias. A microdrive attached to a stereotaxic arm was used to lower the MEA/micropipette assembly into the hippocampus until the center of the lower site pair was aligned with the tissue coordinates for each subregion. A miniature Ag/AgCl reference electrode was inserted in the left pre-frontal cortex to complete the electrochemical circuit. Note that the curved anatomy of the hippocampus made it possible to measure glutamate from the CA1 and DG at the same AP and ML coordinates at different depths.

2.6.4 Resting Glutamate Measurements

All glutamate measurements were taken during the light phase. A key benefit of our MEA design is the use of ‘sentinel’ recording sites for self-referencing. The sentinels are identical to the recording MEA except for the oxidase enzyme layer. As a result, data from the sentinel sites can be used to detect and remove undesirable molecules by subtracting the response of the sentinel sites from the primary recording sites. This subtraction technique is analogous to the working principle of spectrophotometry. Using this dual-channel recording strategy, the oxidation current on the sentinel sites is subtracted from the oxidation current on the working sites to determine current corresponding to glutamate. This current is divided by the MEA calibration curve (from calibration) to obtain true resting glutamate concentrations in hippocampal subregions (Figure 2.5)

2.6.5 Stimulus Evoked Glutamate Overflow

At each tissue location, baseline glutamate measurements were acquired for at least 15 minutes prior to intracranial application of solutions. Phasic release of glutamate was produced by applying nanoliter volumes (12.5 – 150.0 nL) of low concentration KCl (70 mM KCl, 2.5 mM $CaCl_2$, 79 mM NaCl) or high concentration KCl (120 mM KCl, 2.5 mM $CaCl_2$, 35 mM NaCl) into the DG, CA3 or CA1 subfields (n = 7 for each subregion, $n_{ANIMALS}$ = 21). Solution volumes were determined by measuring fluid displacement in the micropipette with a zoom capable stereomicroscope fitted with a calibrated reticule (Cass et al, 1992; Friedemann and Gerhardt, 1992). A dose response study was used to obtain reproducible glutamate signals and determine maximum glutamate release in each subregion.

2.6.6 Clearance of Locally Applied Glutamate

Clearance of physiologically relevant quantities of glutamate was studied by applying an exogenous solution of 100 μM glutamate (n = 6 for each region, $n_{ANIMALS}$ = 17). This allowed us to study clearance of glutamate at a physiologically relevant concentration, and offered the benefit of isolating glutamate clearance mechanisms. This is distinct from studying glutamate clearance following KCl-evoked release, because potassium depolarization of neurons causes a non-selective release of neurochemicals, such as GABA or other potentially modulatory molecules. Application of exogenous glutamate also allowed for control of KCl effects on glutamate transporters.

Average evoked glutamate release observed across all hippocampal regions from KCl studies was used to determine the volume (12.5 – 75.0 nL) and amplitude range of locally applied glutamate. Glutamate clearance capacity was analyzed in terms of uptake rate (expressed as the product of (Amplitude_{MAX}) and first order rate of signal decay k^{-1} (s^{-1}), or T80 (time taken for signal to decay by 80% from maximum amplitude) (Figure 2.5).

2.6.7 Depth Profile Investigations of Glutamate Neurotransmission

A hippocampal depth profile of resting glutamate was obtained by positioning the MEA tip in the stratum oriens of the CA1 and lowering it by -0.35 mm to target the stratum radiatum of the CA1 as well as the suprapyramidal molecular layer, polymorphic layer and infrapyramidal layer of the DG subregion.

Regional variations in phasic glutamate were determined by targeting the MEA to the suprapyramidal stratum oriens of CA1. Once stable baselines values were reached, phasic glutamate release in response to 70 mM KCl stimulation (a total of 5 ejections applied after two minutes) was investigated. Next, the MEA was lowered by a distance of 0.35 mm to reach the suprapyramidal stratum radiatum of CA1. As before, phasic glutamate was determined. This process was repeated three more times to obtain glutamate measurements for the suprapyramidal molecular layer, the dentate hilus and infrapyramidal molecular layer of DG.

2.6.8 MEA Placement Verification

At the end of each experiment, rats were euthanized as described in section 2.4. Paraformaldehyde fixed hippocampal tissues were sectioned using a cryostat (30 µm) and stained with cresyl violet to verify placement of the MEA tracks.

2.6.9 Data Analysis and Statistics

Resting glutamate values obtained from left and right brain hemispheres were averaged and reported as one measurement per region per rat (n = 30). Glutamate signal data obtained from local application of KCl in the DG, CA3 and CA1 hippocampal subregions was recorded by the FAST16mkII system. Signal parameters were analyzed offline with custom-created Matlab® software (courtesy Jason Burmeister, 2009). For comparison purposes, data from a given subregion was included in the analysis only if the signal could be reproduced three times. Volume-matched and amplitude-matched glutamate signals were selected from each region to determine maximum increase (µM) in stimulus-evoked glutamate concentration from baseline values ($\text{Amplitude}_{\text{MAX}}$), and the time, T_{RISE} (s), time to reach $\text{Amplitude}_{\text{MAX}}$. As mentioned above, glutamate clearance capacity was analyzed in terms of uptake rate (expressed as the product of ($\text{Amplitude}_{\text{MAX}}$) and first order rate of signal decay k_{-1} (s^{-1}), or T80 (time taken for signal to decay by 80% from $\text{Amplitude}_{\text{MAX}}$).

It is important to note that glutamate signals could not be obtained from every region for each animal due to a depression of signals following repeated KCl ejections. Accordingly, paired comparisons were not conducted. For statistical comparisons, a one-way analysis of variance (ANOVA, significance defined as $p<0.05$) along with Tukey-Kramer post-hoc tests (GraphPad Prism 5.0) were performed.

2.7 Glutamate Measurements in Unanesthetized Rats

2.7.1 Chronic MEA/Cannula Assembly

For these experiments, a modified PCB design was used for all recordings (Figure 2.2 D). Recording sites of all MEAs were coated with Nafion® and dried at 175°C for 4 minutes for improved selectivity. Nafion® has a net negative charge; therefore it repels anionic interferents such as ascorbic acid and DOPAC (Gerhardt et al., 1984). Parametric studies demonstrated greater stability for Nafion® in comparison to mPD during chronic experimentation (Hascup, unpublished data). Similar to section 2.6, MEAs were configured for selective glutamate detection. Circuit connections for the recording sites and a miniature Ag/AgCl reference electrode were soldered to a modified pedestal connector (Ginder Scientific, Ottawa, Ontario) and insulated with epoxy glue, previously described by Rutherford et al (2007). A 26-gauge stainless steel guide cannula (Plastics One, Roanoke, VA, USA) was affixed to the ceramic paddle at a distance of 60 μm with sticky wax (Kerr Corp., Orange, CA) to allow local application of exogenous solutions. During experimentation, an internal cannula was inserted into the guide. At other times, a solid stainless steel dummy cannula remained in the guide.

***2.7.2 In Vitro* Calibration and MEA Selection Criteria**

MEA performance was determined via *in vitro* calibration (described in section 2.6). MEAs were required to demonstrate sensitivity values > 2.2 pAμM^{-1}, selectivity values of at least 20:1 LOD values < 1 μM to qualify for *in vivo* use.

2.7.3 Experimental Setup for Glutamate Recordings

Following surgery, all animals were allowed to recover for three days before experimentation. On the day 4, rats were transferred to a recording chamber with a commutator coupled to a miniature current-to-voltage converter headstage (Quanteon, LLC, Nicholasville, KY) and connected to FAST16mkII instrumentation. This allowed animals to move with minimal restriction.

2.7.4 Resting Glutamate Measurements

Animals were acclimated to the recording chamber for approximately 30 minutes and then connected to the miniature current-to-voltage converter and recording instrumentation. In general, a baseline glutamate signal was obtained after 2.5 – 4 hours. Resting glutamate was measured on days 4, 5 and 6 post-surgery. In addition, MEA functionality was confirmed by local application of 2.5 μl of 1 mM glutamate through the cannula system.

2.7.5 Data Analysis

For all animals, tonic glutamate measurements obtained on days 3 and 4 were averaged and reported as a single value. A Grubb's test did not identify any significant outliers and all animals were included in the final analysis. Tonic glutamate levels in the DG, CA3, and CA1 hippocampal subregions were discretely compared across age groups using one-way analysis of variance tests (ANOVA) followed by Bonferroni's post-hoc test. Statistical significance was defined as $p < 0.05$.

2.8 Scanning Electron Microscopy Studies of MEAs

A schematic of a scanning electron microscope is shown in Figure 2.7. Electron microscopy imaging of MEAs (n = 25) was carried out at the University of Kentucky Advanced Science and Technology Commercialization Center (ASTeCC). A Hitachi S3200 variable pressure scanning electron microscope (SEM) was used to capture high resolution electron micrographs in two separate modes: secondary electron imaging (SEI) and backscattered electron detection (BSE). The former was used to capture surface features with high spatial resolution while the latter was used to detect changes in surface composition. The MEA was loaded onto a rigid specimen holder called a stub, using a graphite adhesive to assist with charging of the sample surface. Though non-conductive specimens can be observed in the SEM, we metalized the ceramic surface with a coating of Gold/Palladium alloy to maximize spatial resolution (up to 250,000X) of the signal and prevent accumulation of static electrical charge during exposure to the electron beam. The operation parameters were defined as: Accelerating voltage 20 keV, Working distance 15 mm and Beam current of 43 μA. Electron micrographs of the MEA surface were digitally captured, displayed and stored with Quartz PCI software.

2.9 Atomic Force Microscopy Studies of MEAs

We studied the surface topography of the ceramic surface, Pt recording site and polyimide coating of the W4 MEAs using atomic force microscopy (AFM). The AFM probe used in these experiments was a standard contact-mode uncoated silicon tip (Ted Pella Inc., Redding, CA) with a tip radius of approximately 10 nm and a half cone angle of 20° to 25° (measured along the cantilever axis). The MEA sample was studied at room temperature at normal atmospheric pressure. The microscope used in these studies (Digital Instruments/Veeco Nanoscope) maintained a fixed probe position but moves the sample underneath the cantilever at a fixed scan rate of 2.4 Hz in a rastered fashion to obtain a three dimensional profile of the surface of interest. The area of the sample surface was either 1 nm^2, 15 nm^2 or 20nm^2. Topography data for each sample (n = 3) was obtained three times. Following AFM experimentation, representative three dimensional images were constructed to visualize the topography of each component (ceramic, Pt and polyimide). Images constructed in perspective view illustrated the shape and general distribution of peaks and holes across the sampled region while images shown in profile view emphasize feature to feature variability in lateral spread and vertical displacement. In all images, the height scale and deflection range was adjusted to optimize the presentation of topographical information.

To quantify the AFM data, we conducted a roughness analysis for each recording site (N_{SITES} = 2, $N_{ITERATIONS}$ per site = 3) using scanning probe imaging processor, also known as SPIP software (Imagemet Metrology A/S, Denmark).

For the present study, roughness analysis values obtained for multiple sample iterations were averaged and reported as a single value for each parameter. Note that there were no significant differences between iterations for a given surface. This included calculations of average roughness (R_{AVG}, the arithmetic average of absolute values of peaks and valleys within the selected area), root mean squared roughness (R_{RMS}), surface symmetry (R_{SKEW}, dimensionless number signifying the relative proportion of peaks and valleys), maximum peak height (H_{MAX}) and maximum valley depth (D_{MAX}, absolute distance) within the sampled surface. Sudden changes in sample height, say, at the boundary of a site or the edge of the ceramic base were expected to skew roughness values therefore these portions of the image were excluded during analysis. In addition, a height distribution of the sample surface was obtained. Finally, multiple line-scans of the surface were performed as a qualitative assessment of surface roughness.

2.10 Magnetic Resonance Imaging of the Brain – MEA Interface

Please refer to the section on animal preparation for unanesthetized studies for details of the implantation procedure. Magnetic resonance imaging was performed immediately following surgical insertion of the chronic MEA to characterize hippocampal tissue response. To ensure MR-compatibility of the surgical site, the MEA assembly was cemented in place without steel bone screws. Because this requirement results in an unstable implant, the animal was euthanized immediately after the experiment. Urethane anesthesia was used to minimize movement related disruptions during imaging. T1-weight images were obtained to maximize visualization of fluid changes in the extracellular matrix surrounding the MEA. For this study we used using a Siemens Trio imager with Echo Time (T_E) set at 2.6 ms, Repetition Time (T_R) set at 25.0 ms and the Flip Angle (A_F) set to 60°.

2.11 Inkjet-based Microprinting Technology for Application of Enzymes on MEA Recording Sites

2.11.1 Principles of Piezoelectric Inkjet Printing

Piezoelectric jetting devices consist of a fine nozzle enclosed by an electromechanical element, such as a Piezo crystal. Application of a controlled intermittent voltage pulse causes mechanical deformation of the crystal element, forcing the release of fluid droplets through the nozzle (Figure 2.8). This basic principle is utilized in commercial and industrial inkjet-based devices to print pre-defined patterns onto a variety of substrates.

Figure 2.9 is a schematic representing the main components of the Jetlab® 4 microprinting station (Microfab Technologies, Plano, TX). Briefly, the printing assembly is comprised of an array of piezoelectric jetting devices (MicroJets®, Microfab Technologies, Plano, TX) and the fluidic and electrical components necessary for driving the ejection of droplets from the jetting devices. It also contains translation stages to control substrate position in the x-, y- and z- directions (Sutter Instrument Company, Novato, CA), and a visualization system for controlling the droplet placement. The jetting device is a capillary glass tube pulled to an orifice diameter of 50 µm and encased inside a piezoelectric transducer and protective metal housing. Appropriate backpressure regulation is critical for stable droplet formation. Therefore, a pneumatics controller (MicroFab Technologies, Plano, TX) and pressure/vacuum pump (Gast Manufacturing, Benton Harbor, MI) are also integrated into the printing system. Custom-coded LabView® software (National Instruments, Austin, TX) is used to control both the stage motion and inkjet printing functions. All jetting parameters, including pulse generation, number of droplets dispensed per pulse, droplet spacing and printing sequence can be controlled through the software program.

2.11.2 Preparation of Printing Assembly

At the start of an experiment, an intensive cleaning procedure was used to clean the entire dispensing system. Briefly, filtered solutions of Micro-90 detergent solution (2% v/v, Fischer-Scientific), hot water and 70% isopropyl alcohol were flushed through the jetting device and attached tubing. This is an important step that minimizes clogging of the device during printing trials. Except for the coating solutions, all fluids were through a 5 μm syringe filter (Fisher Scientific) prior to filling the reservoir to the jetting device. Droplets leaving the nozzle were viewed on a computer monitor. Illumination and tracking of picoliter sized droplets was made possible by imaging software connected to a strobed LED, a movable camera (Thales Optem, Fairport, NY), and a DVD recorder (Panasonic, Secaucus, NJ). Once a steady vertical stream of water droplets could be visualized in continuous jetting mode, the device was ready for use.

2.11.3 *In Vitro* Testing of Coated MEAs

For our optimization studies, we used choline oxidase and xanthine oxidase as test enzymes because they are relatively inexpensive in comparison to glutamate oxidase but are similar to it with respect to *in vitro* and *in vivo* behavior. Coating quality was tested by *in vitro* calibration. This has been described in detail in section 2.6. Since electrode sensitivity and limit of detection were the only parameters of interest, an exclusion layer was not applied on these MEAs.

2.12 Immunohistochemical Analysis of Brain Tissue and MEAs following Chronic Implantation

Please refer to section 2.3 for details on surgical procedures for unanesthetized animal studies. The purpose of these studies was to evaluate the biocompatibility of our current MEA design and materials for long term implantation in the rat hippocampus. Therefore rats were implanted with W4-

MEAs modified for chronic studies (Figure 2.2 C). Since glutamate recordings would not be taken for these experiments, we used non-functional MEAs lacking enzyme coatings.

Rats with chronic MEA implants in the CA3 subregion of the hippocampus (n = 5 per group) were euthanized at 1 or 3 days and 1, 8, 16, or 24 weeks via transcardial perfusion with 4% paraformaldehyde. Three animals were excluded from the study at the time of euthanasia due to infection at the surgery site. Two additional animals were removed following tissue analysis. One showed severe hemorrhaging while in the other the probe was not positioned in the hippocampus but had followed along the corpus callosum. Three animals were euthanized in the middle of the study because of a dislodged head-cap. Further, we excluded control values from animals that had a cavity in the cortex attributable to the bone screws where inflammation had followed. More detailed description of these tissues is not included as these results appeared to be due to handling of the probes and the procedures used during insertion and wound closure. Since refinement of surgical methods and experience reduces these complications, the effect of these factors on long term MEA presence is not discussed. The present study, therefore, is limited to tissues from animals in which the surgical and insertion procedures did not appear to produce any gross complications. Thus, there were 5 animals at 8 weeks and 6 months, 4 animals at 1 day and 4 months, and 2 animals at days 3 and 7.

During tissue processing, implantation times were blind-coded so as to not bias the study in any way. Brains and MEAs were removed, stored in 4% paraformaldehyde for three days, and then transferred to buffer solution containing 0.1 M phosphate with 10% sucrose and 0.01 M bacitracin until ready for processing. MEAs underwent immunohistochemical analysis to account for tissue detachment during removal. Tissue sections (14 µm thickness) adjacent to the implant track were obtained using a cryostat (courtesy Dr. Ingrid Strömberg, Umeå University, Sweden). MEAs and tissue sections were fixed in acetone for 3 minutes, followed by two incubation periods, each with a different primary antibody, for 48 hours at 4°C. For this study, we chose antibodies selective for astrocytic glial fibrillary acidic protein (anti-mouse GFAP, diluted 1:400; Chemicon) and microglia (anti-rabbit Iba1, diluted 1:1000; Wako Chemicals, Germany). Next, the samples were rinsed and incubated for 1 hour at 25°C in a solution containing Alexa 488 and Alexa 594 secondary antibodies respectively (diluted 1:500 with PBS containing 0.3% Triton-X, Molecular Probes). After additional rinsing, samples were mounted onto slides with a drop of 90% glycerin in PBS. Immunohistochemical images were evaluated using Improvision software (Source: NIH). The densities of GFAP and Iba1 Immunoreactivity were calculated using NIH image software and expressed as mean gray density. Values obtained from four tissue sections of each rat were averaged to obtain one number. Averaged numbers for each time point were analyzed using a one-way ANOVA followed by Dunnet's post hoc test. Significance was defined as $p < 0.5$.

2.13 Drugs and Reagents

Unless otherwise stated, drugs and reagents were used as received. Calcium chloride dihydrate, Citrisolv™, ethanol (70%), isopropyl alcohol, Micro-90 Cleaning solution, paraformaldehyde, phosphoric acid, potassium chloride, sodium chloride, sodium hydroxide, sodium dihydrogen phosphate, sodium hydrogen phosphate and Urethane were obtained from Fisher Scientific (Fair Lawn, NJ). Hydrogen peroxide (3% H_2O_2 topical solution) was purchased from Rite Aid. L-glutamate oxidase was purchased from Seikagaku America, Inc. Ascorbate, bovine serum albumin (fraction IV), Congo red dye, cresyl violet dye, Fast Green dye, Gluteraldehyde (25%), 3-Hydroxytyramine hydrochloride (Dopamine, DA), L- glutamate monosodium salt, Nafion® (5% in a mixture of aliphatic alcohols and water) and 1, 3-phenylenediamine dihydrochloride (mPD) were obtained from Sigma (St Louis, MO). Isoflurane and Rimadyl™ (Carprofen) were provided by the University Of Kentucky Division Laboratory of Animal Resources. The molecular stoichiometry for the above-described molecules was selected on the basis of detailed parametric studies. All solutions were prepared using distilled, deionized water. Solutions prepared for *in vivo* applications were passed through a 0.22 μm filter (Costar, Corning, NY) to minimize particulate obstruction of the micropipettes.

Copyright © Pooja Mahendra Talauliker 2010

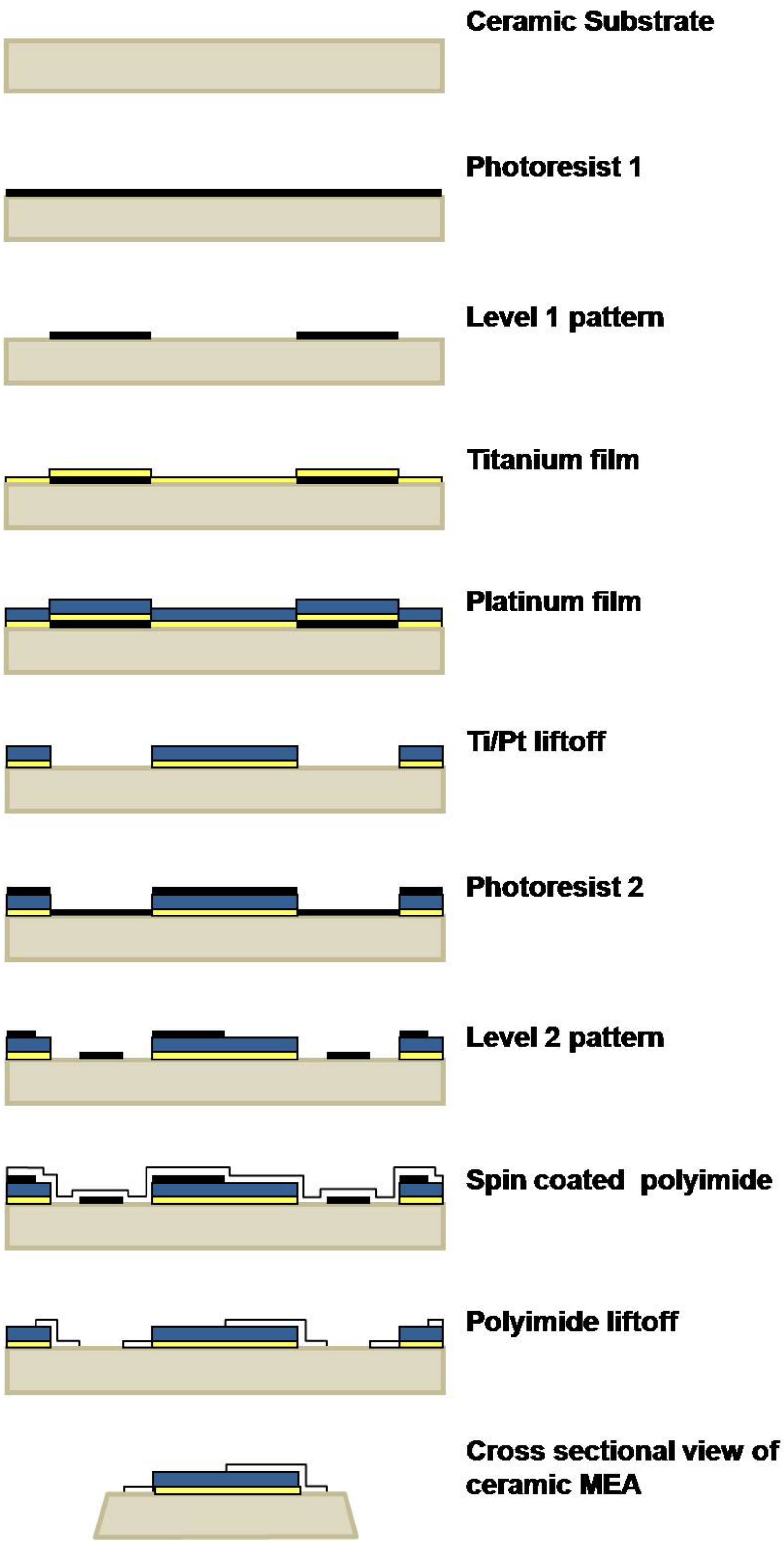
Ceramic Substrate
Photoresist 1
Level 1 pattern
Titanium film
Platinum film
Ti/Pt liftoff
Photoresist 2
Level 2 pattern
Spin coated polyimide
Polyimide liftoff
Cross sectional view of ceramic MEA

Figure 2.1: MEA fabrication using photolithography

Figure 2.1 (contd.): MEAs are manufactured with high reproducibility using a series of photoresist layers and coating masks. The 99% pure Titanium and Platinum layers are deposited onto the wafer to define recording sites, connecting lines, and bonding pads. With the exception of the Pt sites, all circuitry is protected from aqueous environments by spin-coating polyimide onto the surface. Lastly, a diamond saw was used to pattern MEA tips with smooth edges. (Figure adapted from Burmeister et al., 2001)

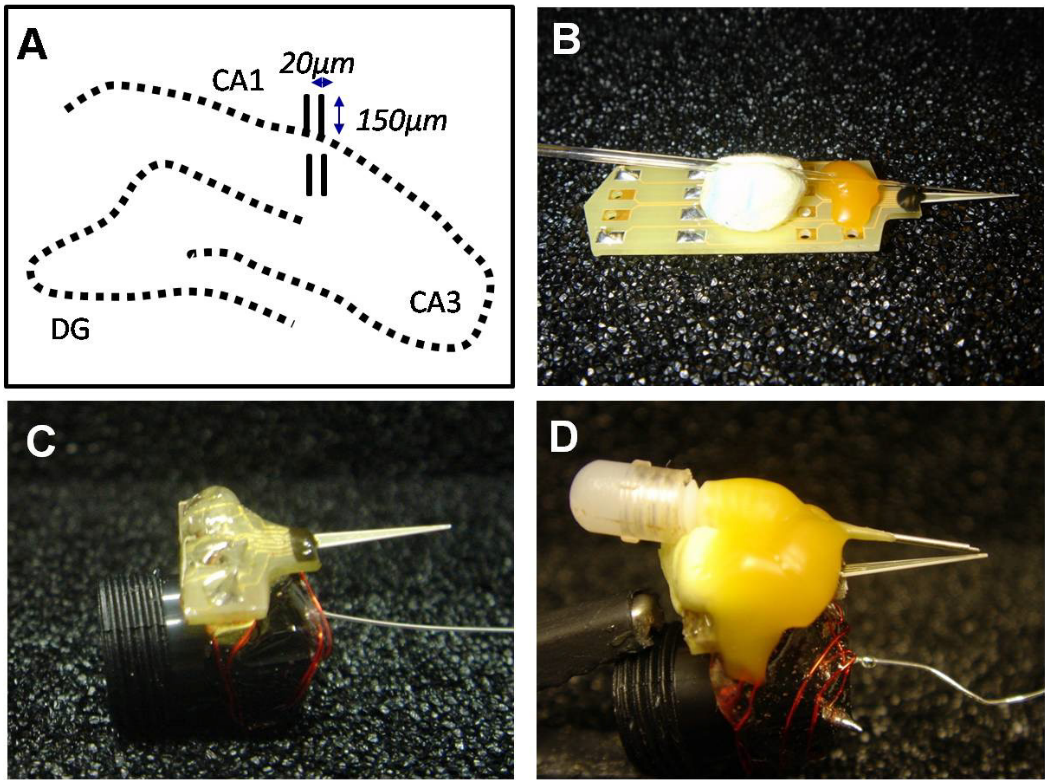

Figure 2.2: W4-MEA configured for neurotransmitter recordings in anesthetized and unanesthetized animals. Panel A is a schematic of the W4 MEA. The Pt sites (20 µm x 150 µm) arranged in dorsal-ventral pairs, allowing for accurate targeting of DG, CA3 and CA1 subregions. Panel B is a photograph of a W4-MEA bonded to a PCB. A glass micropipette is positioned between the four Pt sites at a distance of 60 – 80 µm for local application of intracranial solutions. Panel C shows a W4-MEA with a modified PCB for chronic studies in unanesthetized rats. For glutamate recordings, a stainless steel cannula system is attached between to the MEA tip with Kerr wax (Panel D).

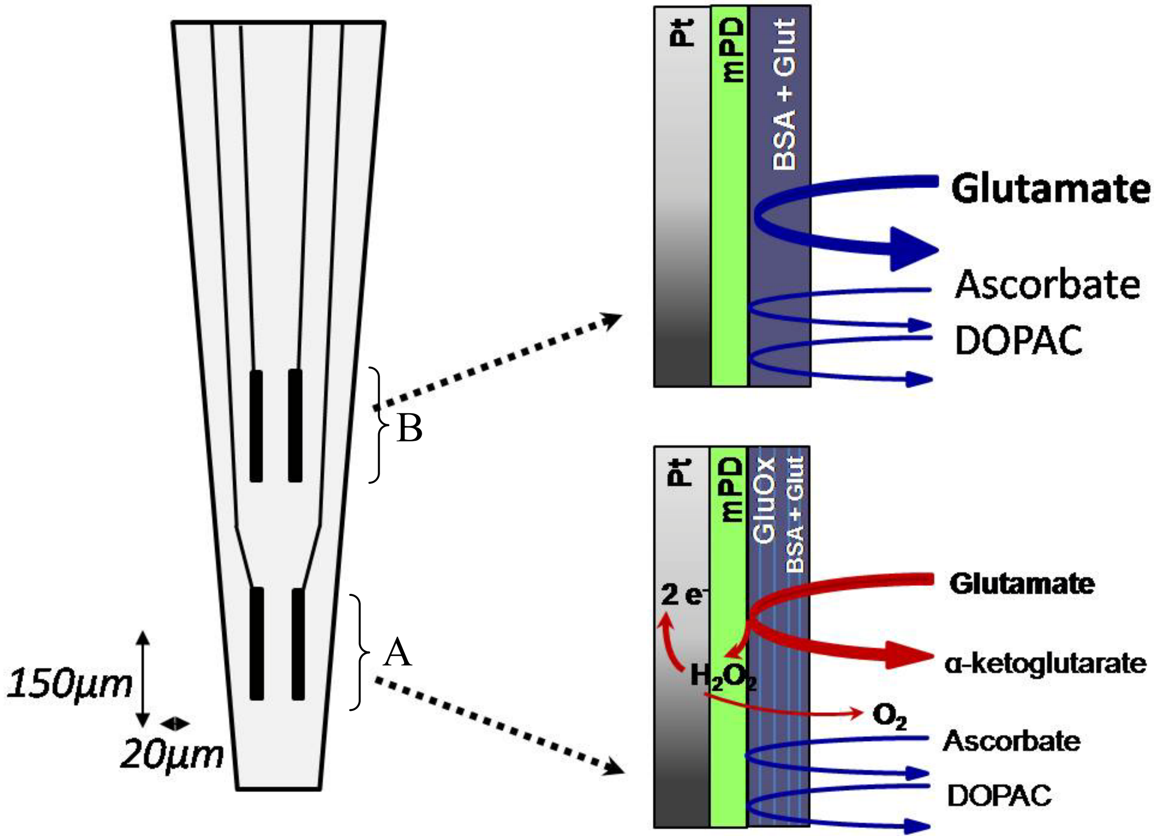
Pt
mPD
BSA + Glut
Glutamate
Ascorbate
DOPAC
B
Pt
mPD
GluOx
BSA + Glut
2 e⁻
Glutamate
α-ketoglutarate
H₂O₂
O₂
Ascorbate
DOPAC
A
150µm
20µm

Figure 2.3: W4 MEA configured for self-referenced glutamate measurements. Poly-metaphenylenediamine (poly-mPD) acts as a size-selective exclusion layer against electroactive interferent molecules such as Ascorbate, Dopamine and DOPAC. Site pair A was configured for glutamate detection with a manual coating of glutamate oxidase (GluOx), bovine serum albumin (BSA) and gluteraldehyde (Glut). Site pair B was coated with an inactive solution of BSA and Glut. Enzymatic breakdown of glutamate produces hydrogen peroxide (H_2O_2) 'reporter' molecules. Current (at +0.7 V vs. Ag/AgCl reference electrode) from glutamate is determined by subtraction of current measured by Site pair B from Site pair A. This recording strategy is known as self-referencing.

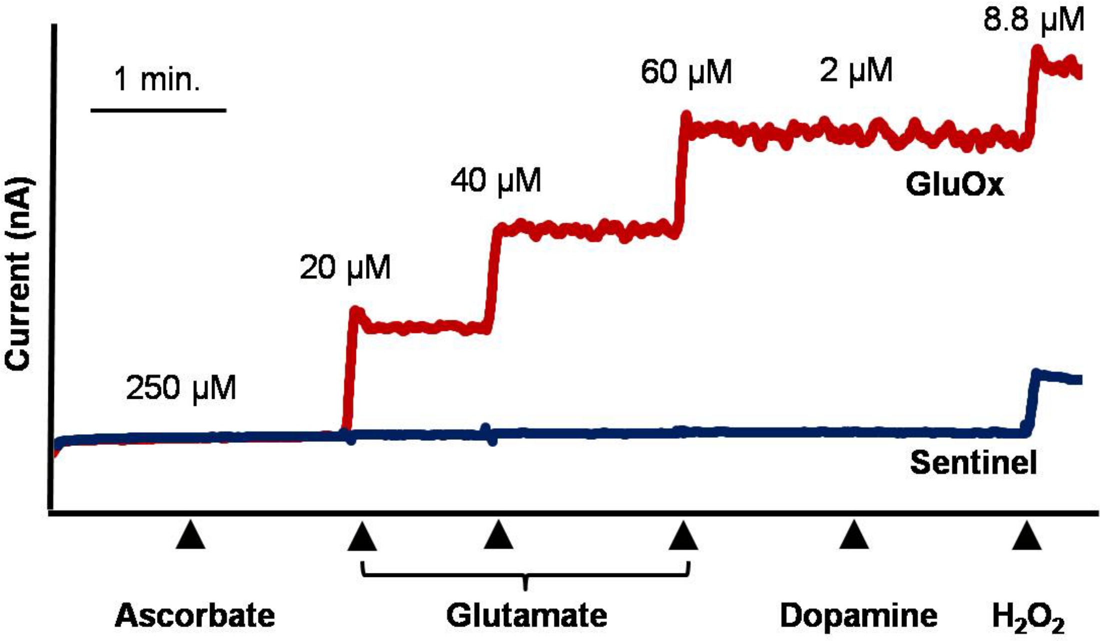

Figure 2.4: Calibration of W4-MEAs. The tip of the MEA is submerged in 0.05 M PBS (40 ml stirred solution, pH 7.4, 37°C) and maintained at +0.7 V vs. an Ag/AgCl reference electrode. A standard response curve is generated by adding serial aliquots of 20 mM glutamate solution to produce final beaker concentrations of 20, 40 and 60 µM. The resulting increase in oxidation current (pA) is used to determine the slope (nA·µM-1) of the curve and the limit of glutamate detection (3 x RMS noise on the baseline signal). MEA selectivity is determined using a 250 µM ascorbic acid challenge. At the end of calibration, recording site sensitivity (or lack thereof) to Dopamine (DA) and hydrogen peroxide (H_2O_2) was verified (negative and positive controls, respectively).

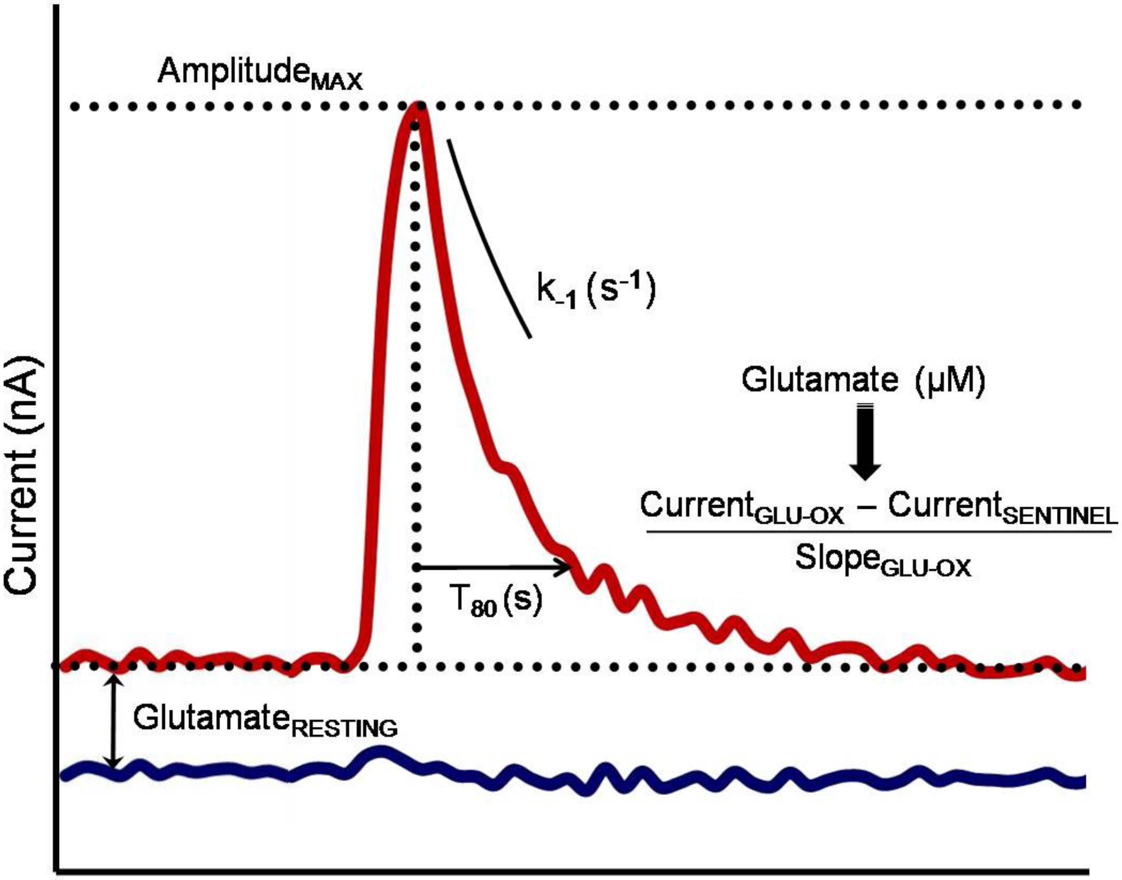

Figure 2.5: Signal characteristics for MEAs. Extracellular glutamate concentration (µM) is calculated by subtracting the current measured by the 'sentinel' sites from glutamate oxidase (GluOx) coated sites, and dividing the difference by the slope of the GluOx site (obtained during calibration). This is useful for obtaining resting levels of glutamate (Glutamate$_{RESTING}$), maximum increase in glutamate concentration following local application of KCl solution (Amplitude$_{MAX}$), and the rate of glutamate clearance (Uptake rate = k_{-1} x Amplitude$_{MAX}$). Clearance is also measured in terms of time (s) to signal decay, for e.g., time taken for signal to decay by 80% from maximum amplitude, or T_{80}.

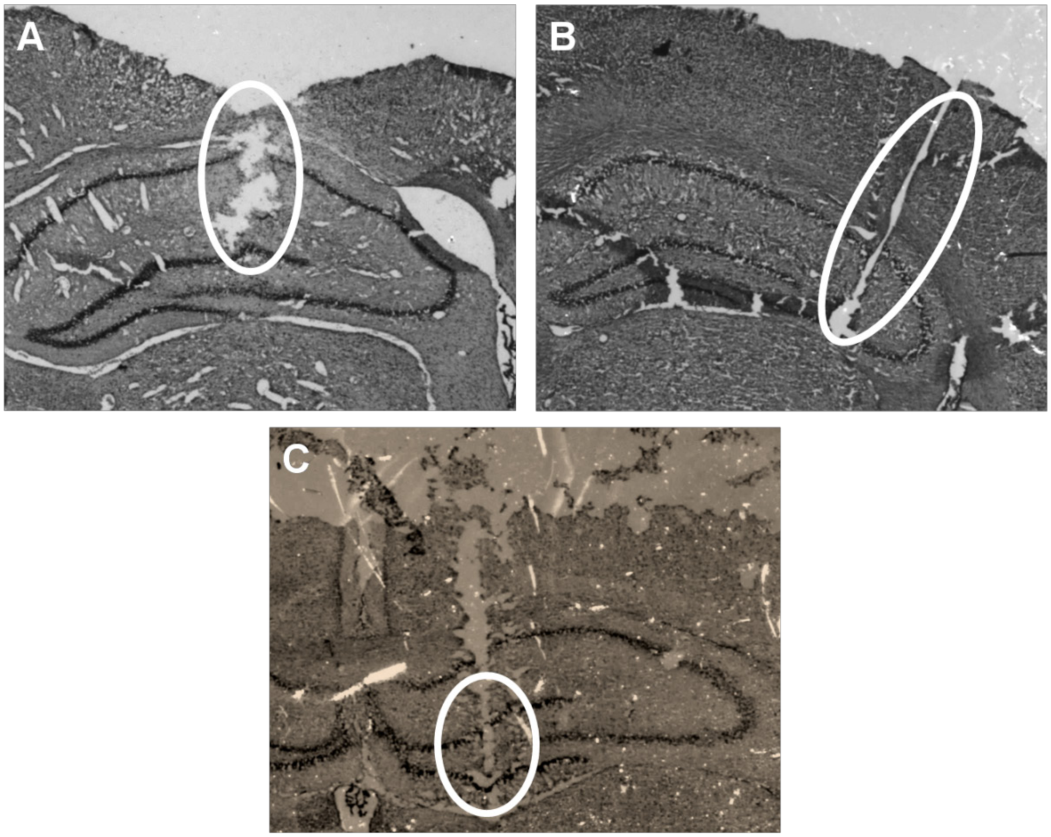

Figure 2.6: Electrode placement verification in the rat hippocampus. Cresyl violet stained sections showing the location of the electrode track in the CA1 (A), CA3 (B) and DG (C) respectively.

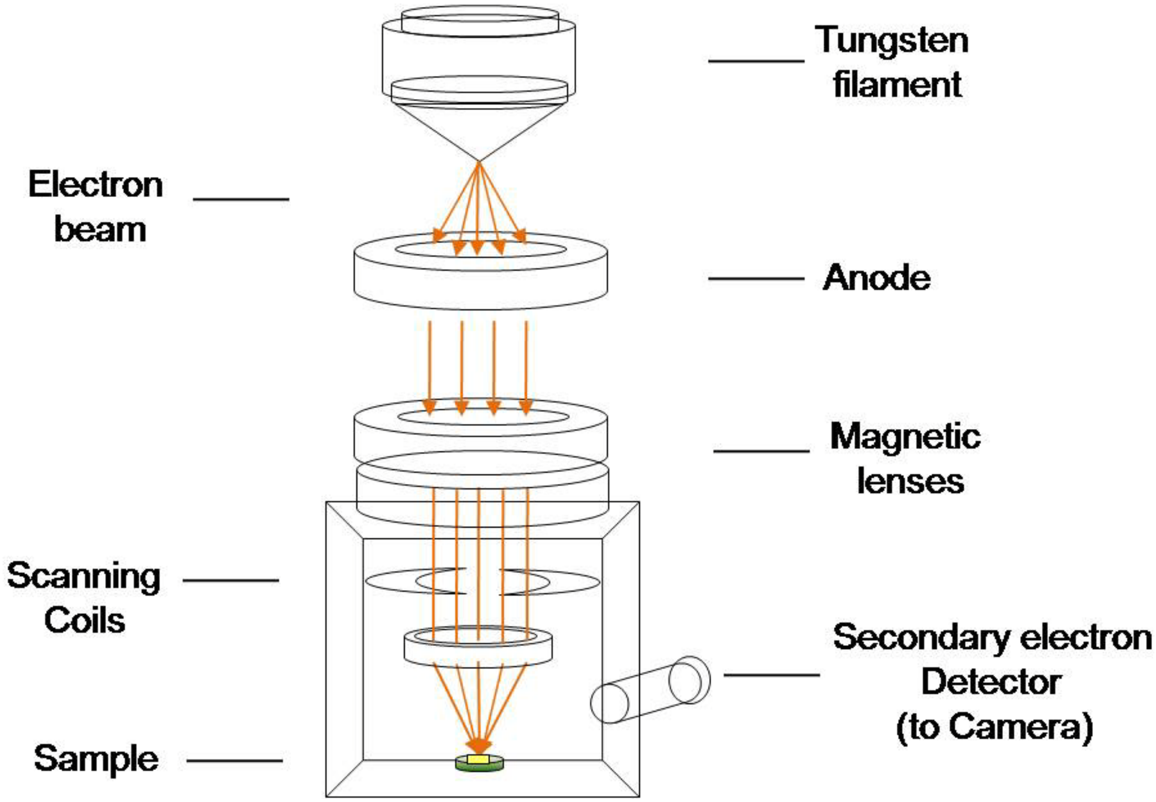
Tungsten filament
Electron beam
Anode
Magnetic lenses
Scanning Coils
Secondary electron Detector (to Camera)
Sample

Figure 2.7: MEA surface imaging using scanning electron microscopy. Electrons emitted by the heated tungsten filament are focused and redistributed by a series of lenses and coils to allow scanning of a sample surface in a raster fashion. When the electron beam interacts with the ceramic surface, displacement of secondary electrons located a few nanometers beneath the sample surface is measured by a secondary electron detector. For viewing purposes, scanning data of the imaged surface is amplified, digitized and expressed in terms of variations in gray levels. (Figure adapted from Encyclopedia Brittanica, 2008)

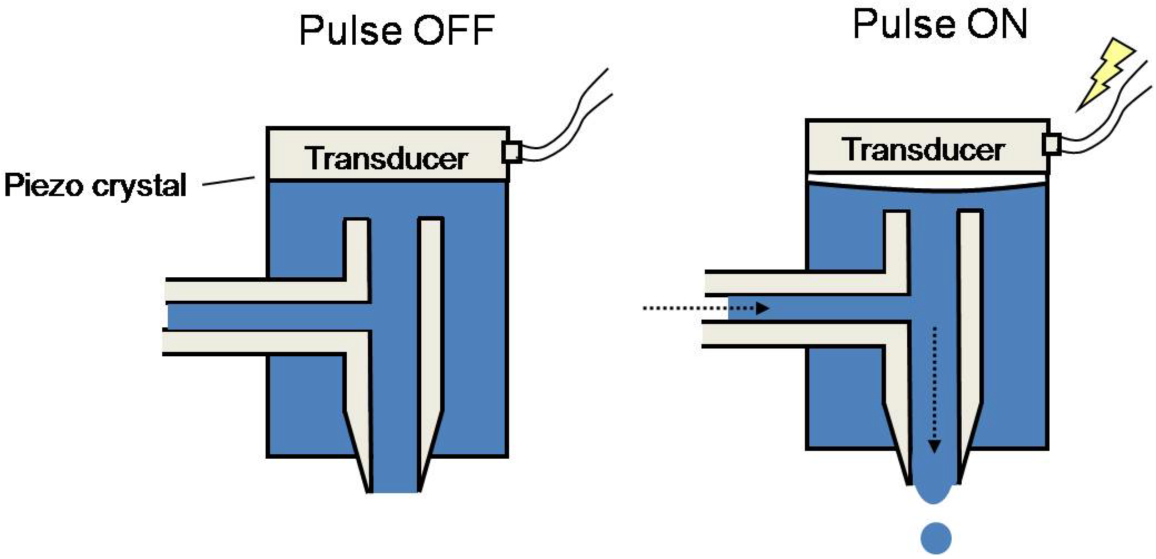
Pulse OFF
Pulse ON
Piezo crystal
Transducer
Transducer

Figure 2.8: Basic properties of piezo-based inkjetting of solutions. Application of a controlled intermittent voltage pulse causes mechanical deformation of the crystal element, forcing the release of fluid droplets through the nozzle.

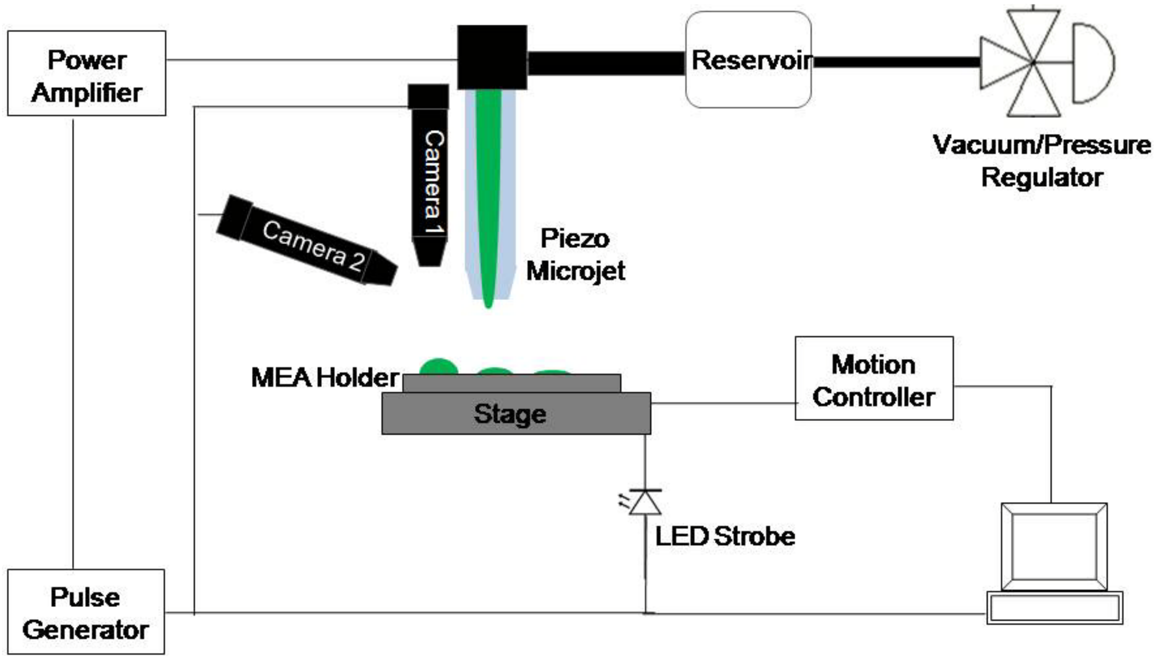
Power Amplifier
Reservoir
Vacuum/Pressure Regulator
Camera 1
Camera 2
Piezo Microjet
MEA Holder
Stage
Motion Controller
LED Strobe
Pulse Generator

Figure 2.9: Schematic illustration of JetLab4 microprinting system. The Jetlab® 4 microprinting station (Microfab Technologies, Plano, TX) printing assembly is comprised of an array of piezoelectric jetting devices (MicroJets®, Microfab Technologies, Plano, TX) and the fluidic and electrical components necessary for driving the ejection of droplets from the devices. It also contains translation stages to control substrate position in the x, y and z directions (Sutter Instrument Co., CA), and a visualization system for controlling droplet placement. The jetting device is a capillary glass tube pulled to an orifice diameter of 50 µm and is encased inside a piezoelectric transducer and protective metal housing. A pneumatics controller (MicroFab Technologies, Plano, TX) and pressure/vacuum pump (Gast Manufacturing, Benton Harbor, MI) is integrated into the system for regulation of backpressure regulation. All jetting parameters can be controlled through the software program. (Image adapted from Lei et al., 2002).

Table 2.1 Stereotaxic Coordinates for Hippocampal Subregions

	Anterior - Posterior (mm)	Medial – Lateral (mm)	Dorsal – Ventral (mm)
Dentate Gyrus (DG)	-4.0 ± 0.2	± 3.0 - 3.3	-3.6 ± 0.2
Cornu Ammonis 1 (CA1)	-4.0 ± 0.2	± 3.0 - 3.3	-3.0 ± 0.2
Cornu Ammonis 3 (CA3)	-4.0 ± 0.2	± 3.5 - 3.8	-4.0 ± 0.0

Average animal weight = 300.0 g ± 28.0 g

n = 7 for each subregion, $n_{ANIMALS}$ = 21

Obtained from Paxinos and Watson, 2005

Chapter Three: Real-time Measurements of Glutamate Neurotransmission in the Hippocampal Trisynaptic Pathway of F344 Rats

3.1 Introduction

During the past three decades, the hippocampus has been intensively studied for its vital role in cognitive learning and memory formation. Though much is known about the structural and functional properties of neurons localized to this brain region, an understanding about how afferent information to the hippocampus is processed at a cellular level and encoded as a new memory or learned behavior is necessary (for review, see Szapiro et al., 2002; Richter and Klan, 2009). The hippocampus is susceptible to a number of physiological and functional changes during aging (Segovia, 2001) and is one of the first structures to be affected during age-related onset of Alzheimer’s disease (Francis et al., 2003; Armstrong et al., 2003). It is also extremely vulnerable to tissue damage from hypoxic-ischemic injury (Ashton et al., 1989; Leifer and Kowall, 1993) and recurrent seizures (Meldrum and Chapman, 2000; Chapman et al., 2001). To aid the development of diagnostic tools and appropriate treatment paradigms for this important brain region, knowledge about the molecular mechanism(s) involved in these pathologies is also needed.

Glutamate is the dominant excitatory neurotransmitter in the brain and hippocampus (Danbolt, 2001). Cellular communication between principal hippocampal neurons is excitatory, mediated by ionotropic glutamate receptors of AMPA and NMDA-sensitive subtypes (for review see Malenka and Nicoll, 1993). These receptors also mediate long-lasting changes in synaptic strength through a process termed long term potentiation or LTP (Andersen et al., 2007). LTP is widely suggested to be the anatomical substrate for cognitive learning, while the resulting change in the synapse has been hypothesized to represent encoded ‘memory’ (Angulo et al., 2004; Albensi et al., 2007). Metabotropic glutamate receptors (mGluRs) have also received significant attention for their modulatory effects on LTP (Anwyl, 1999, 2009) and long term depression (LTD) (Kemp and Bashir, 1999).

It is important to note that glutamate is regulated by a highly efficient uptake system. This ensures precise activation of glutamate's post-synaptic targets (Sonnewald, Westergaard and Schousboe, 1997). Overexposure to glutamate through uncontrolled release or loss of effective clearance mechanisms causes a pattern of neuronal death and tissue damage that is uniquely identifiable in histological tissue sections (Martin et al., 1998). Particularly in the hippocampus, excitotoxic damage is a hallmark of recurrent seizure activity and thought also to be a large contributor to hypoxic-ischemic injury (Danbolt, 2001, Scimemi et al., 2006). Collectively, these findings highlight the importance of proper glutamate regulation for normal hippocampal function.

Much of our present understanding about the neurotransmitter role of glutamate comes from electrophysiological investigations conducted in *ex vivo* tissue such as hippocampal slices, isolated nerve terminals and cell cultures (Nicholl et al., 1993; Hjelmstad et al., 1997; Takeda et al., 2007). Often, data obtained from these studies is inconsistent, partly due to variations in the experimental methodology followed by different research groups, but more likely due to the inherent limitations of studying a brain region without its complete set of intrinsic and extrinsic connections. More importantly, electrophysiology does not allow for direct measurement of glutamate concentration. *In vivo* recordings in the intact hippocampus using microdialysis probes have found some success in measuring tonic glutamate concentration in whole tissues (Bagley and Moghaddam, 1997; Clapp-Lilly et al., 1999) but this methodology also has important limitations. Dynamic properties of glutamate neurotransmission cannot be investigated in microdialysis recordings because the slow sampling rates of this technique (minutes) cannot capture the rapid glutamate release and uptake (milliseconds) events. Measurements of tonic glutamate alone are inadequate because subtle changes in synaptic connectivity may be masked by homeostatic compensation, an expected biological mechanism in most *in vivo* investigations.

Microdialysis probes also cause extensive damage to surrounding brain parenchyma (Clapp-Lilly et al., 1998) due to their large size (0.38 mm).

The size of the microdialysis probe also limits subregional investigations in the hippocampus, which in rodents, is only a few millimeters wide (Paxinos and Watson, 2005). Though the cytoarchitectonically distinct dentate gyrus (DG), cornu ammonis 3 (CA3) and cornu ammonis 1 (CA1) fields of the hippocampus operate in a concerted fashion in the normal brain, evaluation of glutamate regulation in discrete subregions is needed because they are distinct with respect to synaptic connectivity, surface distribution of glutamate receptors and mRNA content (Gegelashvili et al., 1998; Wilson et al., 2005; Greene et al., 2008). In addition to the observation that subregions demonstrate unequal susceptibility to pathological insults (Amaral et al, 1971; Andersen et al., 2007), behavioral testing implicates a different role for dorsal and ventral hippocampal regions with respect to cognitive learning and memory encoding (Kesner and Hopkins, 2006). Since information relay in the hippocampal trisynaptic pathway takes places through a series of excitatory connections, we hypothesize that differential regulation of glutamate neurotransmission within the DG, CA3 and CA1 fields contributes to the observed regional differences in hippocampal function and disease vulnerability. A scientific study of these potential differences, to our knowledge, has not been conducted.

To address this need, we developed a novel MEA design (W4 MEA) comprised of four Pt surfaces (20 X 150 μm) arranged in dorsal-ventral pairs (shown in Figure 2.1 in Chapter Two). The total recording area of this design (3000 μm^2) is approximately 40% smaller than our standard MEA design, ideal for targeted measurements in the cytoarchitectonic layers of the rat hippocampus. In the present studies, W4 MEAs were configured for selective glutamate detection and coupled with amperometry to obtain subsecond (2 Hz) neurotransmitter recordings, similar to our previous studies in rodents and non-human primates (Burmeister et al., 2002, 2003, Nickell et al., 2006; Thomas et al., 2009; Quintero et al., 2008). *In vivo*, the W4 MEA's recording sites were targeted to cell layers containing the dendrites of hippocampal principal neurons in the each subregion, specifically the infrapyramidal molecular layer of the DG, the stratum lucidum of CA3 field and the stratum radiatum of the CA1 field. These locations correspond to synapses 1, 2 and 3 of the hippocampal trisynaptic circuit, respectively. Accurate placement was achieved by stereotactic placement in brain tissue and verified post-experimentally from MEA track locations. First, resting (tonic) levels of extracellular glutamate were determined in the DG, CA3 and CA1 subregions using a dual recording strategy that allowed isolation of electrochemical signals corresponding to glutamate measurements (Day et al., 2006; Thomas et al., 2008). Secondly, we investigated phasic glutamate release from nerve terminals localized to the DG, CA3 and CA1 by delivering either 70 mM or 120 mM potassium solution (KCl) through a micropipette attached to the W4 MEA (Thomas et al., 2008). These experiments were conducted to evaluate subregional capacities for KCl-evoked glutamate release under different depolarizing conditions. The temporal properties of stimulus-evoked glutamate release were evaluated from the rising portion of glutamate signals. Subregional capacity for glutamate uptake was determined by local applications of exogenous glutamate (100 μM) and subsequent evaluation of signal decay. Finally, a depth profile of hippocampal glutamate levels was obtained by measuring resting levels of glutamate and 70 mM KCl-evoked glutamate release in the CA1 (stratum oriens and radiatum) and in DG (suprapyramidal molecular layer, polymorphic layer and infrapyramidal molecular layer).

The acute experiments conducted in this study are important because they validated the capability of the W4 MEA to provide novel data about real-time glutamate neurotransmission from discrete subregions of the hippocampus. Future studies on subregional regulation of hippocampal glutamate will probably be conducted in unanesthetized rats because these experiments offer the potential to correlate regulation of glutamate neurotransmission with hippocampal dependent learning. Additionally, glutamate measurements from unanesthetized rats may provide a unique perspective on alterations in excitatory neurotransmission during hippocampal aging and disease that is not available through conventional recording methodologies. To date, we have successfully adapted the standard MEA design for chronic glutamate measurements in the prefrontal cortex of freely moving rats and mice (Rutherford et al., 2007). Therefore, a second goal of these studies was to evaluate the chronic recording capability of W4 MEAs following implantation in the CA1 subregion of the rat hippocampus.

3.2 Materials and Methods

Please refer to Chapter Two for a detailed description of animal care, MEA preparation, recording methodology for *in vitro* and *in vivo* amperometry, histology procedures, post-experimental data processing and statistical analysis.

3.3 Results (I): Glutamate Recordings in the Anesthetized Rat Hippocampus

3.3.1 Resting Levels of Extracellular Glutamate in the Hippocampal Trisynaptic Circuit

Our MEA technology utilizes a dual recording strategy to allow subsecond (2 Hz) resting or tonic measurements of extracellular glutamate. This temporal resolution, along with the W4 MEA's capability to target discrete cytoarchitectonic layers within subregions of the rat hippocampus is an important advancement over previous MEA designs and is unparalleled in current scientific literature. In the present studies, resting glutamate was reliably measured in discrete hippocampal subregions in F344 rats, specifically the infrapyramidal molecular layer of the DG, the stratum lucidum of CA3 field and the stratum radiatum of the CA1 field. Average resting glutamate levels are seen in Figure 3.1: DG (2.9 μM ± 0.4, n = 15); CA3 (3.3 μM ± 0.6, n=15); CA1 (2.6 μM ± 0.3, n = 16). These data indicate that resting glutamate is not significantly different {F(2, 43) = 0.3, p = 0.7} across the trisynaptic circuit in urethane-anesthetized rats.

3.3.2 KCl-evoked Glutamate Release in the Rat Hippocampus

Application of nanoliter volumes (12.5 – 50.0 nL) of 70 mM or 120 mM KCl (isotonic, pH 7.4) resulted in stimulation of the extracellular environment adjacent to the MEA. This allowed us to investigate glutamate release from nerve terminals in the discrete DG, CA3 and CA1 subregions of the rat hippocampus. Repeated ejections of 70 mM KCl (lasting 0.5 s) in the DG, CA3 and CA1 resulted in robust volume-dependent increases in glutamate signal amplitude (4 - 80 μM) relative to baseline concentration (Figure 3.2 A). In each region, glutamate signals were transient (5 – 12 s) and reproducible (every 60 seconds). Figure 3.2 B shows average glutamate signal amplitudes in the DG (17.5 μM ± 3.9), CA3 (7.4 μM ± 0.4) and CA1 (16.0 μM ± 1.1) (n = 7 per region). Thus, KCl-evoked glutamate signals were significantly smaller in the CA3 field ($p < 0.05$, F(2, 18) = 6.6) compared to the DG and CA1 subregions of the rat hippocampus. The variances of these data were significantly different with Bartlett's test $p < 0.0001$.

Local application of 120 mM KCl in the DG, CA3 and CA1 hippocampal fields revealed further differences in subregional glutamate release capacity. Figure 3.3 A, B shows representative signals and average glutamate signal amplitudes for the DG (6.9 μM ± 1.4), CA3 (3.3 μM ± 1.4) and CA1 (17.7 μM ± 1.2) (n = 6 per region). Glutamate release was reproducible in the CA1 field and glutamate signals measured in this subregion were the largest in the anesthetized rat hippocampus. As before, glutamate signals were significantly smaller in the CA3 ($p < 0.001$, F (2, 11) = 29.8). However, in approximately 50% cases, we observed a complete suppression of glutamate release in the CA3 after repeated application 120 mM KCl ejections. This effect lasted for more than 90 minutes and was also observed in the contralateral CA3 field.

Interestingly, glutamate release was significantly diminished in the DG ($p < 0.001$, F (2, 11) = 29.8). Diminished capacity for glutamate release was also significant relative to 70 KCl evoked stimulation (t(7) = 2.9, p = 0.02, F-test p = 0.44) (Figure 3.4). Collectively, these data suggest that terminal glutamate release is dependent upon KCl concentration and is regulated differently in subregions of the rat hippocampus.

3.3.3 Rise Time of Glutamate Signals following KCl Stimulation in Hippocampal Subregions

Because the time taken to reach maximum signal amplitude, or rise time (T_{RISE}), is an important temporal indicator of glutamate neurotransmission, KCl-evoked glutamate signals from each subregion were evaluated with respect to this kinetic parameter. In these analyses, glutamate signals resulting from 120 mM KCl stimulation in the CA3 were excluded because a majority of the signal amplitudes did not satisfy the defined signal selection criteria (signal amplitudes in the range 8-15 µM).

Figure 3.5 (inset) shows average T_{RISE} in the DG (1.7 s ± 0.2), CA3 (2.0 s ± 0.4) and CA1 (1.7 µM ± 0.2) (n = 6 per group) hippocampal subregions following 70 mM KCl stimulation, and in DG (1.1 s ± 0.1) and CA1 (1.3 s ± 0.2) subregions following 120 mM KCl stimulation. Comparison across subregions and between treatment groups revealed that T_{RISE} was significantly smaller ($p<0.05$) in the DG following stimulation with 120 mM KCl ($t(6) = 2.63$, $p = 0.04$). This result is illustrated in Figure 3.5 by superimposing representative glutamate signals from DG recordings. It is important to note that differences (or lack thereof) in T_{RISE} were not caused by variability in experimental factors such as the distance of the micropipette from the MEA or the relative position of the micropipette tip from the recording sites. Together with the evoked-release data, these results show that the temporal properties of glutamate release in the CA1 and CA3 fields are unaffected by KCl concentration; however, in the DG subregion, diminished glutamate release following at high KCl concentration is accompanied by faster glutamate signaling.

3.3.4 Glutamate Clearance Capacity in Subregions of the Rat Hippocampus

Evaluation of the robust decay of glutamate signals is an important goal of these studies because it is indicative of glutamate transporter activity. Glutamate release and clearance are dynamic, overlapping processes. Therefore, it is not possible to completely isolate the clearance phase from KCl-evoked glutamate signals. In addition, KCl stimulation is non-specific, resulting in the co-release of several modulatory neurochemicals in addition to glutamate. These limitations were avoided by locally applying an exogenous glutamate solution (100μM in 0.9% saline, pH 7.4) into the DG, CA3, and CA1 discrete hippocampal regions. Also, electrogenic glutamate transporters are known to behave in accordance with first order Michaelis-Menten kinetics. Therefore, subregional capacities for physiological glutamate release were mimicked by applying solution volumes in the range 25-150 nL. Statistical comparisons were made on amplitude-matched data (6-15 μM) to ensure that variations in glutamate signal amplitude would not contribute to changes in uptake rate. Average rates of glutamate uptake were not significantly different {F(2,17) = 0.68, p = 0.52} between the DG (1.8 μM·s^{-1} ± 0.6), CA3 (1.1 μM·s^{-1} ± 0.3) and CA1 (1.7 μM·s^{-1} ± 0.5) (n = 6 per group) regions, though a trend for slower uptake was observed in the CA3 field (Figure 3.6). These data indicate that the activity of glial and neuronal excitatory amino acid transporters is comparable in hippocampal subregions in anesthetized F344 rats.

3.3.5 Depth Profile of Resting Glutamate and Stimulus-evoked Glutamate Release in the Rat Hippocampus

The final experiments of the present study involved depth measurements of hippocampal resting glutamate in the stratum oriens and radiatum of the CA1 field and the suprapyramidal molecular, polymorphic and infrapyramidal molecular layers of the DG. As shown in Figure 3.7, average resting glutamate levels were not significantly different between discrete cell layers in urethane anesthetized rats. {F(4,17) = 0.3, p = 0.8, n = 3}.

Lastly, Figure 3.8 shows average glutamate signal amplitudes obtained at each depth following repeated injections of 70 mM KCl (25 nL). Glutamate release capacity was significantly larger in the stratum radiatum (12.7 μM ± 0.3) than the stratum oriens (5.2 μM ± 0.5, $p<0.0001$) of the CA1 field (Figure 3.3). Similarly, the infrapyramidal molecular layer of the DG had the largest signals (13.5 μM ± 0.8) compared to the suprapyramidal molecular layer (7.2 μM ± 0.6) and the polymorphic cell layer (6.3 μM ± 0.6), {$F(4,17)=45.55$; $n = 3$ per group}. Thus, the rat hippocampus demonstrates depth-related differences in glutamate release capacities that are significant both within and between subregions.

3.4 Discussion: Studies of Glutamate in the Anesthetized Rat Hippocampus

In this study, we have shown that tonic glutamate levels in the discrete DG, CA3 and CA1 subregions of the hippocampus are not significantly different in anesthetized F344 rats. However, the trisynaptic pathway does exhibit stimulus-dependent changes in KCl-evoked glutamate release in specific subregions. Of the three subregions, stimulus-evoked release of glutamate with 70 or 120 mM KCl was significantly greater from terminals localized to the CA1 field. In contrast, glutamate release was significantly lower in the CA3 subregion. These data suggest that less glutamate was found in the extracellular space around the MEA in the CA3 region. The most fascinating findings in this study were from KCl studies in the DG subregion. KCl-evoked glutamate release capacity in DG terminals was significantly diminished following high K^+ stimulation but demonstrated faster release kinetics, providing evidence for modulation of presynaptic glutamate release from local nerve terminals. Clearance of exogenous glutamate was not significantly different in the DG, CA3 or CA1 subregions, suggesting similar capabilities for glutamate clearance in the trisynaptic circuit. Finally, depth profile investigations of hippocampal layers in the CA1 and DG demonstrated cell layer-specific differences in evoked glutamate release capacity, as seen with local application of 70 mM KCl. Collectively, these findings validate the capability of the W4 MEA to target discrete cell layers of the rat hippocampus and provide direct evidence for subregion specific regulation of glutamate neurotransmission in the anesthetized rat hippocampus.

3.4.1 Resting Levels of Extracellular Glutamate are Similar throughout the Hippocampal Trisynaptic Circuit in Anesthetized Rats

Previous studies report resting levels of hippocampal glutamate between 1 and 5 µm (Miele et al., 1996; Zhang et al., 2004), obtained by *in vivo* microdialysis measurements. However, due to the relatively large size of microdialysis probes, current scientific literature is lacking in resting glutamate data for individual subregions of the hippocampus. The present studies used a novel MEA design to obtain resting glutamate measurements from discrete regions of the adult rat hippocampus and showed that extracellular glutamate was not significantly different in the DG, CA3 and CA1 subregions. Averaged across the three subregions, our resting glutamate levels are comparable with previous microdialysis data. However, recent studies from our laboratory suggest that urethane anesthesia can alter basal glutamate in the prefrontal cortex (Rutherford et al., 2007). Further investigations in unanesthetized rats are needed to address this issue.

3.4.2 Capacity for Stimulus-evoked Glutamate Release is Different in Hippocampal Subregions

Since the temporal resolution of our MEA technology is an order of a magnitude faster (0.5 s) than the most advanced microdialysis technique (6s) (Kennedy et al, 2002, Rossell et al., 2003), the W4-MEA can measure extrasynaptic spillover of endogenous glutamate from depolarized nerve terminals following KCl stimulation. The experiments described in this study validated this recording capability and also showed that the W4-MEA can detect micromolar differences in KCl-evoked release of glutamate in discrete hippocampal subregions.

We showed that stimulation with 120 mM KCl (but not 70 mM KCl) resulted in decreased glutamate release capacity in the DG subregion. Only one previous study has directly measured glutamate release in the DG region of the rat hippocampus with KCl stimulation (Hu et al., 1994). Their study showed that stimulus-evoked glutamate signals were reproducible in the DG provided a rest period of 20 minutes was allowed between consecutive applications (~1000 nL) of 100 mM KCl solution. Yu and colleagues reasoned that this refractory period was caused by depletion of vesicular glutamate stores in presynaptic nerve terminals. The present study does not support this rationale because glutamate signals can be produced every 60 seconds with 70 mM KCl stimulation. Interestingly, high frequency electrical stimulation of DG tissue for short periods of time (seconds to minutes) has been shown to cause reversible inactivation of afferent glutamatergic fibers (Kwon and Castillo, 2003). It is possible that excessive stimulation with high concentration KCl solution produce a similar effect in our studies. If so, our finding that attenuation of terminal glutamate release in the DG subregion takes place after repeated depolarization with high K^+ levels supports a role for presynaptic modulatory mechanisms. This is a fascinating finding because activation of presynaptic mGluRs (group II and III) in the DG has been shown to inhibit long term potentiation (LTP) and facilitate short term depression (STD) in hippocampal tissue slices (Kew et al., 2000, Klausnitzer, Kulla and Manahan-Vaughan, 2003). Blockade of the same autoreceptors adversely affects long term depression (LTD) (Kilbride et al., 1998, 2001). LTP and LTD have been extensively studied by electrophysiologists because long lasting changes in synaptic strength are believed to be critical for hippocampal-dependent learning (for review on Morris et al., 2003; Lynch, 2004) and proposed to be functional equivalents of memory formation (Andersen et al., 2007). Moreover, impaired cognition is an area of intense interest in studies of aging (Gallagher and Nicolle, 1993, Nagahara et al., 2008) and age-related onset of Alzheimer's disease (Ackl et al., 2005; Lupien et al., 2009). For future investigations, an experimental paradigm that combines real-time glutamate measurements with our MEAs and pharmacological manipulation of presynaptic mGluRs offers the greatest potential for understanding regulation of glutamate neurotransmission in DG function.

The present experiments also showed that glutamate release in the CA3 subregion was significantly lesser than the DG and CA1 hippocampal fields. To our knowledge, direct *in vivo* investigations of glutamate release capacity have not been conducted in the CA3, or for that matter, in any CA field. Diminished release capacity of nerve terminals targeting the CA3 region is an important finding because it suggests that glutamate is modulation differently in this subregion. The most straight-forward explanation for this result could be that less glutamate is released from nerve terminals projecting to the CA3 field. This suggests that less glutamate is available for post-synaptic receptor activation and downstream cell signaling, either due to leading to decreased innervation of post-synaptic targets throughout the hippocampus. Prior work on presynaptic glutamate content in hippocampal subregions does not support this line of reasoning though actual vesicular release probability has not been directly investigated.

Increased activity or numbers of neuronal and glial glutamate transporters can be argued to affect the amount of glutamate that escapes the extrasynaptic cleft and reaches the recording sites of our MEA. Indeed, EAAC1 is selectively enriched in the CA3 subregion (Rothstein et al., 1994). However, the present study showed that rate of glutamate uptake is not significantly different between subregions and does not support this explanation. Instead, we suggest that the anatomy of CA3 synapses may provide insight about the observed results of this study. Mossy fiber terminals synapsing onto the thorny excrescences of CA3 pyramidal neurons are the most unique axonal fibers in the brain because they are large in size and are known to enclose their post-synaptic targets (Danbolt, 2001). In addition, it has been proposed that glutamate molecules release from mossy fiber terminals must travel a greater distance to escape the synaptic cleft (Andersen et al., 2007). The total amount of extracellular space has also been shown to decrease with aging in the CA3 (Segovia et al., 2001). Since glutamate transporters are extensively distributed on synaptic and extrsynaptic membranes, it is conceivable that the probability for glutamate molecules to spill-over into the extracellular space is lower in the CA3 subregion. A role for presynaptic modulation of glutamate release by mGluRs, KARs and GABAR autoreceptors has also been proposed for CA3 terminals (Moulder and Mennerick, 2006).

Finally, the attenuation of glutamate release following high K^+ stimulation may represent homeostatic control of glutamate signaling through decreased cellular intake of calcium (Martinez-Serrano et al., 1996; Piedras- Renteria et al., 2004) or by direct modulation of exocytotic machinery (Kew et al., 2000). In these context, KCl volume-dependent increase in the CA1 field is particularly interesting because it is indicates the glutamate neurotransmission is modulated differently in this subregion. As mentioned previously, each hippocampal subregion receives excitatory inputs from multiple serial and parallel pathways. The present study did not discriminate between sources of terminal glutamate. Therfore, future studies involving selective lesioning of presynaptic inputs or pharmacological inactivation of pre-terminal axons may be useful for identifying the contribution of individual pathways to subregional glutamate neurotransmission.

3.4.3 Stimulus-evoked Glutamate Release is Faster in the DG Subregion

Stimulation with high concentration KCl solution caused faster release of glutamate in the DG compared to other hippocampal subregions. To our knowledge, altered release kinetics have not been investigated for hippocampal glutamatergic terminals. Exocytotic release has been investigated in cerebellar granule cells (Holopainen and Kontro, 1987) and hippocampal gabaergic neurons (Edwards et al., 1990). A number of investigations have also been conducted through computational modeling (Vautrin et al., 2003). Collectively, these studies suggest that autoreceptors (both neurotransmitter and peptide activated) can cause changes in proteins and mRNA participating in the exocytotic machinery through a Calcium-mediate process. Specifically, an increase in neurotransmitter release may be the result of incomplete vesicular fusion with the terminal cell membrane (Sudhof et al., 2003). A similar process may be taking place in DG terminals because we observed that faster release was accompanied by an overall decrease in glutamate signal amplitude. High levels of extracellular K^+ have also been shown to cause reversal of glial glutamate transporters (Szerb, 1990). Additional investigations using pharmacological agents are needed to determine the source and mechanism of faster glutamate signals.

3.4.4 Rate of Glutamate Uptake is not Significantly Different in the Trisynaptic Circuit of Anesthetized rats

Finally, the W4 MEA was able to measure the temporal properties subsecond changes in extracellular glutamate concentration. Using this capability, we showed that glutamate uptake was rapid but not significantly different in the hippocampal trisynaptic circuit of anesthetized F344 rats. These data emphasize the importance of tight glutamate regulation in maintaining targeted activation of synaptic targets. Since loss of glutamate regulation can be caused either by uncontrolled release or compromised uptake, selective blockade of transporters using pharmacological agents offer the potential to understand compensatory regulatory mechanisms in discrete hippocampal subregions.

3.5 Results (II): Glutamate Recordings in the Unanesthetized Rat Hippocampus

3.5.1 Verification of Glutamate Signals in the CA1 Subregion of the Unanesthetized Rat Hippocampus

Our modified W4-MEA was coupled with the FAST16mkII instrument for subsecond amperometric recordings of extracellular glutamate in the F344 rat hippocampus on days 4, 5 and 6 following surgical implantation. On each day, local application of 1 mM glutamate solution (2.5 – 5 µl, pH = 7.4, prepared in 0.9% saline) through the internal cannula was used to confirm MEA recording capability for glutamate. As shown in Figure 3.9, our dual recording strategy allowed for visualization of current from enzymatic breakdown of exogenous glutamate on the glutamate oxidase-coated sites. Also, local application of saline solution as a control did not produce changes in baseline glutamate concentration.

3.5.2 Resting Levels of Extracellular Glutamate in the CA1 Subregion of the Unanesthetized Rat Hippocampus

Following a recovery period of 3 days, resting levels of extracellular glutamate were measured on days 4, 5 and 6 from the CA1 field of unanesthetized F344 rats. These measurements were conducted to evaluate the recording performance of chronic MEAs in the hippocampus. Figure 3.10 shows that resting glutamate was not statistically different in the CA1 on day 4: 13.8 µm ± 1.7, day 5: 16.6 µm ± 1.9, and day 6: 17.9 µm ±1.6; F(2, 7) = 1.215; n = 3.

3.6 Summary of Glutamate Studies in the Unanesthetized Rat Hippocampus

We showed that the chronic W4-MEA is capable of reliably measuring glutamate at subsecond rates (2Hz) in the CA1 subregion of the unanesthetized rat hippocampus. Resting levels of extracellular glutamate were measured on days 4, 5 and 6 and were not significantly different over days. Studies using additional animals along with glutamate recordings from the CA3 and DG hippocampal subregions are needed to compare resting glutamate levels measured by our MEA technology with existing microdialysis data. However, the present results are consistent with our previous published studies using S2-MEAs in the PFC and striatum of Long Evans rats (Rutherford et al., 2007) and C57BL6 mice (Hascup et al., 2007). Our ability to measure exogenous glutamate from day 4 to day 6 and the consistent resting levels seen on all three days suggest that the enzyme coating on the Pt sites is functional for at least 6 days in the rat hippocampus. W4-MEA viability was not evaluated beyond 6 days in the present study. However, we have previously shown that our chronic S2-MEAs are responsive to exogenous hydrogen peroxide applications for up to 90 days (Rutherford et al., 2007). Additional investigations are needed to evaluate the properties of the enzyme layer and the overall recording longevity of our MEAs. However, the present studies indicate that our W4-MEAs are capable of measuring hippocampal glutamate over multiple days and can be combined with behavioral experiments for future investigations in unanesthetized rats.

Copyright © Pooja Mahendra Talauliker 2010

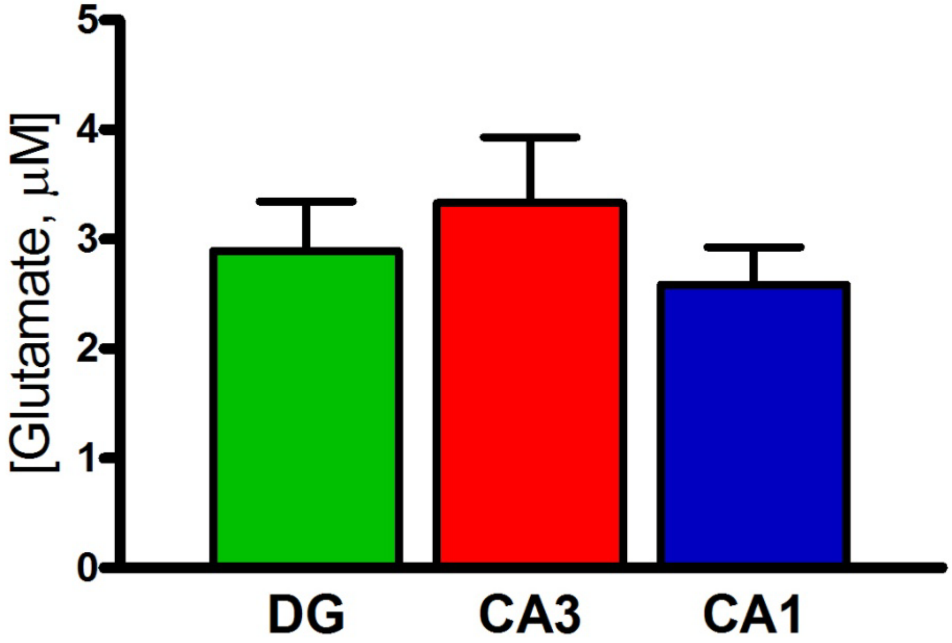

Figure 3.1: Average extracellular levels of resting glutamate in subregions of the hippocampal trisynaptic circuit. Extracellular levels of resting glutamate were not significantly different in the DG: 2.9 μM ± 0.4, n=15, CA3: 3.3 μM ± 0.6, n=15 and CA1: 2.6 μM ± 0.3, n=16; F (2, 43) = 0.33, p = 0.7.

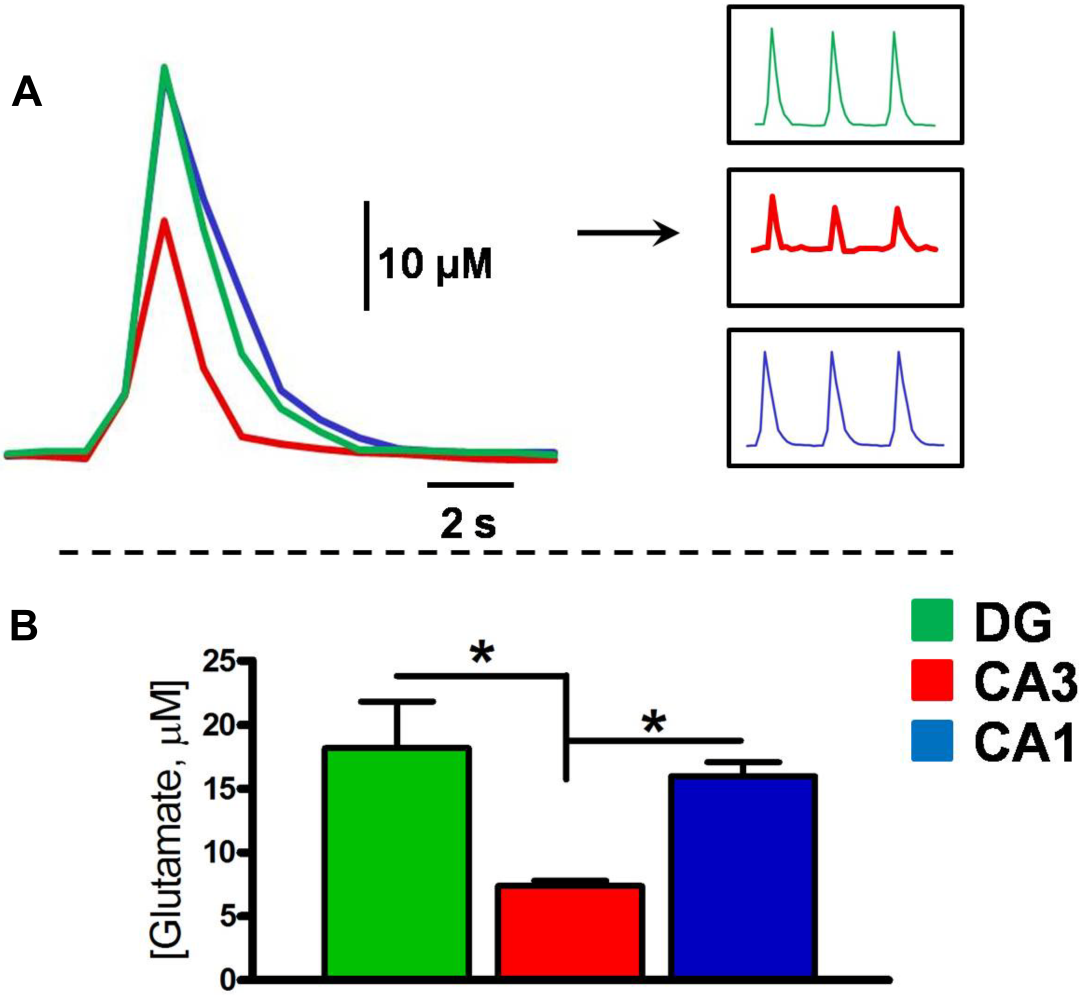

Figure 3.2: Comparison of glutamate release capacity in subregions of the rat hippocampus following stimulation with 70 mM KCl. Panels A and Bshows that application of KCl solution (70 mM, isotonic, pH 7.4, 12.5 - 50 nL) revealed differences in glutamate release in hippocampal subregions. Average maximum signal amplitudes are shown: {DG: 17.5 μM ± 3.9; CA3: 7.4 μM ± 0.4; CA1: 16.0 μM ± 1.13 μM; n = 7; F(2, 18) = 6.6, $p = 0.0071$}. The variances of these data were significantly different with Bartlett's test $p < 0.0001$. These data show that glutamate release was significantly diminished in the CA3 subregion compared to the CA1 and DG (*: $p < 0.05$).

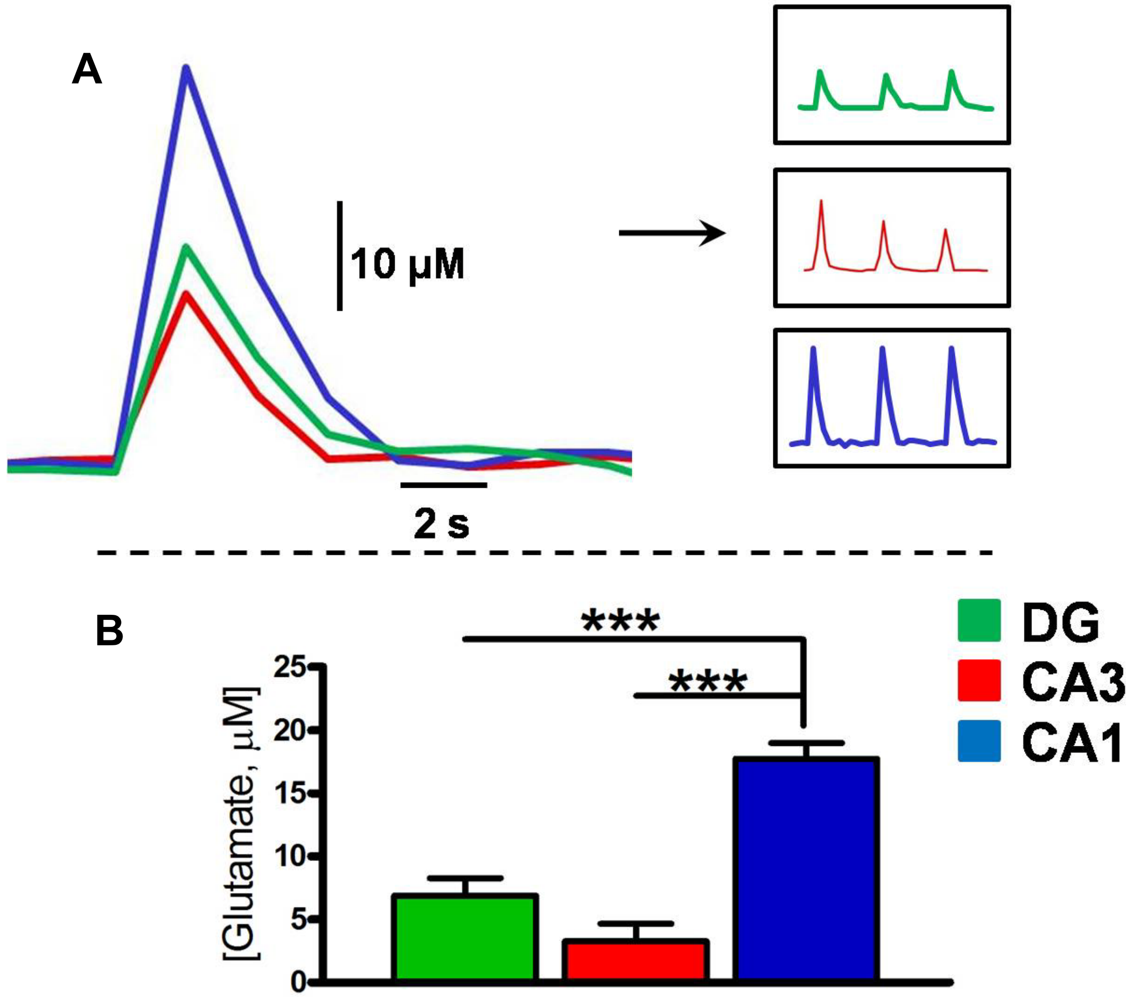

Figure 3.3: Comparison of glutamate release capacity in subregions of the rat hippocampus following stimulation with 120 mM KCl. Panels A and B show that application of 120 mM KCl solution revealed additional differences in subregional glutamate release capabilities. Specifically, glutamate release was significantly diminished in the DG and CA3. {DG: 6.9 µM ± 1.4; CA3: 3.3 µM ± 1.4; CA1: 17.7 µM ± 1.2; n=6; F (2, 11) = 29.8}. Significance was defined as ***: $p < 0.001$

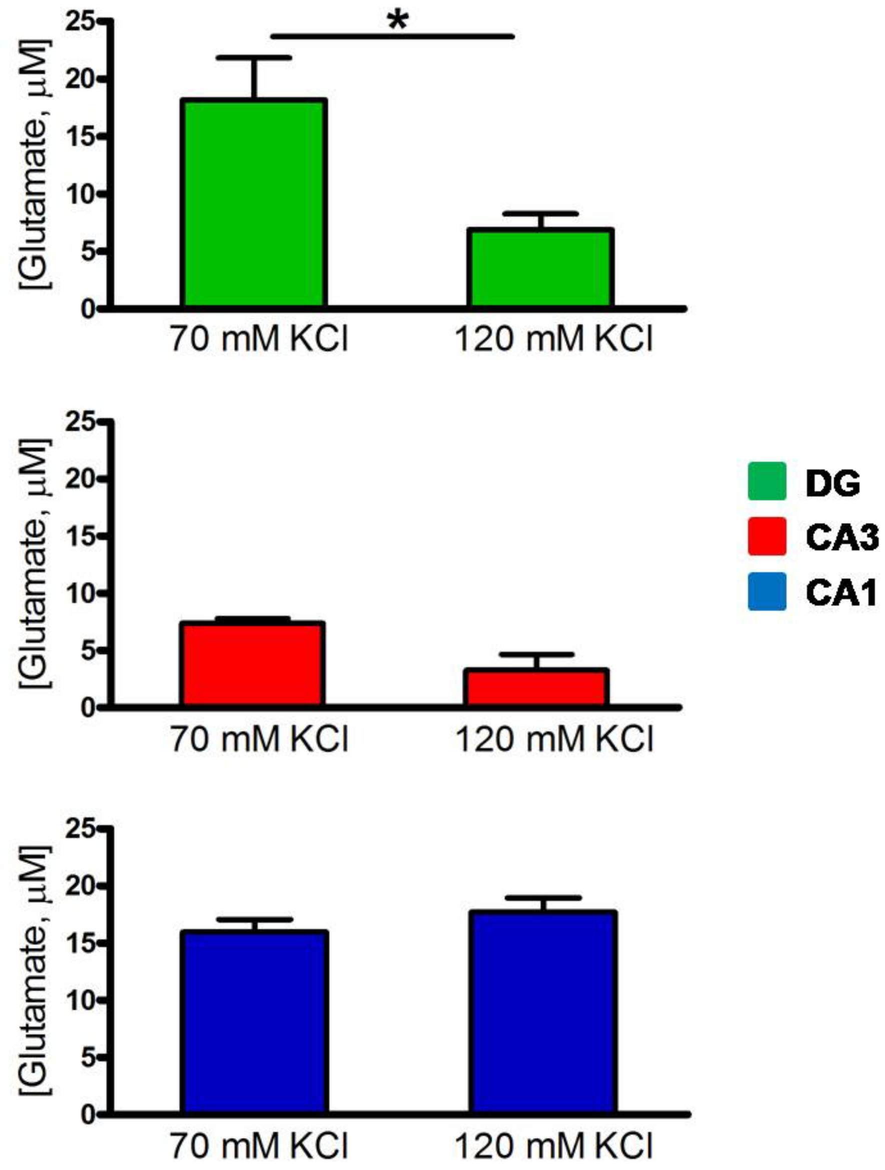

Figure 3.4: KCl concentration-dependent alteration in subregional glutamate release capacity. Between treatment groups, the DG region showed pronounced loss in signal amplitude {t(7) = 2.89, p = 0.023, F-test p=0.44 while the CA3, showed a moderate decline {t(2)=2.824, p=0.11}.

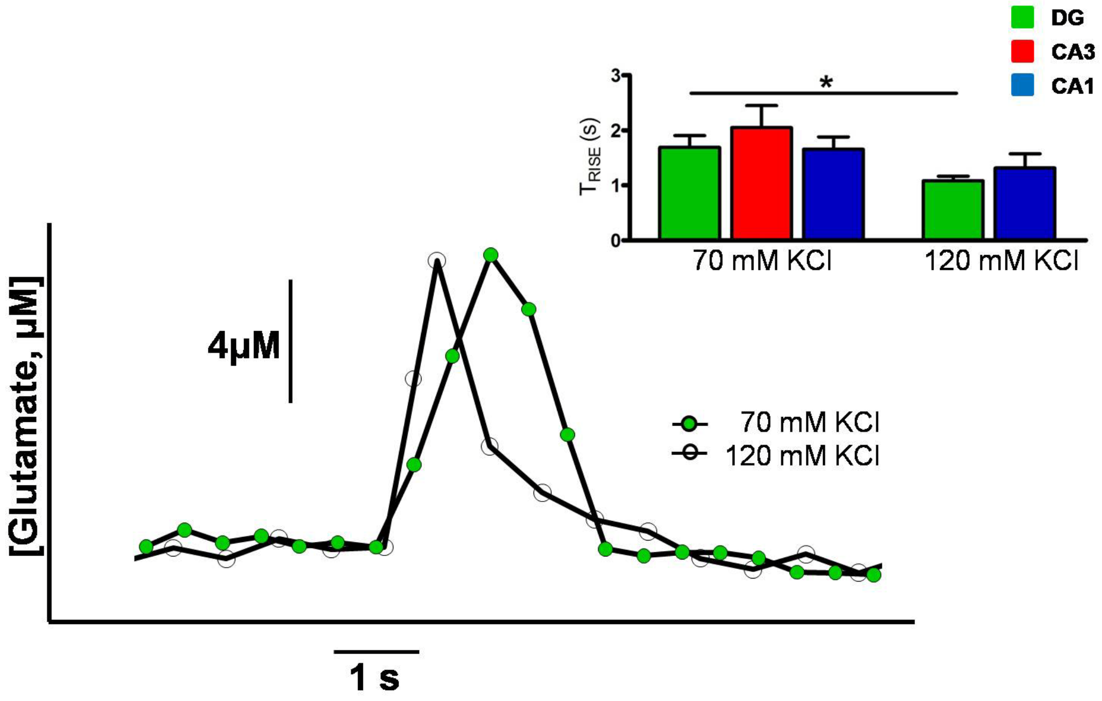

Figure 3.5: Rise times to maximum signal amplitude following local application of 70 or 120 mM KCl in the DG subregion. Comparison of rise times in each region showed significantly faster glutamate release in the DG with 120 mM KCl application {t(6) = 2.63, p = 0.04}.

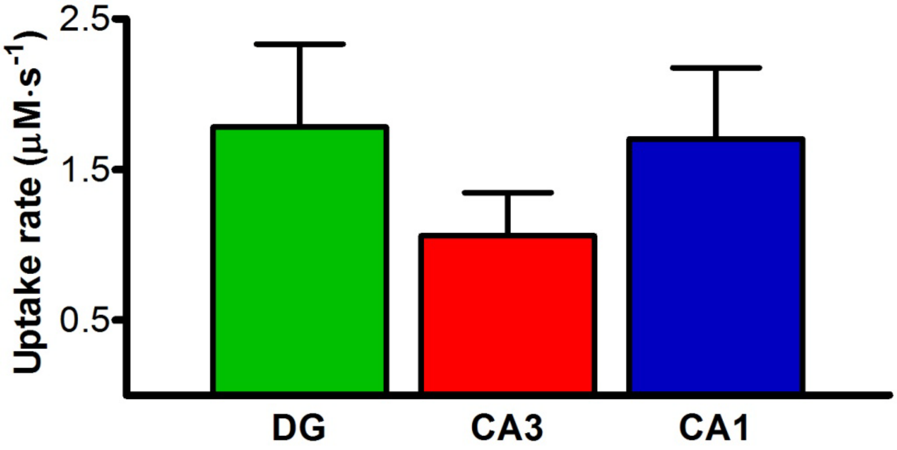

Figure 3.6: Average rates of glutamate uptake in the hippocampal trisynaptic pathway. Local application of 100 µM glutamate solution showed that clearance of glutamate was not significantly different {F(2,17)=0.68, p=0.52} in the DG (1.78µM ± 0.55µM), CA3 (1.06µM ± 0.28µM) and CA1 (1.70µM ± 0.47µM) regions of the anesthetized rat hippocampus.

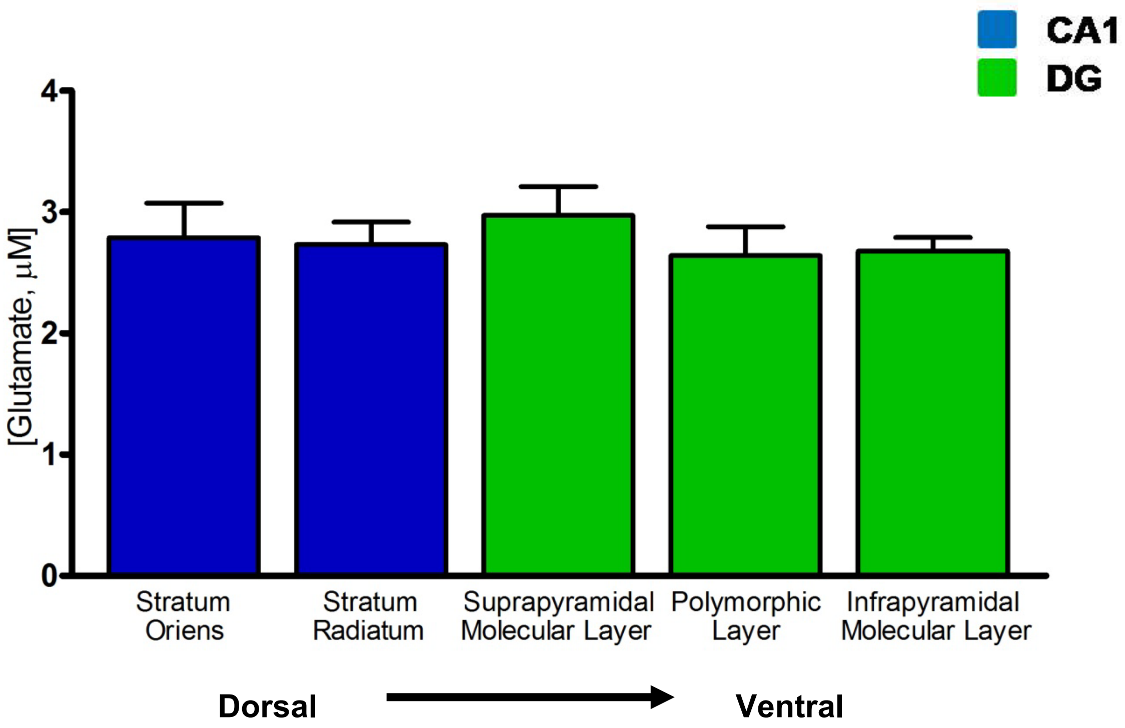

Figure 3.7: Depth profile of resting glutamate in the anesthetized rat hippocampus. Resting levels of extracellular glutamate were obtained at 5 depths, each separated by 0.35 mm. As measured from the surface of the brain, the depths corresponded to the stratum oriens and stratum radiatum of the CA1 and the suprapyramidal molecular layer, polymorphic layer and infrapyramidal molecular layer of the DG. Average resting glutamate was not significantly different between regions {F(4,17) = 0.3, p = 0.8, n = 3}.

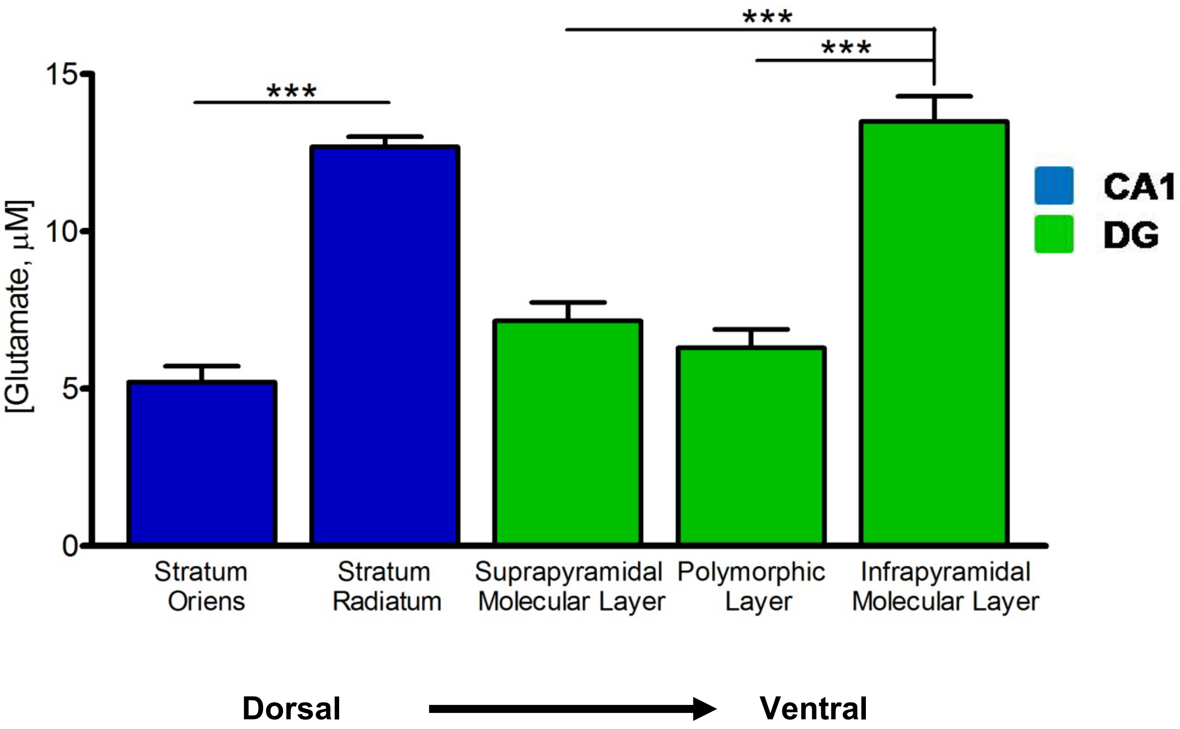

Figure 3.8: Depth profile of KCl-evoked glutamate in the anesthetized rat hippocampus. Hippocampal glutamate release capacity following stimulation with KCl solution was investigated at 5 different depths, each separated by 0.35 mm. Average glutamate signal amplitude was significantly larger in the stratum radiatum (12.7 µM ± 0.3) than the stratum oriens (5.2 µM ± 0.5, $p<0.0001$)of the CA1 field. Similarly, the infrapyramidal molecular layer of the DG had the largest signals (13.5 µM ± 0.8) compared to the suprapyramidal molecular layer (7.2 µM ± 0.6) and the polymorphic cell layer (6.3 µM ± 0.6), {F(4,17)=45.55; n = 3 per group}.

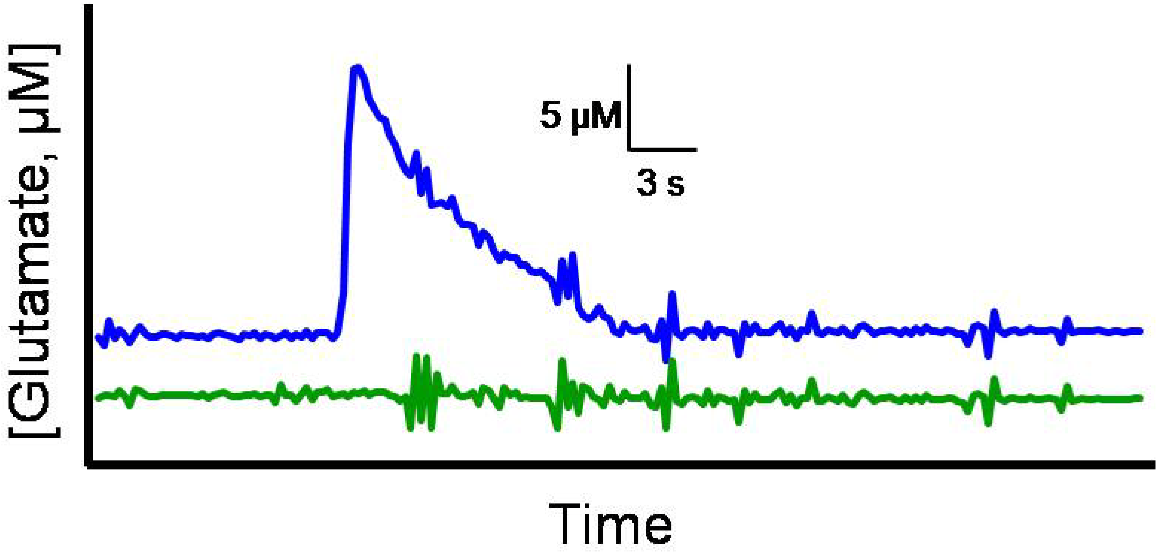

Figure 3.9 Validation of glutamate signals in the CA1 subregion of the unanesthetized rat hippocampus. Local applications of 1 mM glutamate solution (2.5 – 5 µl, pH = 7.4, prepared in 0.9% saline) were used to confirm MEA recording capability for glutamate. Our dual recording strategy allowed for visualization of current from enzymatic breakdown of exogenous glutamate on the glutamate oxidase-coated sites (blue).

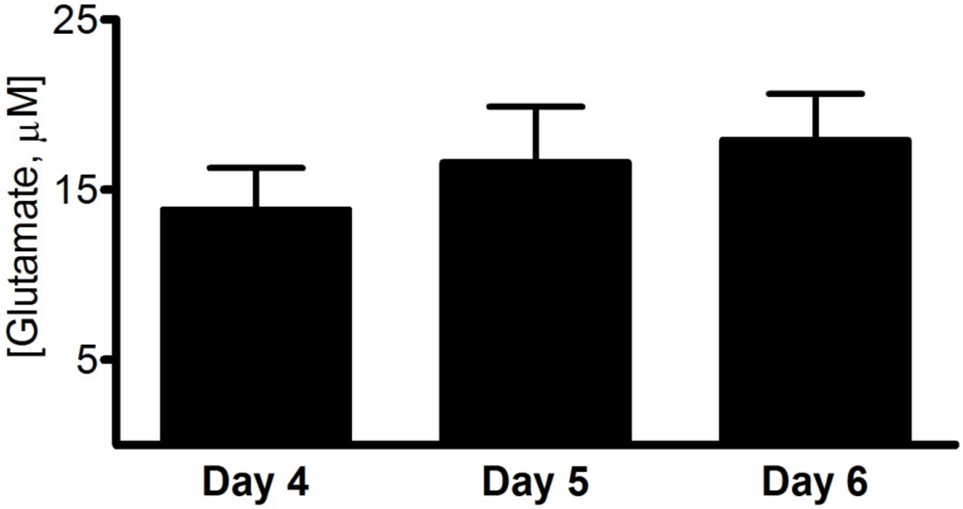

Figure 3.10: Resting glutamate measurements over three days in the CA1 subregion of unanesthetized rats. Following a recovery period of 3 days, resting levels of extracellular glutamate were measured on days 4, 5 and 6 in the CA1 field of F344 rats. Resting glutamate was not statistically different in the CA1 up to 6 days post-surgery. Day 4: 13.8 µm ± 1.7, Day 5: 16.6 µm ± 1.9, Day 6: 17.9 µm ±1.6; F(2, 7) = 1.215; n = 3.

Chapter Four: Surface Characterization and Topographical Analysis of MEAs

4.1 Introduction

Detailed surface characterization is a necessary first step towards improving the performance of MEAs intended for *in vivo* electrochemical recordings. Under acute experimental conditions, high quality signal generation is dependent upon electrode sensitivity and selectivity for the analyte of interest (Reiner et al., 2006), total electroactive area and reaction kinetics (Ozden et al., 1998). To improve these recording parameters, knowledge about intrinsic physical and electrochemical properties of the recording surface such as topography, electrical behavior, chemical reactivity and molecular composition is necessary.

In chapter three, we used novel ceramic-based MEAs with oxidase enzyme-coated recording sites to measure resting levels of extracellular glutamate in the hippocampus of unanesthetized rats. Glutamate measurements could be obtained up to 6 days post-surgery, but high levels of background noise restricted extended neurotransmitter measurements, indicating a change either in the extracellular environment or the enzyme layer, perhaps both. Until now, the microscale topography of the MEA, which is predominantly composed of ceramic alumina (Al_2O_3), has never been studied. Traditionally, ceramic has been the material of choice for orthopedic prostheses and dental implants because of its structural strength and negligible tissue reactivity (Hulbert, 1972; Williams et al., 1989). In these devices, improved rates of implant success have been achieved primarily by altering the roughness of the ceramic surface. For example, replacement hip joint prostheses show enhanced integration with host tissue when the roughness value of the implant surface is equivalent to the dimensions of bone-forming cells (50 - 400 µm). Increased roughness is also useful for improving the anchorage of dental implants but can compromise oral health by promoting bacterial growth and plaque formation (Boyan 1996, Shackelford

1999). Analogous studies on central nervous system biocompatibility are lacking because the utilization of ceramic-based neural devices as a tool for chronic investigations is a very recent development (Rutherford et al., 2007; Hascup et al., 2008). We have begun to examine the tissue effects of our MEAs in implanted rats (Rutherford et al., 2007, Hascup et al., 2009); however, the surface topography of the MEAprior to implantation also needs to be studied.

Platinum is widely used in amperometric electrodes, both planar and wire-based, because of its lasting biocompatibility and high catalytic activity for amperometric measurements of hydrogen peroxide. In a majority of electrochemical experiments utilizing platinum-based electrodes, hydrogen peroxide is generated as a reporter molecule following the enzymatic oxidation of the molecule of interest. It is generally held that the reaction mechanism of hydrogen peroxide oxidation on platinum surfaces is independent of electrode geometry (Hall et al., 1998; 1999). However, a review of current scientific literature reveals that this similarity does not translate to equivalent recording performance per unit area (Table 4.1). Dissimilarities in analyte sensitivity and recording lifespan observed both within and between electrode types can be hypothesized to have been caused by differences in material selection and fabrication processes but, to our knowledge, are yet to be directly investigated.

In the present chapter, we studied the surface characteristics of our microelectrodes using complementary investigative techniques. *In vitro* calibration was conducted to compare the performance of S2 and W4 MEAs. Scanning electron microscopy (SEM) was utilized to obtain high resolution secondary electron micrographs of MEA samples, allowing examination of sub-micron sized topographical features. Further, backscattered electron microscopy (BSE) and energy dispersive spectroscopy (EDS) were used to visualize surface composition, and to detect potential contaminants on the recording sites. The qualitative information gained from these experiments was supplemented by topographical analysis and roughness estimation using atomic force microscopy (AFM). As a whole, these studies are the first to describe the surface properties of an implantable ceramic-based neural device. The present results will also be useful to ongoing efforts aimed at improving and extending the recording performance of our MEAs.

4.2 Materials and Methods

Please refer to Chapter Two for a detailed description of MEA fabrication, surface cleaning methods, sample preparation and imaging procedures for scanning electron microscopy and atomic force microscopy.

4.3 Results and Discussion

4.3.1 *In Vitro* Performance of W4 and S2 MEAs

We compared the *in vitro* performance of W4 and S2 MEAs through beaker calibrations. As shown in Figure 4.1 A, the average sensitivity (slope) of W4 MEAs (-5.7×10^{-3} nA·µM^{-1} ± 6.8×10^{-4}, n = 14) was not significantly different from S2 MEAs (-7.5×10^{-3} nA·µM^{-1} ± 1.3×10^{-4}, n = 10). However, the average limit of detection (LOD) was significantly higher for W4 MEAs (0.61 µM ± 0.08, n = 14) when compared to S2 MEAs (0.24 µM ± 0.04, n = 10). **: ($p < 0.0.1$) (Figure 4.1 B). The higher LOD is likely due to the lower surface area of Pt sites on W4 MEAs. A smaller site leads to less signal being obtained per unit surface area. Since the RMS noise on the signal is unchanged between MEA designs, the signal to noise ratio is lower for the W4 MEA and by definition results in a higher LOD. At the same time, we note that the average LOD values for W4 MEAs are well within ≤ 1 µM. Taking this result together with the comparable sensitivities of both designs, we conclude that the W4 MEA meets our performance criteria for *in vivo* experimentation.

4.3.2 Photolithography Produces Recording Sites with Microwell Geometry

Images A and B (Figure 4.2) are secondary electron micrographs of the tip of a W4 MEA. In this type of imaging, the signal source is provided by low energy electrons that are released when the incident electron beam impacts the sample surface. For these experiments, the MEA was rotated in the X-Y plane and tilted with respect to the incident beam such that the images were maintained in focus while maximizing the yield of textural information. The front face of the MEA is comprised of an array of platinum sites and their connecting lines overlying a machined ceramic base. Except for the working sites, the entire surface is enclosed underneath a continuous layer of insulating polyimide (Figure 4.2 B, rotation angle: 50°; tilt angle: -10°). Interestingly, the bare recording sites are marked with irregular peaks and indentations, with approximate cross-sectional areas in the range 0.04 – 25.06 μm^2 (Figure 4.2, C and D, tilt angle = 0°). Average layer thickness ranged between 0.1 - 0.3 μm for the recording sites and 1.0 - 2.5 μm for the polyimide film, measured manually using imaging software (Axiovision, Zeiss Inc.). These numbers are consistent with manufacturer's specifications though some image distortion is expected because of sample tilting. Thus, the photolithographic process produces recording sites with a microwell geometry.

We have previously described the application of enzyme solutions and interferent exclusion layers that readily bond to the recording surface in acute experimental settings (Hascup et al., 2006; Thomas et al., 2008). Current scientific research on protein attachment (or adsorption) to microwell structures is largely focused on high throughput immunoassays and cell culture applications. Comparison studies between micron-sized plates and wells demonstrated superior protein immobilization in the latter design (Kang et al., 2005; Jung et al., 2008). For chronic measurements (weeks to months), stable coating adhesion is particularly important because the failure of the MEA implant is often associated with decreased sensitivity and selectivity for the molecules of interest. While it is plausible that the three dimensional geometry of the working sites aids in enzyme immobilization and contributes to extended neurochemical detection capability, the evaluation of electrode sensitivity (in comparison to planar electrodes that have inlaid or protruding geometry) is not straightforward. Additional parameters such as the depth of the microwell, distance between electrodes on a multisite array and software limitations must also be considered (Sandison et al., 2002). Further investigation is needed to evaluate the long term adhesion properties of coating solutions.

4.3.3 Ceramic Topography is composed of Micro/nanoscale Surface Features

The reverse (opposite) face of the MEA is also machined but is free of surface coatings. Here, the topography is dominated by intersecting microgrooves (width < 1 µm) and irregular holes (cross-sectional area 0.1 – 10.0 μm^2), both of which are believed to produced during the ceramic polishing process (Figure 4.3, A and B). A detailed discussion on wear-related microgroove and pit formation is beyond the scope of this chapter (see Zarudi and Zhang, 1998; Ravikiran, 1999, 2000, 2000b for review). The topography of the arrays is analyzed further in following sections. In contrast, the sides of the microelectrode are composed of an extensive network of interconnected peaks and pores, resulting in an extremely rough appearance (Figure 4.3 C). The boundary region of a given peak was not readily distinguishable from adjacent peaks or pores. Indeed, a base surface was not at all discernible; therefore identification and cross-sectional measurements of individual surface features could not be conducted. Larger surface cavities were composed of clusters of smaller microfeatures and connected to other cavities or holes through fissures and surface corrugations (red contouring shown in Figure 4.3 D, 0° tilt). Also, note the increased brightness along the border of some structures in the image. This edge effect is caused by sharp changes in the height/depth of sample resulting in increased electron scattering in this region.

4.3.4 Fabrication Errors and Defects from Photolithographic Processing

The occurrence of surface defects on approximately 5% of the microelectrodes used in this study was an unexpected finding. The selected examples shown in Figure 4.4 (A-D) suggest that these imperfections are the result of fabrication errors during photolithography. For example, the active surface area of a recording site is reduced when an offset in the photomask displaces the boundaries of the polyimide layer (Figure 4.4 D). Similarly, a disrupted polyimide coating may not provide an adequate shield for connecting lines in an aqueous environment (Figure 4.4 C). We also observed defects in the platinum circuitry. Electron micrographs A and B in Figure 4.4 illustrate delamination of the platinum/titanium composite from the recording sites and connecting lines. Though further investigations on defective MEAs were not conducted, these findings emphasize the importance of quality testing procedures. In particular, periodic surface examination of random microelectrode samples may be useful for identifying a range of manufacturing errors that compromise recording performance but may not be apparent to the naked eye.

4.3.5 Backscattered Electron Imaging (BSE) and Energy Dispersive Spectroscopy (EDS)

Electron micrographs obtained by BSE detection clearly distinguished between the ceramic substrate and the polyimide layer on the front surface of the microelectrode (Figure 4.5 A). In these images, the intensity of the polyimide was uniform, indicative of homogenous surface composition. Also, maximum image intensity was produced by the platinum working sites, consistent with the working principle of BSE imaging. Note that the resolution of BSE images is lower than SE images (Figure 4.5 B) because backscattered electrons interact with a larger volume of the sample leading to a loss in spatial resolution.

Because information about the elemental identity of a recording surface can be useful for detecting potential contaminants and for evaluating electrochemical behavior, we carried out EDS studies to analyze the elemental composition of the recording sites (Figure 4.6). Spectral analysis confirmed that the recording sites are primarily composed of platinum. The multiple platinum peaks on the graph are associated with excitation energy levels of different electron orbitals. Apart from platinum, x-ray emissions corresponding to carbon and silver were also detected and may have been transferred during the photolithographic process. Carbon is known to impede amperometric detection of hydrogen peroxide, therefore thorough cleaning of the recording surface is a critical step in experimental preparation. If carbon is embedded into the recording layers, it indicates a problem with the fabrication process. Accordingly, quantification of total contaminant must be performed to determine whether it is within the tolerance range of the device.

It is important to note that BSE and EDS techniques do not provide direct information about the oxidation state of any element, though oxygen atoms can be detected by the Silicon/Lithium Detector used in these studies. In this context, the absence of oxygen in the atomic spectrum is a fascinating finding because platinum naturally adsorbs oxygen molecules into its crystalline lattice. These results also suggest that platinum may be present in its elemental state. The leading hypothesis on platinum-based amperometric detection contends that the reduction of hydrogen peroxide by platinum electrodes is actually the result of a catalytic reaction with a thin layer of platinum oxide (Lingane and Anson, 1960). Indeed, it is believed that the current detected at the electrode surface corresponds to the re-oxidation of platinum to platinum oxide following hydrogen peroxide reduction. Clearly, additional investigations are needed to determine whether amperometric detection of hydrogen peroxide by our microelectrodes is governed by a previously undetected electrochemical step or perhaps, involves a different reaction altogether.

4.3.6 Platinum Sites are composed of Nanoscale Topographical Features

In a scanning electron micrograph, the scattering intensities of secondary or backscattered electrons displaced from the sample surface are represented in gray scale. Despite the large depth of field, the image does not contain information about surface height. To address this limitation, atomic force microscopy was utilized to characterize the three dimensional topography of our MEAs. Figures 4.7 A and B depict the typical micro and nanoscale topography data of a recording site over 15×15 μm and 1×1 μm regions, respectively. The spatial resolution of these diagrams is identical because the same AFM probe was used to acquire topographical information. However, adjusting the sampling area is useful for visualizing surface details at different magnification levels and for isolating regions of interest. Variations in surface height are shown in the form of a color gradient where lighter shading is indicative of regions with raised topography while darker areas correspond to indentations or cavities. For the present study, sample regions on the recording sites were selected randomly: 15×15 μm (N_{SITES} = 3, $N_{SAMPLES}$ per site = 3, Height scale = 0 - 150 nm) and 1×1 μm (N_{SITES} = 3, $N_{SAMPLES}$ per site = 3, Height scale = 0 - 20 nm). These data supported the SEM study and verified non-uniform morphology of the platinum sites. The actual shape and distribution of peaks and holes was visualized by constructing three dimensional digital projections of the mapped data (Figure 4.8 A, B).

AFM data from these experiments was quantified to evaluate differences in surface roughness between sites (Table 4.2). It is important to note that data points beyond the site boundary were excluded to avoid artificial skewing of results. Values for R_{AVG} (arithmetic average of absolute values of peaks and valleys within the selected area) and R_{RMS} (root mean squared roughness) obtained from 15 μm^2 samples describe a surface with nanoscale roughness. Roughness factors obtained from 1 μm^2 images show greater variability because they represent a small portion of the overall site. The R_{SKEW} (dimensionless number signifying the relative proportion of peaks and valleys) relays two important pieces of information. Positive R_{SKEW} indicates an asymmetric surface with more peaks and holes. Additionally, values >1 suggest the presence of extreme peaks and holes and is verified by the average H_{MAX} (maximum peak height) and D_{MAX} (maximum valley depth given in terms of absolute distance).

Roughness analysis has some limitations. Calculations for R_{AVG} and R_{RMS} do not include holes. Also, these values can be distorted by outlier peaks of extreme height (for example, features in the height range of H_{MAX}) and cannot tell us whether features of a certain size occur more frequently than others (mode or median value). Finally, R_{SKEW} does not account for the actual distribution of peaks and holes so the roughness value for two sites can be identical even if the peaks are grouped together on one site but are distributed evenly on the other. A typical scenario is illustrated in Figure 4.9 (20×20 μm scan area).

To address this, we examined surface height across multiple cross-sections of each site (representative image shown in Figure 4.10 A), also known as line scan analysis. Overall, line profiles for each site indicate that the topography of the sample recording sites is dominated by nanometer sized peaks and holes (absolute height < 5 nm) (Figure 4.10 B). Extreme peaks and holes (> 100 nm) were less frequent. The lateral distribution of extreme surface features was unique for each site. The total number of surface features on each site was obtained by constructing a frequency distribution (representative graph shown in Figure 4.10 C). Absolute numbers were variable between sites (data not shown); however the frequency distribution demonstrated near-Gaussian properties for every sample. In keeping with line analysis results, most data points were within an absolute height value of 10nm from the mean feature height (~2nm). Note that the distribution also indicates flat regions (height = 0).

The implication of these results must be discussed. Clearly, the nanoscale topography of the recording sites produces an electroactive area that is much greater than the geometric surface area. While this suggests improved sensitivity measurements over a flat surface, it is important to note sensitivity also depends on the probability that a surface will be reached by an electroactive molecule and undergoes a chemical reaction. Accordingly, if a molecule cannot reach a narrow cavity or a steep wall, these regions represent areas of less than average reaction probability. Thus, total surface area does not necessarily translate to total accessible area. Such surface areas may also contribute to differences in recording performance between Pt sites.

4.3.7 Machined Ceramic Faces are dominated by Nanometer–Sized Microgrooves

A similar approach was used to map the front and reverse ceramic faces of the microelectrode (Figure 4.11 A-C). The inner surfaces of the microgrooves observed on the lower ceramic surface during SEM imaging were irregular in shape but were relatively consistent in maximum depth (200 – 220 nm) for the samples selected in this study. Roughness analysis (Table 4.3) generated R_{AVG} and R_{RMS} values similar to the platinum sites. The most important finding in this study was gained from the negative R_{SKEW} and height distribution data which indicated that holes were the dominating surface feature. (R_{SKEW} = -2.2 and -0.4 respectively). Lastly, R_{AVG} and R_{RMS} values were extreme on the front surface due to height variation between the ceramic base, the polyimide coating, the connecting lines and the platinum sites. Together with the results from the previous section, it is apparent that the topography and roughness characteristics of the front and back faces of the MEA differ from each other and from the ceramic sides.

4.4 Summary and Conclusion

When observed under the optical microscope, the machined surfaces of our MEA appear smooth and light reflective. The studies conducted in this chapter described these surfaces at sub-micron levels of spatial resolution using scanning electron microscopy and atomic force microscopy. Recording sites on the patterned face of the MEA appear recessed relative to adjacent surface due to a coating of polyimide that covers the ceramic surface and connecting lines. Polyimide also served to lower overall surface roughness. The opposite face of the MEA consists of non-parallel microgrooves and focal pits that result in a surface with low nanoscale roughness but high negative asymmetry. Also, microscale and nanoscale features were observed on the sides of the microelectrode where the surface was dominated by irregular peaks and holes. Thus each face of the MEA has a unique surface profile. The absence of oxygen on the platinum surface was the most fascinating finding of this study along with the discovery of platinum nanostructures that served to increase total recording site area. Together, these results support that photolithographic fabrication produces recording sites with naturally occurring nanoscale roughness and may have a unique physical chemistry that warrants further investigation.

Copyright © Pooja Mahendra Talauliker 2010

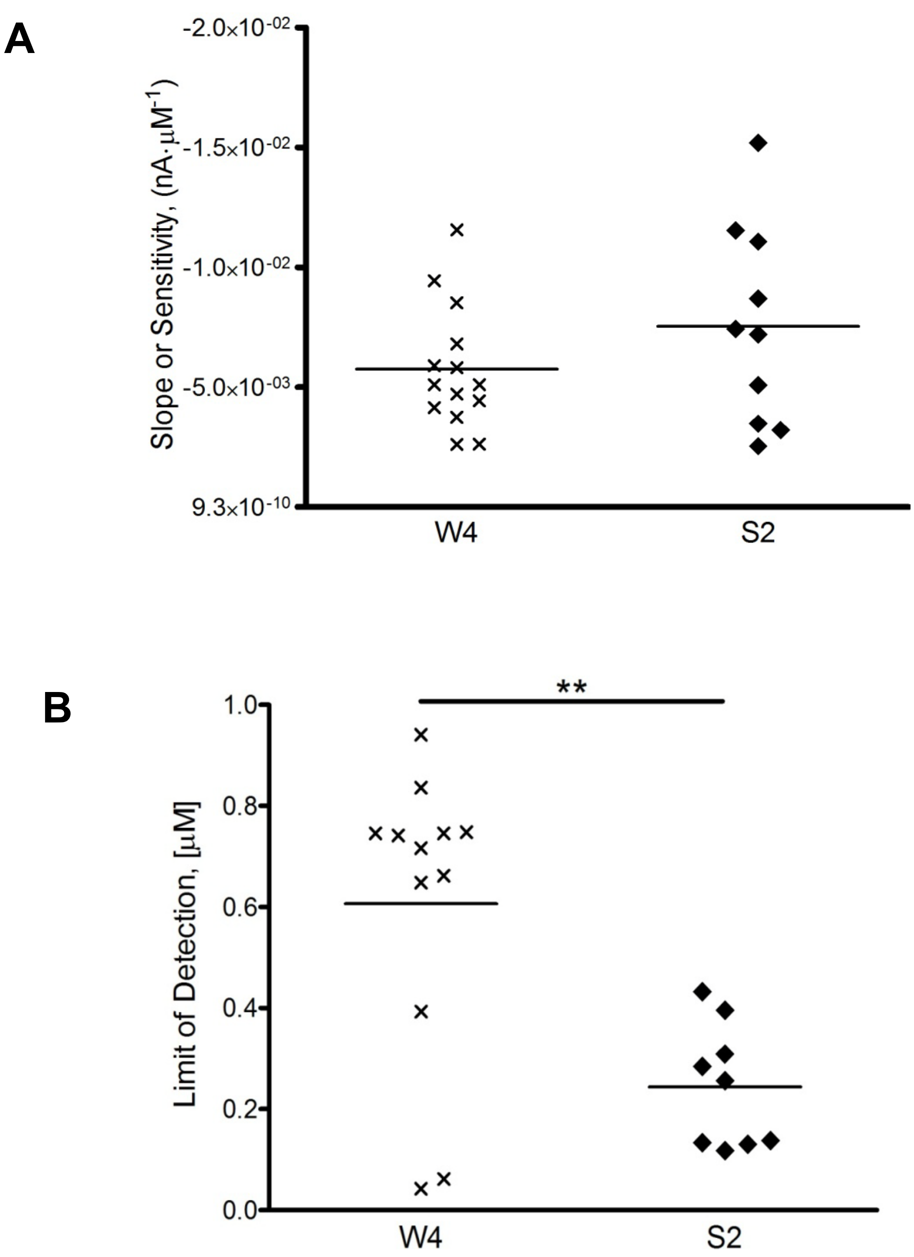

Figure 4.1: Comparison of slope and LODs of W4 and S2-MEAs. Figure A shows that the average sensitivity (slope) of W4 MEAs (-5.7 x 10^{-3} nA·µM^{-1} ± 6.8 x 10^{-4}, n = 14) and S2 MEAs (-7.5 x 10^{-3} nA·µM^{-1} ± 1.3 x 10^{-4}, n = 10) are not significantly different while Figure B shows that the limit of detection was significantly higher for W4 MEAs (0.61 µM ± 0.08, n = 14) when compared to S2 MEAs (0.24 µM ± 0.04, n = 10). **: ($p < 0.0.1$).

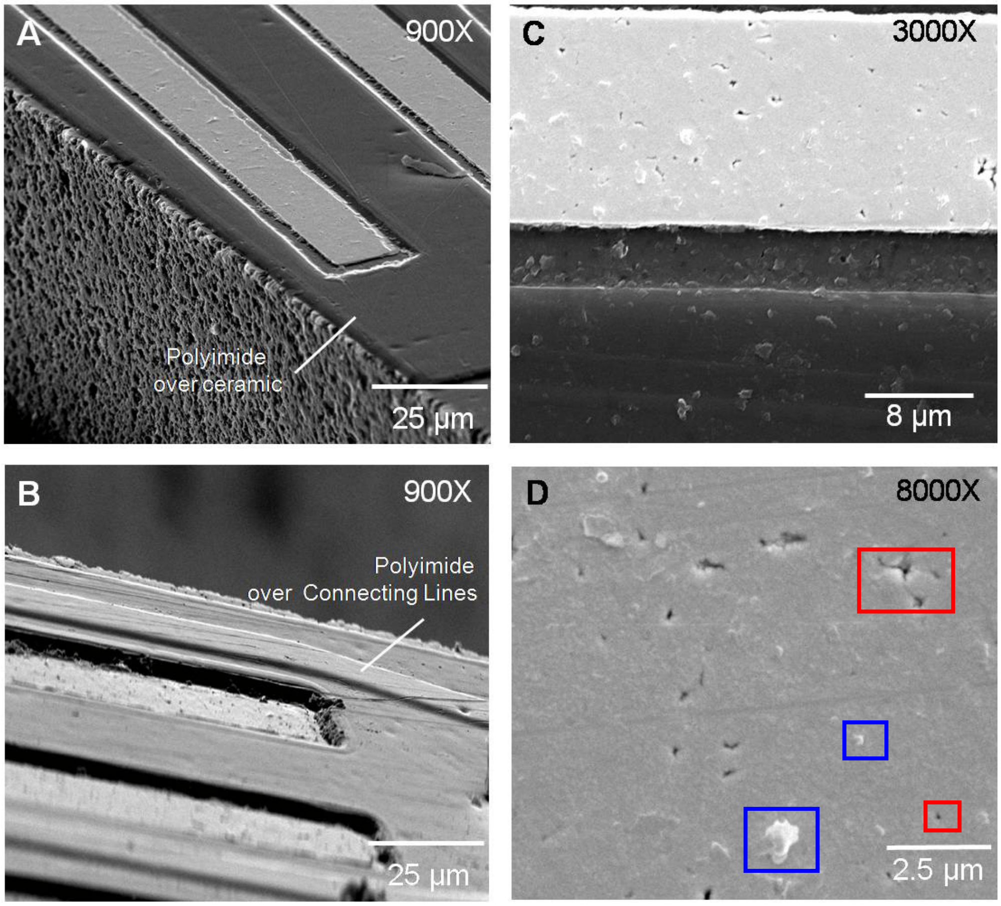
A
900X
Polyimide
over ceramic
25 µm
C
3000X
8 µm
B
900X
Polyimide
over Connecting Lines
25 µm
D
8000X
2.5 µm

Figure 4.2: Secondary electron micrographs of front surface of the MEA. A and B are electron micrographs of the front surface of the MEA Except for the working sites, the entire surface is enclosed underneath a continuous layer of insulating polyimide. Panels C and D are high magnification images of the bare Pt sites and show sub-micron sized irregularities in the form of peaks (blue boxes) and indentations (red boxes).

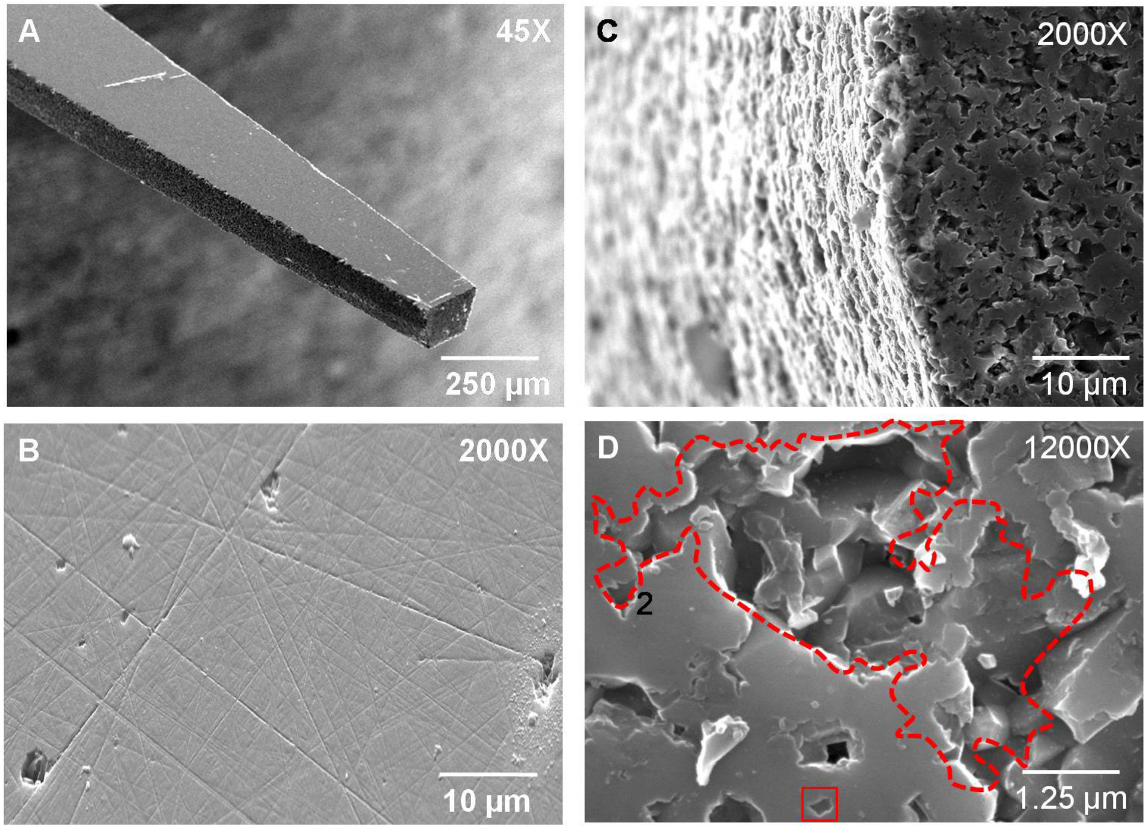

Figure 4.3: Secondary electron micrographs of the back surface and sides of the MEA. Panels A and B show that the reverse face of the MEA is comprised of intersecting microgrooves (width < 1 μm) and irregular holes (cross-sectional area 0.1 – 10.0 μm^2). In contrast, Panels C and D show that the sides of the MEA are composed of an extensive network of interconnected pores that were composed of clusters of smaller microfeatures (red contouring in D). Increased brightness along the border of some structures in panel D is caused by edge effects.

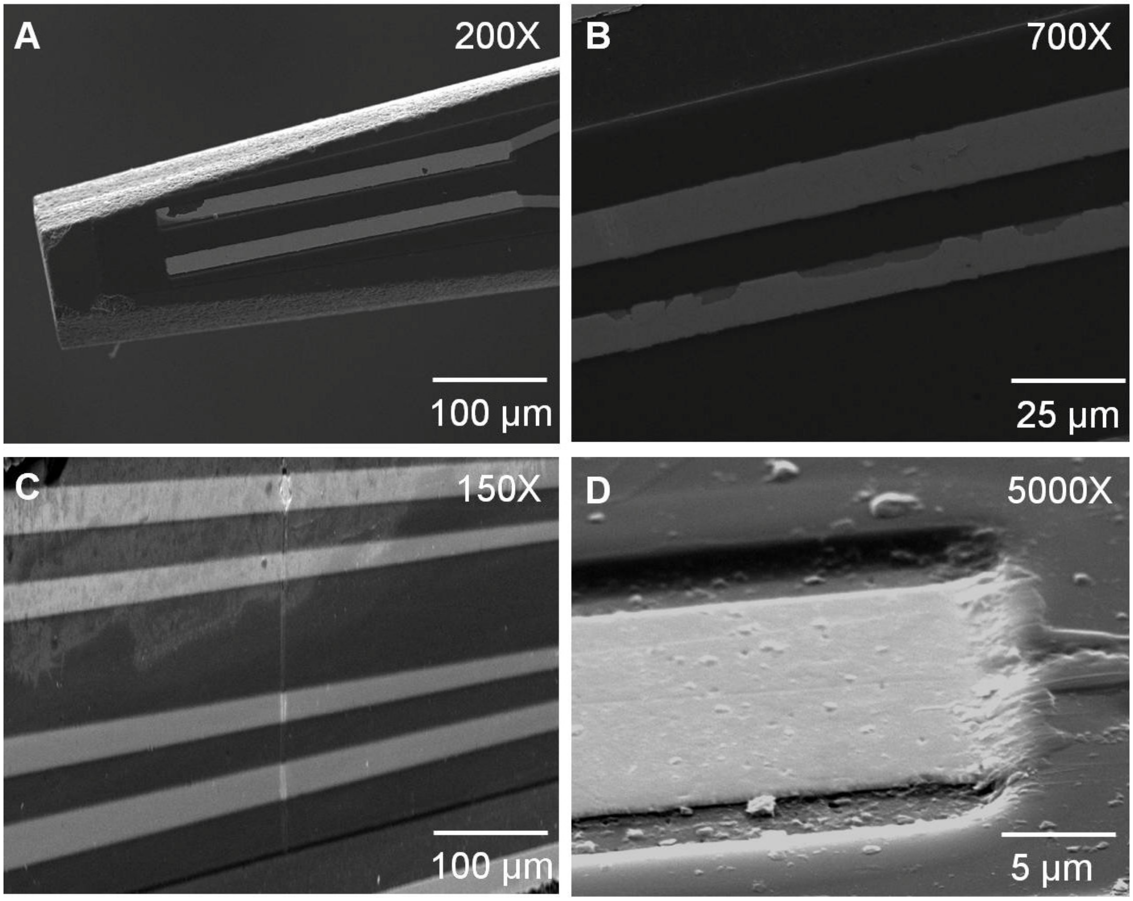
A
200X
100 µm
B
700X
25 µm
C
150X
100 µm
D
5000X
5 µm

Figure 4.4: Defects from photolithographic processing. Panels A and B show delamination of the Pt/Ti composite from the recording sites and connecting lines. Panels C and D show an offset in polyimide layer.

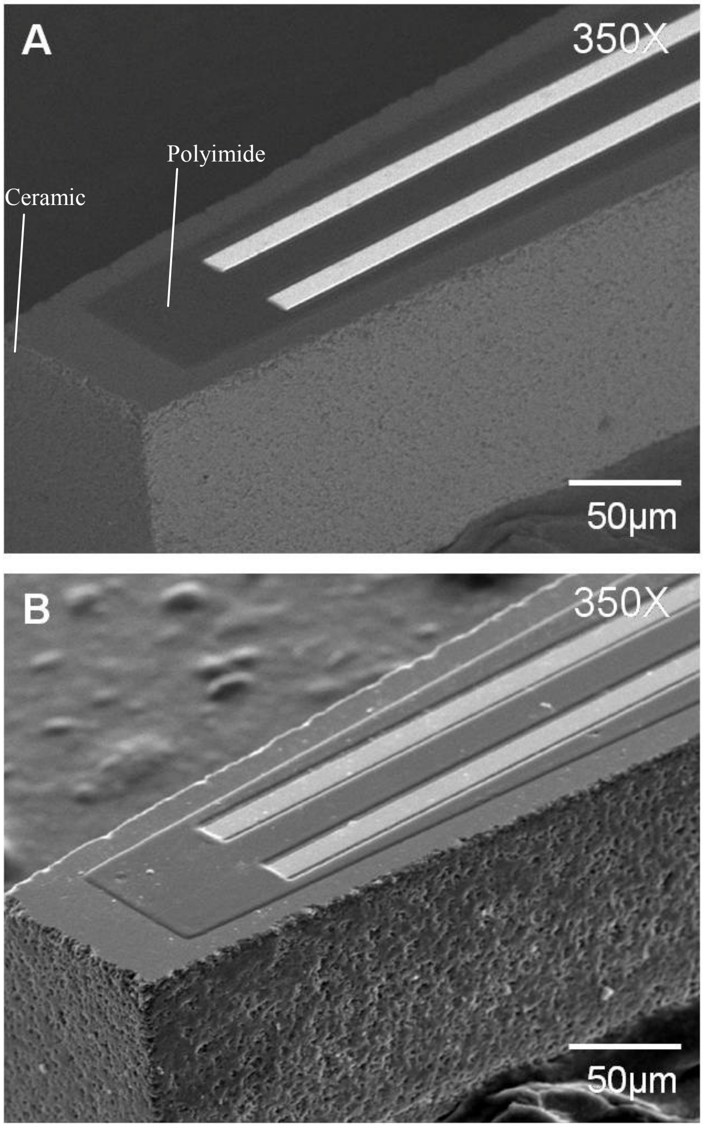

Figure 4.5: Backscattered electron micrographs of MEA surfaces. Panel A is a backscattered electron micrograph (BSE) of the front surface and sides of a W4-MEA. The polyimide coating, ceramic substrate and Pt sites are distinguishable based on their gray intensity levels. The polyimide layer appeared to be homogenous because it showed uniform intensity. Panel B is a secondary electron micrograph (SEI) of the same MEA shown for the sake of comparison. The spatial resolution of an SEI image is greater than a BSE image.

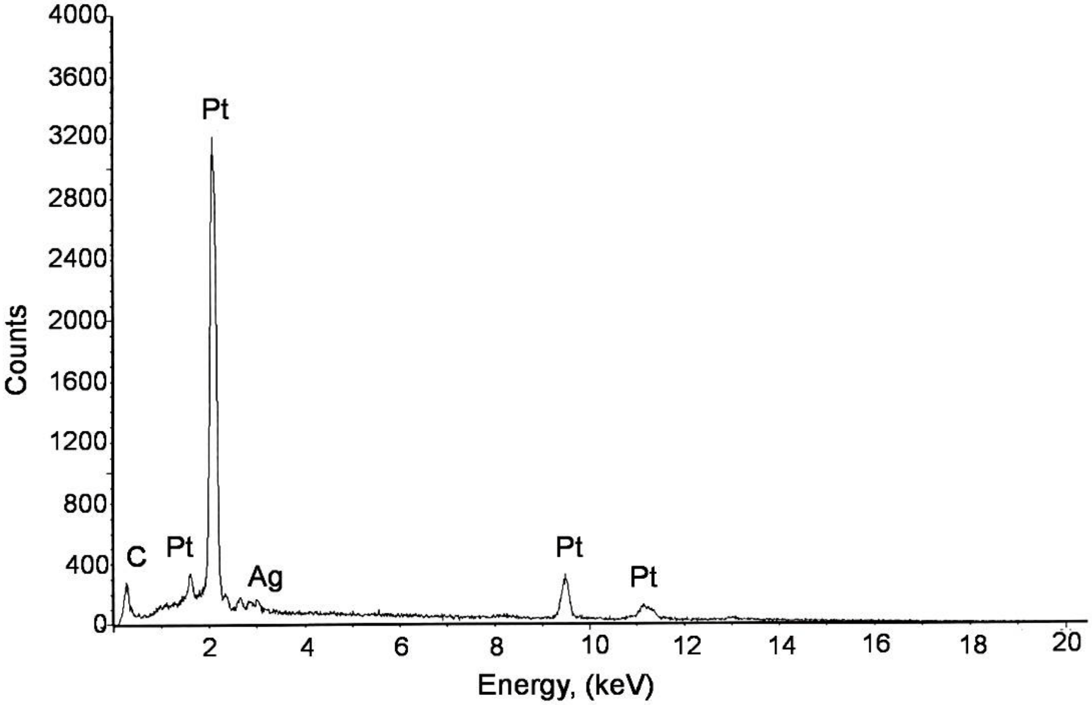

Figure 4.6: X-ray dispersive spectroscopy of Pt sites. Spectral analysis confirmed that the recording sites are primarily composed of platinum. The multiple platinum peaks on the graph are associated with excitation energy levels of different electron orbitals. X-ray emissions corresponding to carbon and silver were also detected. No other elements were detected.

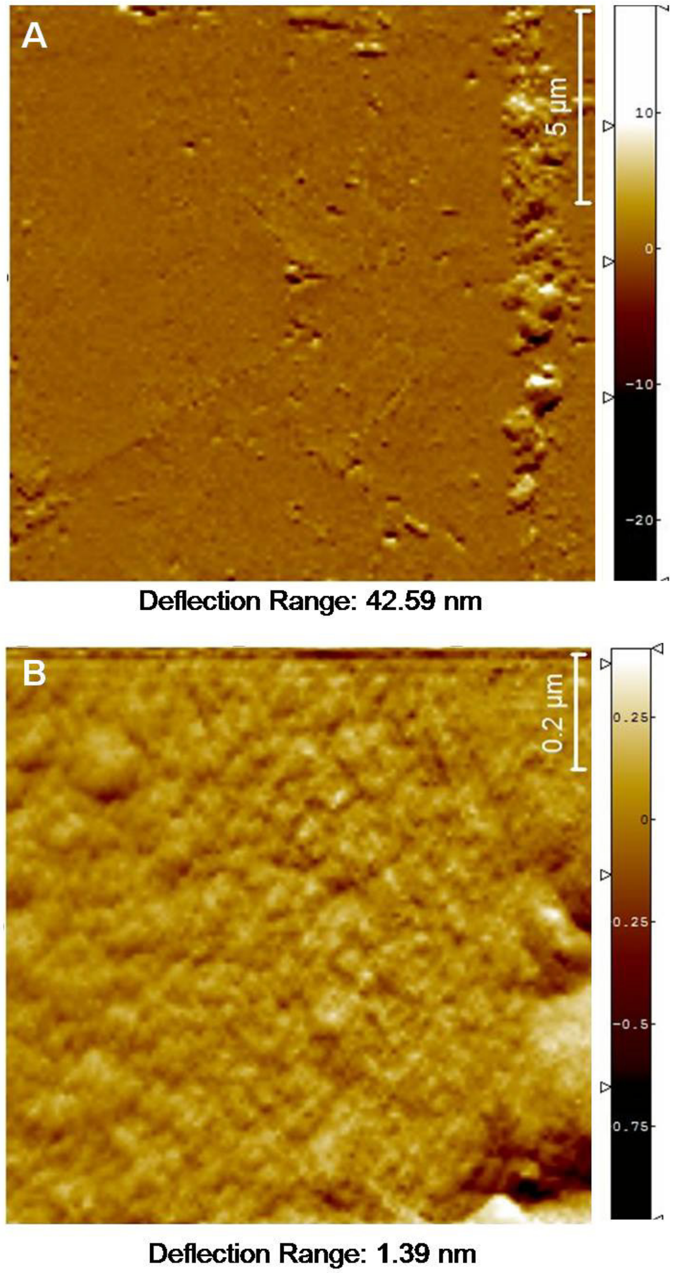
A
5 µm
10
0
-10
-20
Deflection Range: 42.59 nm
B
0.2 µm
0.25
0
0.25
-0.5
0.75
Deflection Range: 1.39 nm

Figure 4.7: Atomic force microscopy of Pt sites. Topographical representation of Pt recording surface: 15×15 µm (image A) and 1×1 µm regions (B). Variations in surface height are shown in the form of a color gradient. Lighter shading is indicative of regions with raised topography while darker areas correspond to indentations or cavities.

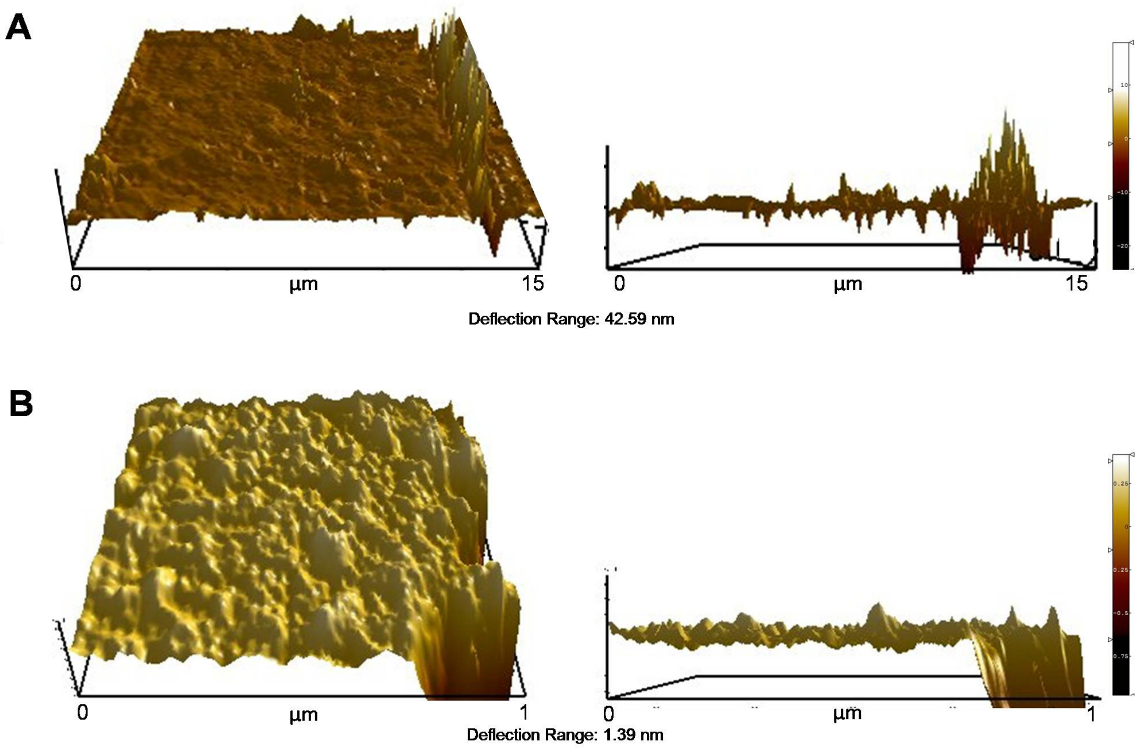

Figure 4.8: Three dimensional projections of Pt topography data. Graphs A (15 µm^2) and B (1 µm^2) illustrate the shape and general distribution of peaks and holes across sampled regions of the Pt site (perspective and profile views) on the MEAs. Height scale and deflection range were adjusted for optimum viewing of topographical information.

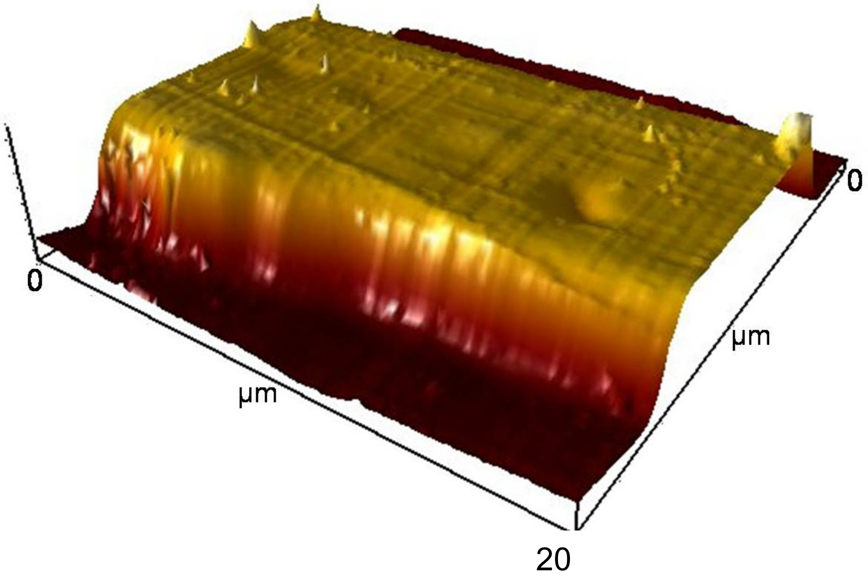

Figure 4.9: Representative polyimide coated connecting line. Portion of a polyimide coated Pt connecting line shown over a 20 x 20 μm region. Height scale and deflection range were adjusted for optimum viewing of topographical information. The connecting line is approximately 10 μm wide.

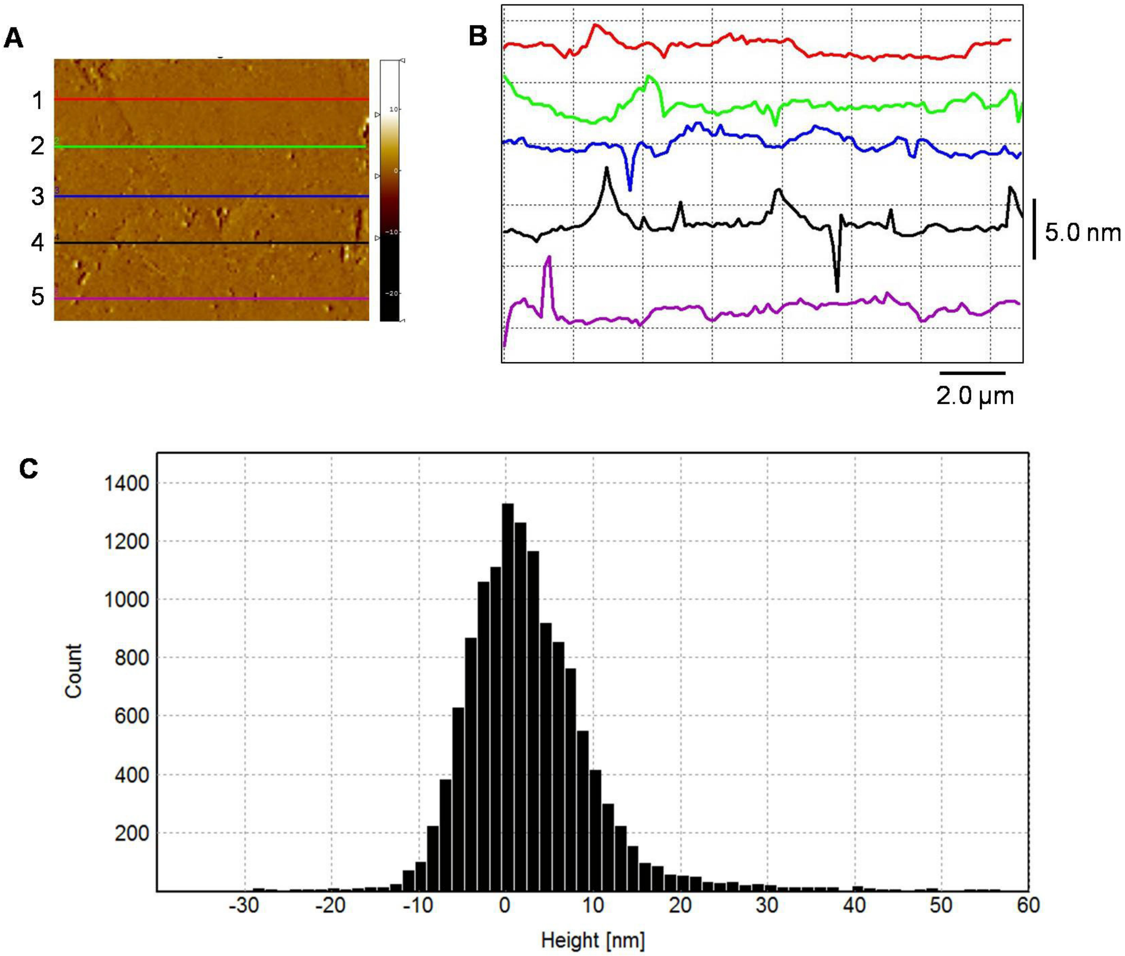

Figure 4.10: Multiple line profiles and frequency distribution of surface features on Pt sites. Panel A shows the line locations for multiple line scan analysis on a 15x15 µm section of a Pt site. Panel B shows the corresponding line profiles. Surface topography along each line was dominated by nanometer sized peaks and holes (absolute height < 5 nm). Panel C is a frequency distribution graph showing the total number of surface features on each Pt site.

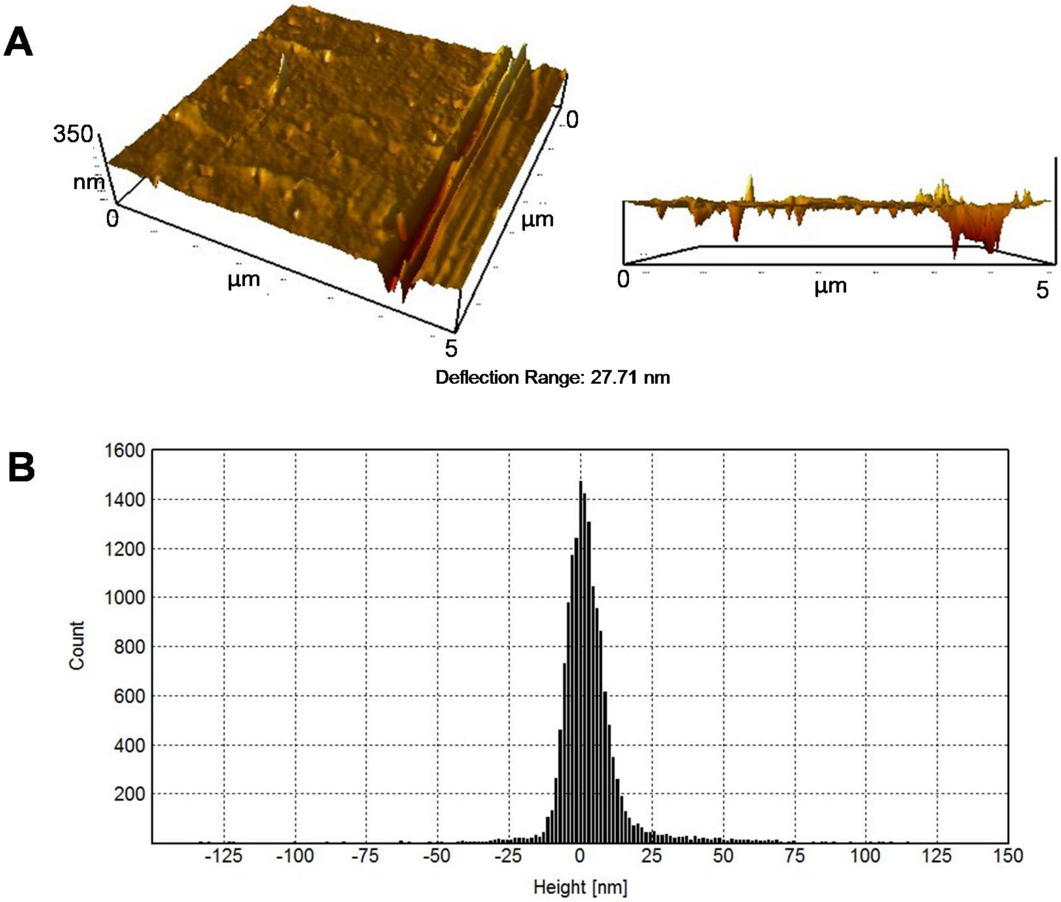

Figure 4.11: Frequency distribution of surface features on ceramic substrate. Panel A is a three dimensional projection of the reverse MEA surface over a 5x5 µm area. Panel B is a frequency distribution graph of surface heights over this area and shows that negative heights were the dominant surface feature.

Table 4.1 Pt Site Sensitivity for Hydrogen Peroxide

Type	Surface Modification	Method	Sensitivity ($pA \cdot \mu M^{-1} \cdot mm^{-2}$)	Source
Disk	Polished	Amperometry	1.4	O’ Neill et al., 2003
Disk	Polished	Amperometry	6800	Guascito et al., 2008
MEA	-	Amperometry	>9100	Burmeister et al., 2002
Planar	Pt nanowires	Amperometry	5.4	Yang et al., 2006

Table 4.2 Sample Roughness Analysis of Platinum Recording Sites

	R_{AVG} (nm)	R_{RMS} (nm)	R_{SKEW}	H_{MAX} (nm)	$\lvert D_{MAX} \rvert$ (nm)
Site 1					
15 μm^2	6.3	10.0	2.4	78.3	99.1
1 μm^2	1.6	2.4	1.9	6.2	18.2
Site 2					
15 μm^2	6.8	11.3	2.7	85.9	179.4
1 μm^2	3.3	7.5	-4.7	61.3	12.3
Site 3					
15 μm^2	17.9	30.0	3.8	219.0	368.6
1 μm^2	1.6	2.2	1.6	5.2	7.6

For each site, $N_{SAMPLES}$ per site = 3, $N_{ITERATIONS}$ per sample = 3

15 μm^2 Sampled Region: Height scale= 0 - 150 nm

1 μm^2 Sampled Region: Height scale= 0 - 20 nm

Table 4.3 Sample Roughness Analysis of Reverse Ceramic Surface

.	R_{AVG} (nm)	R_{RMS} (nm)	R_{SKEW}	H_{MAX} (nm)	$\lvert D_{MAX} \rvert$ (nm)
MEA 1					
front	145.2	208.5	0	574.3	110.7
back	32.5	46.9	-1.8	132.6	213.4
MEA 2					
front	125.8	180.0	-1.5	314.2	568.4
back	6.0	10.7	-1.13	97.4	-200.0

$N_{ITERATIONS}$ per sample = 3

Chapter Five: Investigations of Microprinting Technology as a Novel Protein - Coating Tool for MEA Recording Surfaces

5.1 Introduction

We have developed ceramic based MEAs for acute and chronic measurements of hippocampal single unit neuronal activity and neurotransmitter regulation. The working sites of our MEAs are arranged in dorsal-ventral pairs at the tip of the electrode. The built-in redundancy of this arrangement is useful for verifying neurotransmitter changes in a given region or for identifying discrete neuronal activity. However, for future dual recordings with multiple analytes, our current manual enzyme-coating procedure must be modified to allow greater control during enzyme application.

The present studies investigated the coating methodology and salient characteristics of two computer-controlled microprinting devices, namely the Nanoject microplotter and the Jetlab® microprinter. The former was custom-designed by our lab to allow micrometer precision for enzyme application (Courtesy: Thomas Coates). The second system is a commercial microprinting station (Microfab Technologies, Plano, TX) that can be adapted for enzyme coatings. Choline oxidase and xanthine oxidase were selected for optimization studies because they are relatively inexpensive compared to other oxidase enzymes.

5.2 Materials and Methods

Please refer to Chapter Two for a detailed explanation about the principles of piezoelectric-based inkjet printing utilized by the JetLab4® microprinting station. Section 2.10 also includes details on cleaning procedures for jetting device preparation and a brief overview of the JetLab4 software.

5.3 Results and Discussion I: Nanoject Microplotter System for Application of Enzyme Coatings on MEAs

The experiments described in this study have a considerably longer down time (30 – 60 minutes) when compared to manual coatings (10 – 15 minutes). Since gluteraldehyde is a strong cross-linking molecule, it was necessary to prepare a solution of containing gluteraldehyde alone and a separate protein solution of bovine serum albumin and enzyme. This prevented clogging of the micropipette (or jetting device in section 5.4). In addition, the concentration of BSA and protein concentration was 50% less than manual coatings (0.05% BSA and 1 unitµL^{-1} Choline Oxidase) while the gluteraldehyde concentration was increased from 1.25% to 5%. The lower protein concentration aided in reduced clogging of the tip while the higher gluteraldehyde concentration facilitated cross-linking on the Pt site.

5.3.1 Coating Methodology for W4-MEAs

The Nanoject Microplotter is a pressure-controlled continous jetting system. Therefore, a pressure trigger causes the release of fluid from the micropipette tip in the form of a continuous stream. Precise application of coating solutions on each Pt site (Site width = 20 µm) of the MEA was achieved by using micropipettes with a tip diameter of 20 – 30 µm and by positioning the tip directly over (but not in contact with) the Pt site. Only one nozzle could be used at a time; therefore, solutions of BSA/enzyme and gluteraldehyde were applied in tandem. Clogging of the nozzle was prevented by using separate micropipettes for gluteraldehyde and enzyme solutions or by flushing the micropipette with water between solution applications.

We empirically determined that at least 8 serial applications of enzyme solution and 4 applications of gluteraldehyde were needed to produce a stable cross-linked enzyme layer. The performance of these MEAs was compared to manual coatings. As seen in Figure 5.1, average slope and LOD values were not significantly different between MEAs coated manually (1.4 x 10^{-2} nA·µM ±

1.4x10-^{3}) and the with the nanoject microplotter (1.0 x 10-$^{-2}$ nA·µM ± 1.6 x 10^{-3}). Thus, the nanoject microplotter allowed for discrete application of enzymes on Pt sites while also maintaining the recording performance of these MEAs.

5.3.2 Challenges of Coating Procedure

Three main findings impacted the ease of using the Nanoject Microplotter for routine enzyme coatings. First, the three dimensional motion of the micropipette and the release of fluid was completely under human control. While this allowed for greater coating precision, it also led to much longer coating times (2-3 minutes per solution per MEA). Secondly, the present system utilizes a fixed stage and moving printhead. This made it difficult to maintain the fluid stream in continuous focus of the viewing microscope. Finally, a steady fluid flow was observed only when relative humidity (RH) levels were > 60% at room temperature. Though the entire unit was housed in a partially sealed Plexiglas® chamber, approximately 4 hours were needed to raise the RH to desired levels. Thus, during a single coating session, a turnover of 14 - 16 MEAs was achieved with an active coating time of 60-90 minutes and a downtime of 30-40 minutes, excluding time taken to reach desired RH levels. These challenges may be addressed in part by automating the coating process and by fitting the microscope with a viewing system such as a camera or computer monitor.

5.4 Results and Discussion II: Jetlab® Microprinting Station for Application of Enzyme Coatings on MEAs

The Jetlab® microprinting station is a piezoelectric pulse-controlled jetting system. Therefore, application of a brief potential causes release of fluid from the tip of the jetting device in the form of droplets. The primary goal of this study was to determine a range of operating conditions that allowed accurate printing of Pt sites on W4-MEAs. This included optimization of droplet size, characterization of drying behavior and evaluation of MEA performance. The latter was conducted at

Microfab laboratories (Data courtesy Thom Coates and David Silva) and at the University of Kentucky.

5.4.1 Calibration of Viewing Cameras and Translation Stages

The Jetlab4® hardware and software are provided with some basic printing and testing capabilities such as a two-camera system that allows visualization of ejected droplets (drop-observation camera) and printed substrate (inspection camera) and user-defined calibration of stage motion. Water sensitive paper (Ritterhouse Co., CA) was used as a print substrate for all calibrations. The jetting device used in the present study is capable of generating droplets with picoliter volumes (Cooley et al., 2001); therefore a 2X zoom lens was fitted onto the inspection camera (downward-viewing) to allow droplet visualization on the paper. Droplet evaporation and drift in droplet placement were minimized by maintaining a height separation $\leq$ 2 mm between the jetting orifice and the MEA tip (Figure 5.2). A screen-scale calibration was used to determine a scale transformation from the coordinated motion of the stages in x- and y- directions to the displacement calculated by the imaging software, as seen by the substrate observation camera (Figure 5.3 A). This step was necessary to determine the size of the impacted droplet, and for identifying the exact location of the MEA Pt sites for printing. Next, a head-to-lens vector was calculated to determine the distance to be moved in the x-y plane to place a spot from directly under the jetting device to the center of view of the substrate observation camera (Figure 5.3 B). Finally, a test pattern was printed to correct for systematic deviations in the placement of droplets over time (Figure 5.3 C).

5.4.2 Characterization of Pulse Parameters for Formation of Droplets

Formation of a droplet at the tip of the nozzle is controlled at the gross level by a pneumatics box that allows control over positive and negative pressure. For gluteraldehyde solution, we determined that a slight negative pressure (-2 to -6 psi) was needed to release drops along a vertical trajectory. A greater negative pressure (-4 to -12 psi) was needed to see similar behavior with choline oxidase and xanthine oxidase solutions. The back pressure also minimized formation of satellite droplets. Fine control of droplet size and shape was achieved by altering the characteristics of the pulse driving droplet ejection, particularly the voltage and dwell times.

Figure 5.4 depicts the unipolar square waveform that was used for gluteraldehyde solution. A separate waveform was generated for enzyme solutions because of the propensity of these fluids to dry at the jetting tip. Figure 5.4 also shows a bipolar squarish waveform that combines features of square and sine waves. This particular pulse caused low-level agitation of the meniscus at the opening of the nozzle and minimized clogging. For each waveform, we selected the lowest combination of voltage and dwell times to obtain the smallest possible drop size. The Jetlab® software uses strobed illumination to estimate the size, volume and planar deviation of droplets in mid-flight, allowing real-time measurements of droplet characteristics. Voltage values between (±) 26 – 40 V and dwell times between 10 – 25 µs produced stable droplets (diameter 60 – 85 µm) for both glutaredehyde and enzyme solutions.

5.4.3 Drying Behavior of Droplets on a Ceramic Substrate

For each solution, the drying behavior of droplets was evaluated. Droplet characteristics were studied on a bare ceramic wafer to approximate drying behavior on an MEA. The chemical and surface composition of the wafer was identical to our MEAs. These experiments were conducted in a room maintained at a constant temperature of 30°C and relative humidity of 30%. With each of the three solutions, a few principal behaviors emerged when the distance between adjacent drops was altered. Figure 5.5 shows photographs of these line morphologies. Droplets spaced at distances greater than two times the droplet radius dried as individual features. Decreasing the drop spacing to 1/4th of the droplet radius allowed interaction between adjacent droplets. Partial merging was observed though the original contact lines (droplet shape) were preserved, resulting in the appearance of the ‘scalloped’ morphology. We noted that the width of the scalloped was less than isolated droplet width, likely due to movement of the fluid along the axis of the line which decreased lateral expansion (Soltman et al., 2008).

Further reduction of drop spacing eliminated the scalloped appearance and produced a smooth, straight line. The width of these lines was the narrowest of all observed line morphologies. Specifically, straight lines were obtained when droplet spacing was between one-third and one-half of the radius. Finally, drops that were printed closer than one-half of the radius demonstrated bulging along discrete regions of the line. A recent study by Duineveld et al (2003) modeled similar behavior in screen printed circuits. Their study proposed that droplets tend to maintain their shape following substrate impaction because of surface tension. However, when the amount of fluid exceeds the contact angle of the droplets, surface tension cannot be maintained; therefore, droplets flow beyond the initial contact angle, producing the bulge-like behavior observed in both studies.

5.4.4 Automation of Coating Process

Using this data, we generated a custom script that printed arrays of droplets with straight line morphologies. The script controlled stage motion and droplet formation through the Jetlab® software (Sample script shown in Figure A.1). MEAs were loaded on a custom Plexiglas® holder that aligned the tips in the same x, y, z direction and minimized movement during printing. The holder was fitted onto the stage provided for print jobs. The x-y coordinates of each site were coded into the script. Activating the script resulted in automated printing of individual coating solutions onto the MEAs. Separate jetting devices were dedicated for each enzyme solution and the gluteraldehyde solution to reduce the downtime of the coating process and to allow for selective coating of enzyme onto discrete sites. Figure 5.6 (left) shows an MEA with choline oxidase enzyme coated onto two discrete sites. Figure 5.6 (right) shows an MEA with xanthine oxidase on left Pt sites and choline oxidase on the right Pt sites. Red dye

(Rhodamine or Congo red) was mixed with coating solution to allow visualization of the enzyme layer.

5.4.5 *In Vitro* Performance of Microprinted MEAs

Initial testing of MEA performance was conducted at Microfab laboratories (data courtesy Thom Coates and David Silva). We empirically determined that at a droplet size of 20 µm, at least 4 coats of enzyme solution (~400 nL) and 2 coats of gluteraldehyde solution (~200 nL) were required to produce a stable enzyme layer. Together with the operating speed of the translation stages, the current coating methodology is capable of coating up to 30 MEAs within 30 minutes. *In vitro* testing demonstrated that the microprinting procedure produced enzyme coatings that were comparable to our manual coatings (Figure 5.7). At the present time, we have not been able to replicate the necessary droplet size or recording capability at the University of Kentucky. Light microscopy imaging showed that large droplets peeled away from the Pt sites, possibly due to poor cross-linking between gluteraldehyde and protein layers. Though future experiments will focus on increasing the relative humidity around the jetting orifice to reduce droplet size and increasing drying time, our preliminary investigations have been successful.

5.5 Conclusion

The present studies have provided a wealth of characterization data for two novel coating methodologies. Specifically, our studies on the Jetlab® system suggest that this coating methodology offers a greater range of coating capabilities, shorter coating time and greater control over solution properties.

Copyright © Pooja Mahendra Talauliker 2010

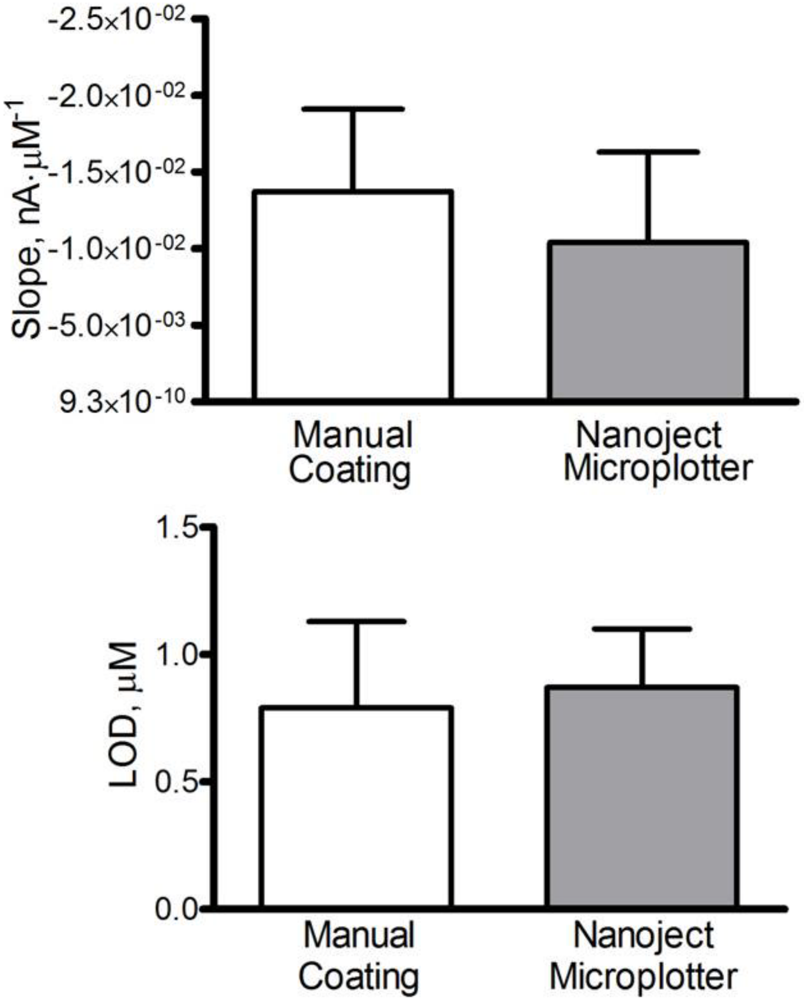

Figure 5.1: Comparison of slope and LOD characteristics of manually-coated and microplotter-coated MEAs. Statistical comparison of MEA performance using students' t-test found no significant differences between manual coatings (n = 14) and nanoject microplotter (n = 9) coatings with respect to average slope and LOD values.

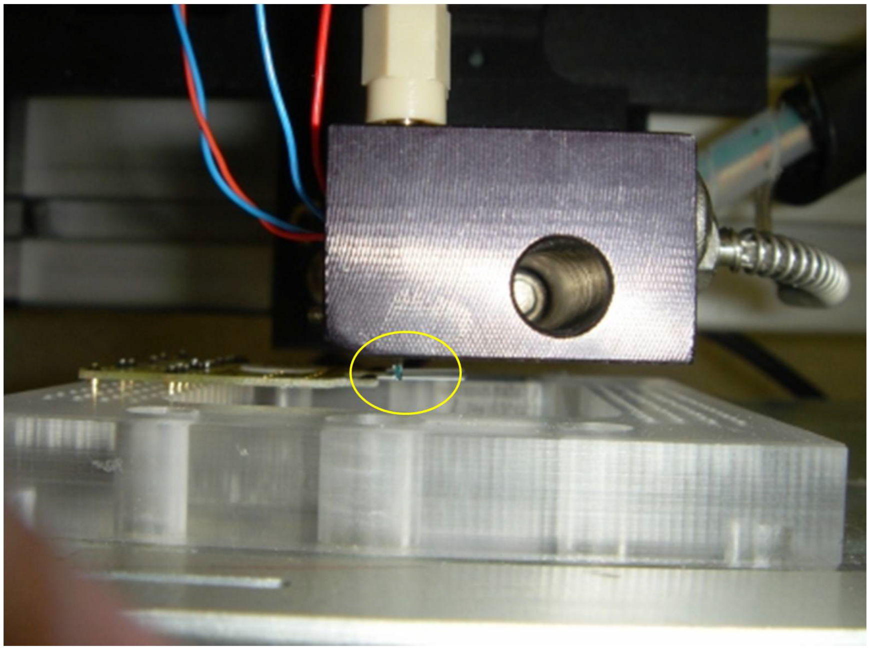

Figure 5.2: Vertical separation between jetting orifice and Pt Sites of MEA. The jetting device used in the present study generates droplets with picoliter volumes; therefore droplet evaporation and drift in droplet placement must be minimized by maintaining a height separation ≤ 2 mm between the jetting orifice and the MEA tip. Yellow circle enclose the jetting tip (filled with green dye) and the MEA tip.

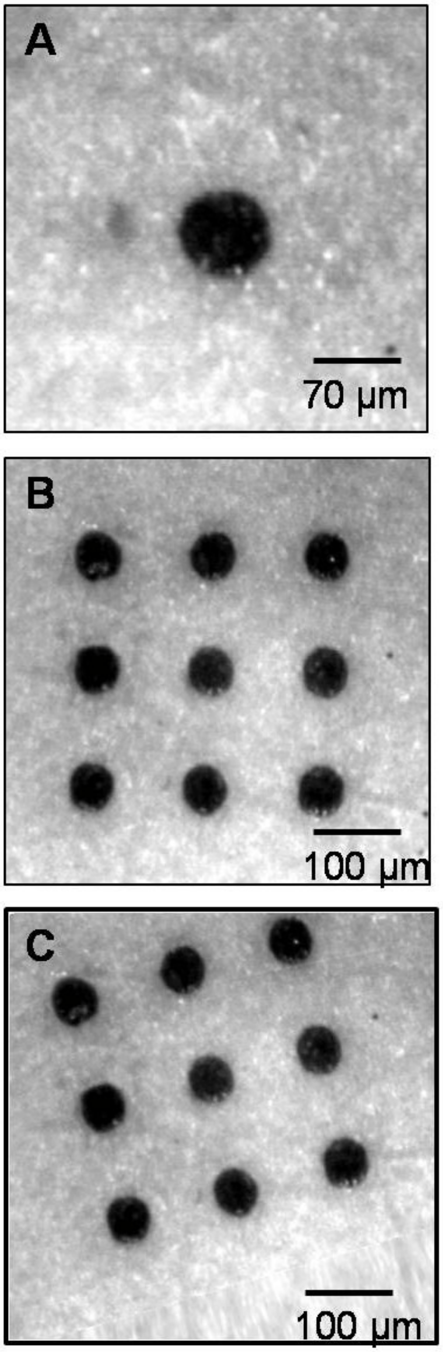
A
70 µm
B
100 µm
C
100 µm

Figure 5.3: Calibration of Jetlab® cameras and translation stages.

Figure 5.3 (contd.) Panel A shows a droplet on water sensitive paper. Screen-scale calibration of the camera can be used to determine the size of the droplet. Panel B shows a pattern used for head-to-lens vector calibration. If calibration was correctly performed, the center of the pattern will be positioned beneath the jetting orifice. This was necessary for locating the precise position of MEA Pt sites during printing. Panel C shows a pattern that is rotated by an angle of 20 degrees from its original position. Spot shift calibration was used to correct for this error by superimposing identical patterns in the same location and measuring the difference in the location of each spot. .

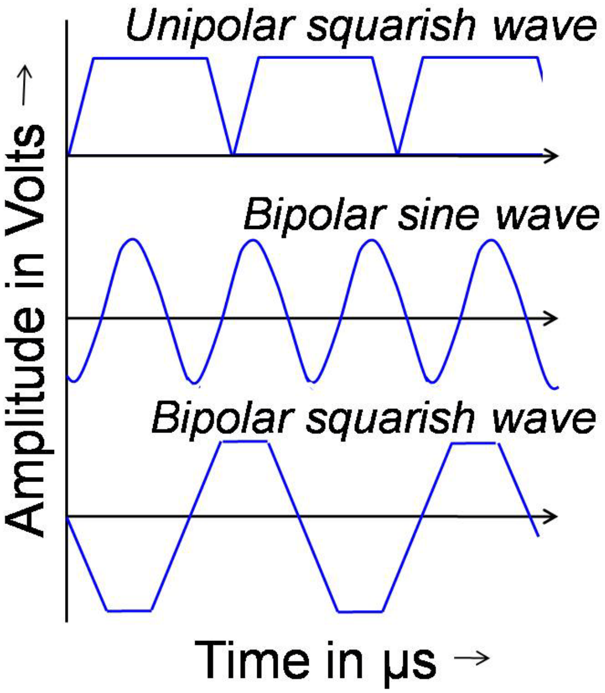
Unipolar squarish wave
Bipolar sine wave
Bipolar squarish wave
Amplitude in Volts →
Time in µs →

Figure 5.4: Pulse waveforms used to control droplet size. Fine tuning of droplet size and shape was achieved by altering the voltage and dwell times for the piezoelectric pulse. A unipolar square waveform was used for gluteraldehyde solution while a bipolar waveform that contained features of a square wave and a sine wave was used for BSA/Enzyme Coatings.

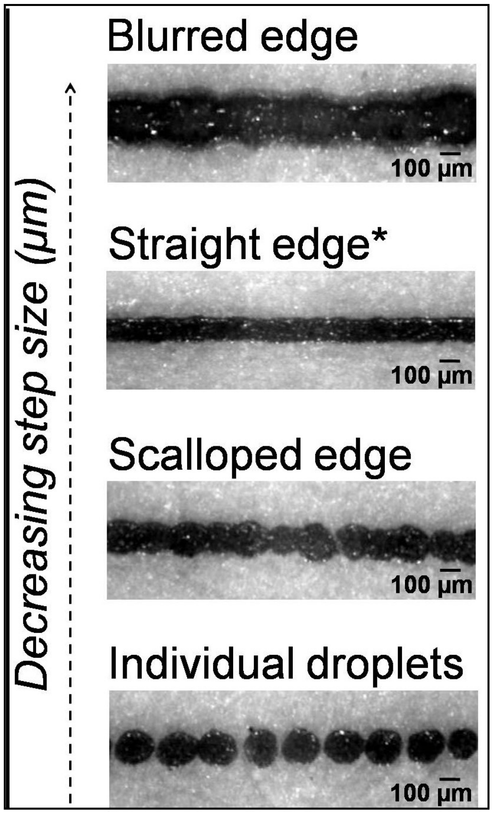
Decreasing step size (µm)
Blurred edge
100 µm
Straight edge*
100 µm
Scalloped edge
100 µm
Individual droplets
100 µm

Figure 5.5: Common droplet behaviors observed during microprinting. The behavior of protein and gluteraldehyde droplets following injection from the microprinting nozzle was evaluated at a constant temperature of 30°C and relative humidity of 30%. If droplets were printed at distances greater than two times the droplet radius, they tended to be too far apart to interact with each other. Decreasing the drop spacing to 1/4th of the droplet radius allowed droplet interaction and merging though the original contact lines (droplet shape) were preserved, resulting in the appearance of the 'scalloped' line. Straight lines were obtained when droplet spacing was between 1/3 and 1/2 of the radius Drops that were printed close than ½ the radius demonstrated bulging along discrete regions of the line.

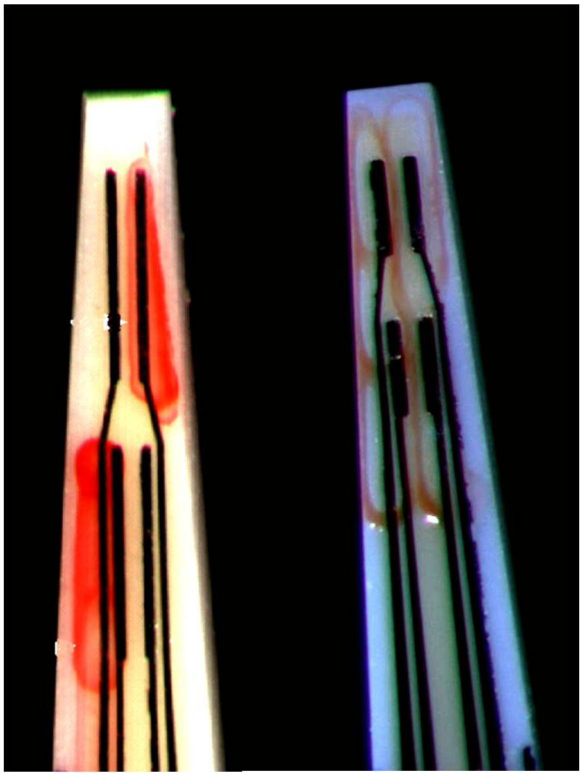

Figure 5.6: Examples of high precision enzyme coatings using Jetlab microprinting devices. The Jetlab® system allowed for precise application of enzyme coatings on discrete MEAs. The MEA on the left has two sites coated with choline oxidase and gluteraldehyde solutions. For the MEA on the right, Pt sites on the left side are coated with choline oxidase while sites on the right side are coated with xanthine oxidase. Red dye (Rhodamine or Congo red) was mixed with coating solution to allow visualization of enzyme layers.

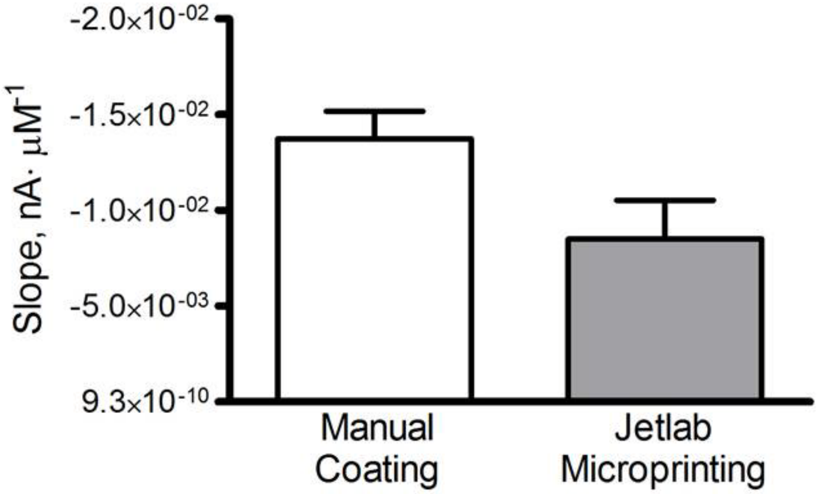

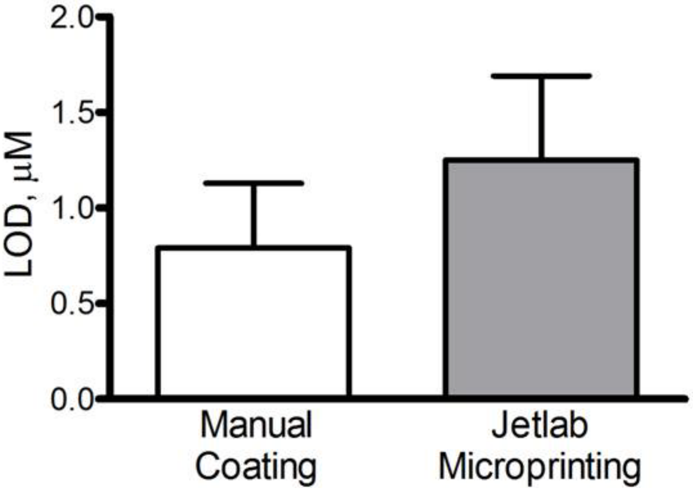

Figure 5.7: Comparison of slope and LOD characteristics of manually-coated and Jetlab®-coated MEAs. Statistical comparison of MEA performance using students' t-test found no significant differences between manual coatings (n = 14) and Jetlab® microprinter coatings (n = 11) with respect to average slope and LOD values.

Chapter Six: Characterization of Tissue Responses to Chronic MEA Implantation in the Hippocampus

6.1 Introduction

In vivo monitoring of extracellular glutamate is of interest to researchers investigating synaptic mechanisms of hippocampal-dependent learning and memory formation because the nerve terminals involved in synaptic communication release glutamate molecules that in turn activate post-synaptic glutamate receptors (Danbolt, 2001; Manabe, 2008). Outside of its role as an excitatory neurotransmitter, glutamate is implicated in the pathophysiology of diseases known to involve the hippocampus. An acute rise in basal glutamate has been reported before and during a seizure event in the hippocampus of patients with temporal lobe epilepsy (Cavus et al., 2005). In contrast, an overall decrease in hippocampal glutamate has been shown for patients with Alzheimer's disease (for review see Greenamyre and Young, 1989). In both cases, histopathological evidence for excitotoxic tissue damage has been demonstrated (During and Spencer, 1993; Armstrong et al., 2003, respectively). Therefore, there is also a need in the medical community to develop treatments that control the adverse effects of glutamate dysregulation. Studies that combine glutamate investigations with behavioral measurements offer the potential to correlate neurochemical data with real time changes in hippocampal function. Therefore, an investigative or diagnostic technique that allows chronic glutamate measurements over multiple days is needed.

Microdialysis has been the historical gold standard for *in vivo* neurochemical measurements though the slow sampling rate of this technique (5 – 20 minutes) is a significant limitation for measuring the rapid release and clearance of glutamate in the brain (milliseconds – seconds) (Kennedy et al., 2002; Watson, Venton and Kennedy, 2006). Chronic microdialysis experiments usually last for only 6- 8 hours (Clapp-Lilly et al., 1999; Kennedy et al., 2002). Further, the large-sized microdialysis probes (1 - 4 mm length, 0.2 - 0.3 diameter) produce considerable tissue damage (Clapp-Lilly *et. al*., 1999). Alternate technologies with improved spatial and temporal resolution have been developed using principles of electrochemistry. Of these, carbon fibers and hydrogel-based electrodes have demonstrated success for measuring brain concentration of catacholamines (Suaud-Chagny et al., 1993, Westerink, 2004) but not for excitatory amino acid neurotransmitter recordings.

We have refined the salient features of both techniques and combined them into a single versatile technology by developing ceramic-based MEAs for chronic neurotransmitter measurements (Rutherford et al., 2007). The current state of the technology allows for chronic glutamate measurements up to 7 days in the prefrontal cortex (Rutherford et al., 2007) and up to 6 days in the hippocampus (refer Chapter 3). Because the working sites of our MEAs are composed of Pt, we also have the capability to record single unit neuronal activity (Opris et al., 2009). In fact, chronic MEAs implanted into the rat hippocampus have been shown to perform reliably for as long as six months (unpublished data). Chapter 5 chronicled our efforts to modify our coating methodology to allow improved adhesion of the enzyme layer to the Pt sites, particularly because future experiments will involve long term chronic recordings with indwelling MEAs. Parallel studies on the tissue responses to chronic MEA implantation have conducted in the rat prefrontal cortex (PFC) (Hascup et al., 2009). Immunohistochemical analysis of PFC tissues showed minimal tissue damage and inflammation around MEA track up to six months. We believe that a separate evaluation is needed for hippocampus implants because the unique anatomy and physiology of this brain structure makes it vulnerable to damage from penetrating electrodes. For example, Shorvon and Fish (2004) noted that insertion of depth electrodes in the rat hippocampus was sometimes followed by a sudden rise in activity of local neurons. Electroencephalographic data (EEG) from their study was similar to electrical activity seen in transient epileptogenic foci (Meldrum and Chapman, 2000). Similar observations have been reported by others, with a greater likelihood of these occurring in the aging or diseased hippocampus (Karhunen et al., 2005).

It is important to note that astrocyte numbers in the hippocampus are greater than most other brain regions (Savchenko et al., 2000) and are shown to increase in an age-dependent manner (Takahashi et al., 2006). Astrocytes are one of two major glial cell types participating in the inflammatory reaction to tissue injury following electrode insertion (Biran et al., 2005, 2007). The other cell type is microglia. These cells undergo morphological changes and accumulate around the electrode in the days and weeks following implantation (Turner et al., 1999, 2001). Furthermore, it is widely suggested that astrocytes and microglia form a physical barrier that limits electrode access to healthy neurons (Polikov, Reichert and Tresco, 2005). For glutamate investigations, glial changes in the recording environment of the MEA present an additional challenge. Specifically, glutamate transporters located on the cell membrane of astrocytes are the primary mechanism by which glutamate is cleared from the extracellular environment (Danbolt, 2001). The effect of astrocyte changes on glutamate regulation is unknown.

The present study investigates tissues responses to chronic MEA implantation in rat hippocampus. These experiments utilized non-recording MEAs fitted with the complete recording pedestal and studied at time points 1, 3 and 7 days and 8, 16 and 24 weeks to evaluate the full biological response. Edema and hemorrhaging immediately following surgery was studied by magnetic resonance imaging (MRI) and cresyl violet staining. The latter was also used to verify electrode placement and visualize the gross morphology of neuropil at each time point. Changes in the morphology and distribution of hippocampal astrocytes and microglia were determined using fluorescent antibody markers for glial fibrillary acidic protein (GFAP) and microglial ionized calcium-binding adaptor molecule 1 (Iba1). Throughout this study, contralateral hippocampal tissue was used as a control. GFAP was also used to determine astrocyte adhesion to the MEA surface. Lastly, scanning electron microscopy (SEM) was used to study post-surgery changes in MEA topography.

6.2 Materials and Methods

Chapter Two contains a comprehensive description about the experimental design and methodology followed in this study including fabricaton and preparation of chronic MEAs, implant construction and *in vivo* assembly, protocols on animal use, post-experimental tissue processing, microscopy procedures, data selection and statistical analyses. For details about a specific technique, please refer to relevant sections within this chapter.

6.3 Results

Animals exhibited normal behavior within 4 hours post-surgery and had minimal post operative complications. At autopsy, we found that one animal had improper MEA placement, one had extensive hemorrhaging, and two showed signs of infection. These animals were removed from the study. We continue to improve our surgery technique; however it is important to note that the present experiments had a low complication rate.

6.3.1 Post-surgery Magnetic Resonance Imaging (MRI)

T1-weighted MRI of rat brain tissue were conducted immediately following MEA implantation in the right hippocampus (Figure 6.1, A - L). A water-filled capillary tube was used to mark the implanted hemisphere in these images. Tissue was studied in serial coronal sections (500 µm thickness) to allow gross visualization of the brain-MEA interface. Diminished contrast observed at the insertion site suggested the presence of edema or hemorrhaging in the extracellular environment surrounding the MEA (Figure 6.1 F - J). In addition, a dark spot was noted near the track in sections C-E, possibly a microhemorrhage in the sagittal plane that was caused during stereotactic insertion of the probe. The temporal effects of these changes are described in the following sections using conventional histology and immunohistochemistry.

6.3.2 Cresyl Violet Staining

The distribution of cresyl violet in tissue sections was consistent with accepted anatomical distributions of neuroglial cells in the rat hippocampus. Moderate increases in staining (50 μm away from the track) were detected near the implant track at day 1(Figure 6.2, A, C). Increased staining persisted up to 1 week (Figure 6.2 B, D) and was accompanied by small amounts of debris from disruption of local vasculature. Moderate amounts of debris seen in the brain parenchyma overlying the hippocampus was caused by bone screws that were inserted too deep into the skull, evidenced by tissue disruption in both hemispheres. The implant cavity was free of cellular matter. At 8 weeks post-surgery, distinct morphological changes were observed in tissue sections. A thin layer of scar tissue lined portions of the insertion site, though this was not apparent at low magnification (Figure 6.3 A, C). Very few samples contained artifacts from hemorrhaging, suggesting that products of vascular disruption had been cleared from the extracellular fluid by this time. The track produced by the MEA was larger at 8 weeks (50 - 200 μm) and irregular in shape. Bands of tissue and some scattered cells were observed inside the track and may have torn away when the probe was removed. It was not possible to determine whether the enlarged cavity was the result of *in situ* tissue damage or implant retrieval. Similar changes were observed in hippocampal tissue sections 4 months after surgery (Figure 6.3 B, D).

6.3.3 GFAP and Iba1 Immunoreactivity

In the present, a cell with stellate morphology and positive immunoreactivity to glial fibrillary acidic protein (GFAP, red) was assumed to be an astrocyte. Similarly, cells showing positive immunoreactivity for ionized calcium-binding adaptor molecule 1 (Iba1, green) were taken to be microglia. Simultaneous detection of these cell types was achieved by exposing hippocampal sections to both protein markers and studying the co-labeled tissue by indirect immunofluorescence. Altered levels of GFAP near the insertion site were not readily apparent at days 1, 3 or 7 following implantation because of overwhelming Iba1 immunoreactivity in this region. In addition, the pattern of GFAP distribution in the hippocampus made it difficult to distinguish between normal and reactive astrocytes at these time points (Figure 6.4 A – F). Very few GFAP positive astrocytes were observed inside the track or along its perimeter. Thus, we tentatively suggest that astrocytes may not be a major component of the cellular sheath up to 7 days post-implantation.

Hippocampal coronal sections obtained 8 weeks post-surgery demonstrated intense GFAP immunoreactivity around the implant track (Figure 6.5 A, C). The extended processes of reactive astrocytes contributing to the glial scar were readily distinguishable from normal astrocytes. These processes formed long tangled bundles that radiated away from the track perimeter, extending up to 100 μm into surrounding tissue. Interestingly, cell bodies could not be visualized within the glial sheath, though the tangled morphology of the processes suggested a multilayered composition. Similar to the cresyl violet data, the track was wider at later time points. The track interior also contained isolated filamentous particles that were GFAP immunoreactive. These particles may be astrocyte processes that broke off during implant retrieval. At 4 months (16 weeks) post-surgery, the width of the glial sheath decreased and became more compact (Figure 6.5 B- D). Gliotic tissue was still multilayered though a decrease in the total number of cells was observed. Interestingly, cell bodies were now distinguishable from each other and there was a marked decrease in the length of astrocytic processes. As before, the inner surface of the cellular sheath was disrupted, evidenced by irregular lumen shape and ribbons of dislodged gliotic tissue extending across the track. This type of partial tissue disruption in long term implants suggests that adhesion between cells in the sheath was comparable to cell adhesion at the MEA surface.

Quantitative estimation of total GFAP immunoreactivity at all data points showed that increased staining intensity was detected at day 1 following MEA implantation (Figure 6.6). A significant increase in intensity levels was measured at 1 week ($p<0.001$). Beyond 8 weeks a decrease in GFAP levels was noted though overall immunoreactivity remained significantly elevated ($p<0.05$) for the duration of the implant.

Figure 6.4 (A - F) also shows representative images of Iba1 immunoreactivity (green) in the hippocampus at days 1, 3 and 7 following MEA insertion. At distances greater than 50 μm from the track, low levels of Iba1 were detected throughout the hippocampus. Based upon their stellate morphology, most cells appeared to be non-reactive. Reactive microglia with amoeboid morphology were observed close to the implant cavity and were surrounded by an amorphous fluid-like substance that also showed low-level immunoreactivity. At days 3 and 7, microglia formed a diffuse multilayered network. The absence of a defined implant cavity suggested that the microglial sheath collapsed when the MEA was removed, indicating poor intercellular adhesion. Increased microglial content in the overlying cortical layers were correlated with tissue damage noted in cresyl violet sections. Iba1 immunoreactivity subsided dramatically by 8 weeks and was not easily differentiated from control tissue at later time points (Figure 6.5 A – D). Furthermore, images obtained at high magnification showed that very few cells exhibited amoeboid morphology.

Since Iba1 is a generalized marker for microglia, the proportion of reactive and unreactive cells at various time points could not be determined. Despite this, gray level measurements revealed interesting quantitative data about total Iba1 content in implanted tissue. Gray intensity measurements obtained 1 day after microelectrode implantation were slightly decreased when compared to control tissue. These levels became significant at 1 week ($p < 0.05$). Total intensity levels remained significantly high until 8 weeks, though wide variance was observed in the data at this time point (Figure 6.6). Diminished gray levels were seen at 4 and 6 months.

6.3.4 Surface Characterization of Explanted MEAs

Following implant removal from perfusion-fixed tissue, tissue adhesion on MEA surfaces was investigated using SEM. Samples were viewed in a high vacuum environment; therefore, some distortion of cellular architecture was expected. All MEA showed evidence of attached biological material. However, the distribution of tissue was variable between samples. For the MEAs examined in this study, there was no correlation between implant time and tissue content. Other than the probe shown in Figure 6.7 B, only one other MEA was covered with thick layers of closely associated cell matter. In both samples, the microstructure of the probe was not visible and individual cells or cell processes could not be distinguished. All other samples were similar to probe A where the recording surface had very little tissue and only a few scattered cells (Figure 6.7 C). Adhering material was usually found on the sides or along edges in isolated clusters. High magnification images showed that some of these clusters were composed of cellular debris in multiple layers that were held together by a smooth amorphous material (Figure 6.7 C, D). We also observed cell-free regions covered solely by the amorphous layer (Figure 6.7 E). Both types of tissue could be found on a single probe. For example, the MEA in Figure 6.7 A has a coating on the vertical side near the base that starts out as an amorphous layer that transitions into a thin cell-like layer and fuses with a thick tissue cluster on the horizontal surface.

Finally, a subset of freshly removed MEAs was retained for tissue fixation and immunohistochemistry analysis. Except for a discrete region on one probe (Figure 6.8 A), all samples were negative for GFAP indicating an absence of astrocytes on MEA surfaces. High magnification imaging of the GFAP positive region showed fragment resembling astrocytic processes, but no whole cells (Figure 6.8 C). The amorphous coating detected during SEM was also observed during confocal imaging in the form of a thin layer that covered most of the MEA (Figure 6.8 B, D). The identity of this material could not be determined. Additional immunological markers were not tested because the SEM and GFAP studies collectively suggest that attachment of non-astrocytic cells on the MEA surface was unlikely. These results also support that the large void left behind in tissue sections is not to due to removal of tissue during implant retrieval.

6.4 Discussion

These studies demonstrate that our chronic MEAs were well-tolerated in the hippocampus up to six months post-surgery. MEA insertion into the brain produced edema, hemorrhaging and rapid alterations in local microglia and astrocytes. At all time points, the MEA was surrounded by a highly active cellular sheath that was immunoreactive for GFAP (astrocytes) and Iba1 (microglia). Temporal changes in the morphology and spatial distribution of cells inside the sheath and in surrounding tissue were studied by immunohistochemical staining, which also allowed quantification of fluorescent intensities and comparison with control tissue samples. Briefly, Iba1 levels were significantly elevated from 1 to 8 weeks post-surgery but were diminished at later time points. GFAP immunoreactivity was also significant by 1 week remained high even 6 months after surgery. Interestingly, the cellular sheath produced in response to MEA insertion was less than 100 μm wide suggesting that only tissue in the immediate vicinity was affected. After 4 months, the sheath contracted and became more compact, further reducing the extent of the biological response (≤ 50 μm). These results indicate that minimal tissue damage resulted from insertion of the probe and its prolonged presence in the hippocampus. Only two explanted probes (out of 30) showed limited GFAP immunoreactivity confirming a lack of astrocytic content on the ceramic surface. In addition, SEM studies showed that very little tissue adhered to the ceramic surface indicative of weak cell attachment to the implant. As discussed below, these findings have important implications for future electrochemical and electrophysiological investigations involving chronic MEAs.

6.4.1 MEAs are Well-Tolerated in the Rat Hippocampus

The present studies demonstrated that our MEAs were well-tolerated up to six months in the hippocampus, a brain region known for high susceptibility to trauma-induced neurodegeneration (Shorvon and Fish, 2004). The low complication rate observed in these experiments is an important result because it emphasizes the significance of quality surgical procedures. Brain implantation of any penetrating electrode is a difficult process; despite this, current scientific research on the impact of initial insertion conditions is limited (Turner et al., 1999; Parlikar and Clement, 2008). For our experiments, we used a stereotactic frame coupled to a high-precision microdrive so that the MEA was inserted vertical to the brain surface at a slow and steady rate of 0.1 $mm \cdot s^{-1}$. The tapered MEA design, rigidity of the ceramic material may have contributed to reducing tissue damage (Polikov, Tresco and Reichert, 2003). We also removed dura overlying the brain surface, which minimizes dimpling of the brain surface during insertion (Szarowski et al., 2003). Lastly, non-steroidal inflammatory drugs were administered to minimize pre-operative stress and alleviate post-operative inflammation at the surgery site. Animal recovery was also aided by providing a soft food diet and saline injections (for dehydration) as needed.

6.4.2 Hippocampal Tissue Response to Chronic MEAs Demonstrates Overlapping Acute and Chronic Phases

Microglia appear to accumulate around the MEA track as early as day 1 post -implantation, verified by the increased Iba1 staining seen in this region. Interestingly, this was not reflected by mean intensity levels, which were lower than control values. A possible explanation is the migration of existing microglial cells to the track from surrounding tissue rather than production of new cells (Szarowski et al., 2003). The loss of processes during activation of stellate-shaped unreactive microglia to amoeboid, reactive microglia to this transformation may also account for the apparent decrease in Iba1 staining (for review, see Polikov, Tresco and Reichert, 2003).

Iba1 levels were significantly higher than control between 1 and 8 weeks ($p<0.001$ and $p<0.05$), but diminished at later time points. Similar changes in microglial distribution have been reported in response to electrode insertion though not at the same time points (Stensaas and Stensaas, 1976; Turner et al., 1999b; Szarowski et al., 2003; Biran et al., 2005). Since hemorrhaging debris was absent beyond 8 weeks in cresyl violet stained sections and Iba1 immunoreactivity was diffuse at 4 and 6 months, it appears that microglia are activated in response to insertion related damage and remain in place until products from disrupted tissue and vasculature are removed from the extracellular matrix. At the same time, Iba1 intensity did not return to control levels. This low level, persistent response has been attributed to the continued presence of the electrode in the brain (Yuen and Agnew, 1995; Rousche et al., 2001; Csicsvari et al., 2003; Biran et al., 2005). These results support the prevailing view that the microglia response to injury is characterized by distinct acute and chronic phases (for review, see Polikov, Reichert and Tresco, 2003).

Knowledge about the time course and spatial extent of the microglial reaction is important because activated microglia are known to secrete both neuroprotective and neurotoxic substances (Elkabes et al., 1996; Nakajima et al., 2001; Giulian et al., 1993a, b) which may either prevent extension of dendrites to the MEA or induce neuronal death. Microglia also produce chemicals that recruit additional microglial to the injury site and upregulate the proliferation of this cell type (Elkabes et al., 1996). Because of these extracellular effects, microglia can act as a chemical barrier to electrode-neuron communication if their range of diffusion overlaps with the recording zone of our MEAs (Tresco et al., 2000). Finally, activated microglia can serve as an indirect physical barrier because they promote the formation of a glial scar that encapsulates the injury site (Tresco et al., 2000).

In the present experiments, average GFAP levels were elevated in implanted hippocampal tissue within 1 day. These levels continued to rise and became significant at one week though aggregation of GFAP positive cells or reactive astrocyte morphology was not discernible around the implant cavity. Mean density levels remained significantly high at 8 weeks but maximum GFAP intensity was concentrated near the track. Increased staining was clearly due to a well-developed sheath of reactive astrocytes, which extended 100 µm into surrounding tissue and must have formed several weeks earlier. Diminished intensity levels beyond 4 months is probably associated with contraction of both astrocyte processes and the sheath itself, which now only extended to 50 µm away from the cavity.

Similar to microglial cells, the rapid upregulation of reactive astrocytes and their subsequent accumulation in the cellular sheath within a few weeks presents several challenges to recording longevity. Neuron growth and repair is an extremely slow process; therefore it takes several days for neurons to form proper connections with the recording sites. Because of this, even a thin, well-developed gliotic scar is an effective physical and electrical insulator that shields the electrode from the rest of the brain (Nathaniel and Nathaniel, 1981; Landis, 1994). With respect to glutamate measurements, the glial scar presents an additional impediment because increased astrocyte density can alter glutamate clearance mechanisms. The glutamate transport capacity of reactive astrocytes is unknown. Accordingly, future neurochemical studies will need to be extended for longer times. It is also important to investigate alterations in the distribution of neurons and their processes around the chronic MEA over time.

6.4.3 Tissue Responses to Chronic MEAs is Different in the PFC and Hippocampus

We have previously investigated the brain tissue reaction to MEAs implanted in the PFC of Long Evans rats (Hascup et al., 2009). In the PFC, the cellular sheath surrounding the implant track was contained within 50-100 µm of the inner track surface at all time points. A similar result was observed with hippocampal implants in the present study supporting that the volume of tissue responding to the MEA is similar in both regions (Figure 6.9). With respect to control tissue, PFC levels of GFAP were increased 4 fold (Control: 3.77 ± 0.77; 1 Week = 16.15 ± 6.6) whereas hippocampal GFAP levels were increased 2 – 3 fold (Control: 13.49 ± 1.0, 1 week = 33.82 ± 6.5). However, comparison of GFAP intensities at common time points showed that total astrocyte levels were approximately two fold higher in the hippocampus ($GFAP_{Hippocampus}$ / $GFAP_{PFC}$: Day 3 = 2.18; Day 7 = 2.09; Month 6 = 1.86). These results suggest that relative change from control was greater in the PFC but absolute numbers were higher in the hippocampus. The most straightforward explanation for this discrepancy is that the hippocampus contains more astrocytes than the PFC (Danbolt, 2001). Further, the studies were carried out in different rat strains and may account for differences in total astrocytes numbers (Gosselin et al., 2008), though actual data from previous research is limited. It is possible that increased astrocyte numbers lead to an enhanced repair response in the hippocampus. Alternately, the cellular and molecular composition of the two regions may be different, possibly affecting wound response and repair.

Differences in experimental design can also lead to different results. The PFC study used MEAs coated with Nafion® while the present study used bare MEAs. Ceramic alumina is inherently hydrophilic, has high porosity and high wettability (Coors Manual S1785), all of which limit astrocyte adhesion (Biran et al., 2005). This is supported by the present SEM and immunohistochemical data. Our ceramic MEAs also have low nanoscale roughness (Chapter Four). Unlike ceramic, Nafion® has dual hydrophilic-hydrophobic properties and studies on the biocompatibility of Nafion and other polysulphonated polymers are contradictory. Leung et al (2008) showed that Nafion coatings increase adhesion of microglia to hydrophobic surfaces. In contrast, Turner and colleagues (1990, 1991) demonstrated a minimal tissue response to intraperitoneal and intravenous nafion membrane implants. Clearly, additional studies on the brain biocompatibility of Nafion are needed.

Finally, the MEA used in the present studies were implanted along with the complete chronic assembly to approximate the actual weight of probes used in recording experiments. The PFC implants only consisted of a microelectrode tip held in place by dental cement (Hascup et al., 2009). The added weight may contribute to increased internal pressure around the implant, potentially causing greater damage *in vivo* (for review, see Polikov, Reichert and Tresco, 2003). Comparison of Iba1 levels showed that control microglial levels are similar in both regions. In the hippocampus staining levels were moderately higher than PFC at the same time points, but these data were not significant.

6.4.4 Chronic MEAs Produce Minimal Tissue Damage in the Rat Hippocampus

The study by Hascup et al also evaluated the tissue effects of chronically implanted microdialysis probes. Microdialysis has traditionally been the gold standard for *in vivo* neurochemistry measurement; therefore a direct comparison of long term tissue effects is important to understand performance differences between this technique and our microelectrode technology. Approximately 1 week after implantation, non-dialysized probes produced tissue reactions extending to 300 µm in the rat prefrontal cortex investigated by Immunohistochemical staining. Other studies based on electron microscopy, voltammetry and fluorescent staining have described a range of distances for acute tissue injury, extending from 300 µm to 1.4 mm (Clap-Lilly et al., 1999; Borland et al., 2005; Mitala et al., 2008; Jaquins-Gerstl and Michael, 2009). Together with the results of the present study, we can state with confidence that our MEA technology causes minimal tissue damage relative to chronic microdialysis probes.

Based on a review of scientific literature, neuronal recording devices such as silicon shank electrodes and platinum or titanium wire electrodes appear to produce greater insertion injury than our MEAs (Turner et al., 1999; Szarowski et al., 2003). It is important to note that these devices are geometrically narrower than our ceramic MEAs (6-12 µm), yet they produced cellular sheaths extending 500-600 µm into external tissue. Though factors such as probe shape (Nicolelis et al., 2003), texture (Rousche et al., 2001) and insertion conditions (Szarowski et al., 2003) are expected to impact implant biocompatibility, recent studies have shown that these factors do not affect the chronic tissue response (12 weeks after implantation) (Szarowski et al., 2003). These data can lead to the assumption that the acute response is not as important as the long term effects. However, theoretical modeling and direct measurements support that the maximum distance between an electrode and a neuron soma must be of the order of cell dimensions to maintain recording performance (Mountcastle, 1957; Rall, 1962; Rosenthal, 1972; Henze et al., 2000). This distance is directly dependent upon the initial tissue reaction because it affects neuronal survival near the probe (Shain et al., 2002). Thus, for indwelling devices like our MEAs, it is important to also evaluate biocompatibility from a functional perspective, i.e., long term recording capability.

The most important finding in support of this hypothesis comes from chronic electrophysiological recordings using our MEAs. We have successfully recorded single unit neuronal activity in the unanesthetized rat hippocampus up to six months (unpublished data by S. Deadwyler and R. Hampson). In this study, hippocampal single-unit neuronal recordings were conducted in rats in conjunction with behavioral measurements, also known as place field measurements (Figure 6.10). Briefly, the Pt sites measured electrical activity of individual pyramidal neurons (place cells) in the hippocampus while the animal explored its environment. Since each neuron has a unique electrical signature, the identity of the neuron can determined by correlating individual firing rates with a range of spatial locations (place fields) in the animal's environment (principal component analysis). Using this technique, neuronal processing of hippocampal dependent learning and memory events can be investigated. One month following implantation, discrete neuronal activity was measured on all Pt sites, and place fields were generated within thirty minutes of placing an animal in a novel environment (Figure 6.10). Similar single unit recordings and place maps could be generated six months later from the same animals. At this time point, the electrical signature measured by the sites was altered (Figure 5.10), suggesting a change in the extracellular environment around the MEA either due to internal movement or due to a change in the properties of the neurons that were recorded. Together, these results unequivocally support the minimal damage caused by our MEAs.

Copyright © Pooja Mahendra Talauliker 2010

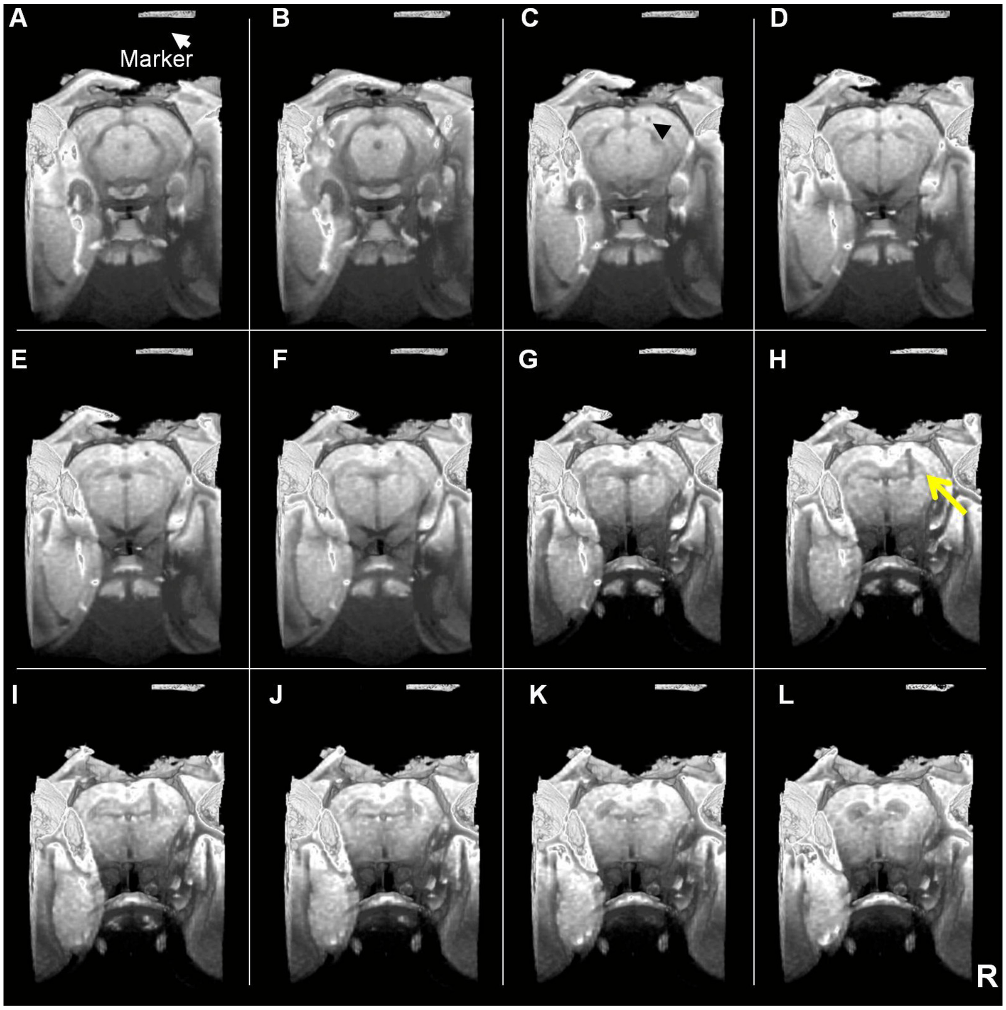

Figure 6.1: T_1-weighted magnetic resonance imaging of the brain-MEA interface. Images are shown in serial coronal sections (500 μm thickness). A water-filled capillary tube is used to mark the implanted hemisphere (white arrow in image A). Note the diminished contrast at the insertion site indicative of edema or hemorrhaging around the MEA (yellow arrow in Image H). A dark spot noted near the track in sections C-E (black arrow in image C) may be a microhemorrhage in the sagittal plane.

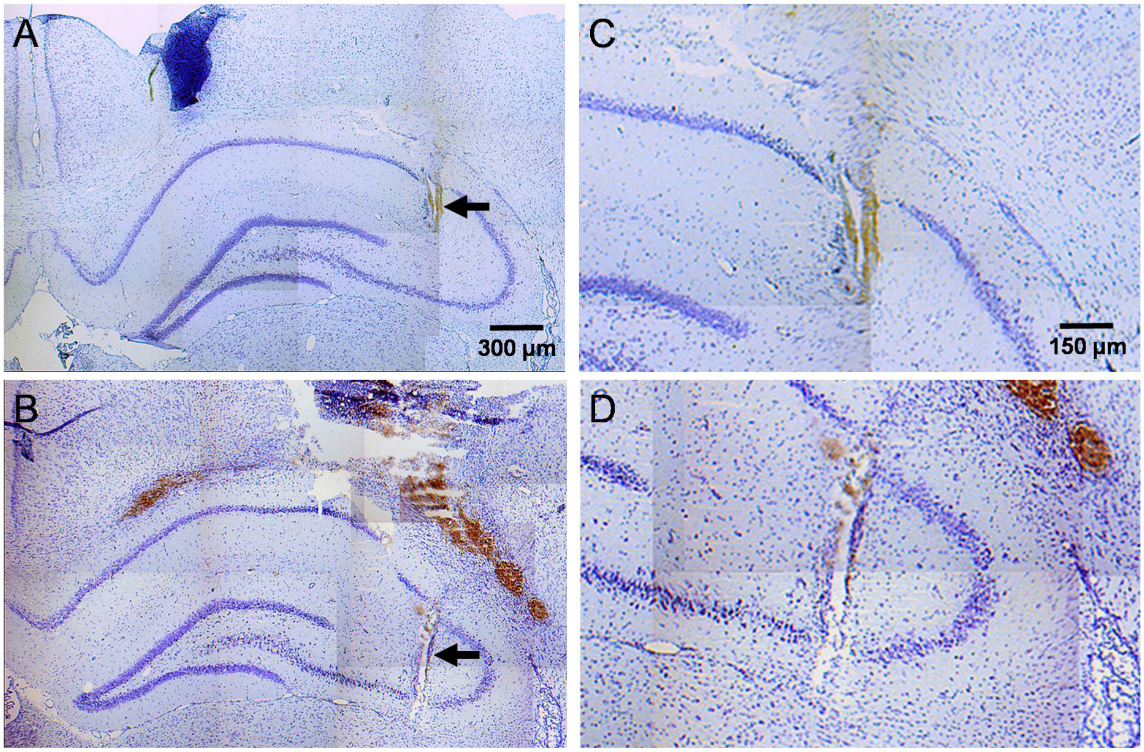

Figure 6.2: Cresyl violet imaging of the MEA track at days 1 and 7. Panels A and C correspond to low and high magnification images of 1 day implants. Panels B and D correspond to low and high magnification images of 1 week implants. Brown staining in tissue sections is debris from hemorrhaging. Arrows indicate well-defined tracks at all time points. Scale A, B: 300 µm, Scale C, D: 150 µm.

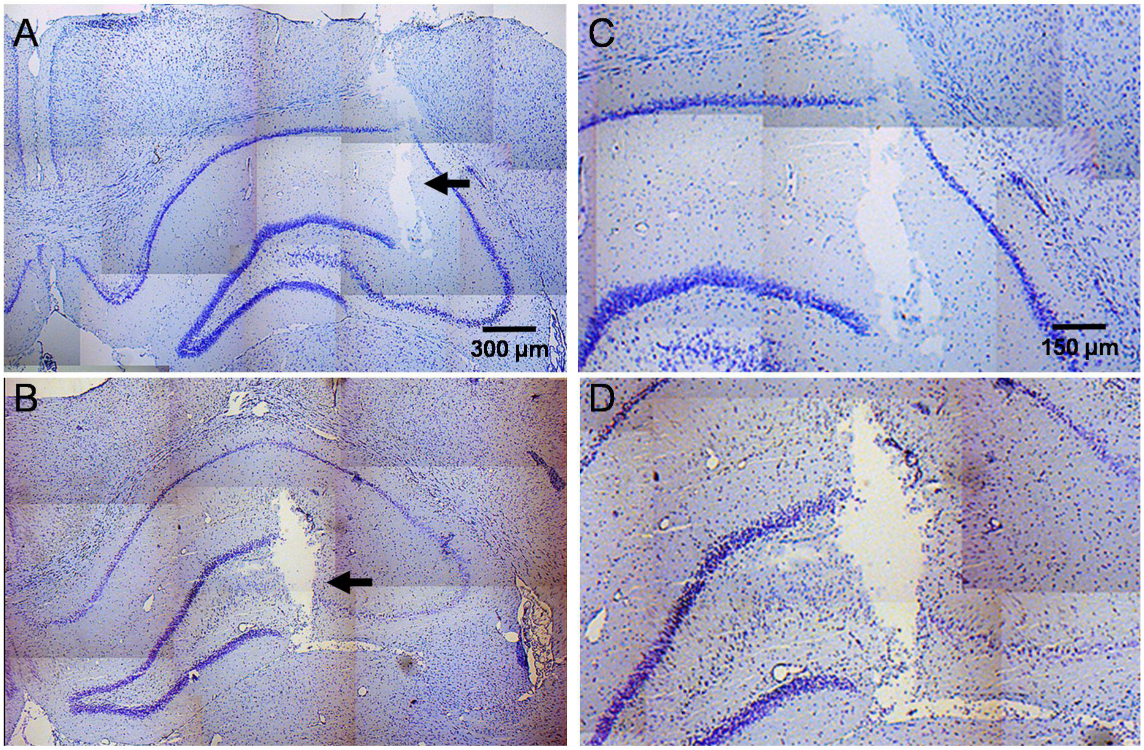

Figure 6.3: Cresyl violet imaging of microelectrode track at weeks 8 and 16. Panels A and C correspond to low and high magnification images of 8 week implants. Panels B and D correspond to low and high magnification images of 16 week implants. Arrows indicate tracks that are wider at these time points. Increased staining is not seen around the track. Scale A, B: 300 µm, Scale C, D: 150 µm.

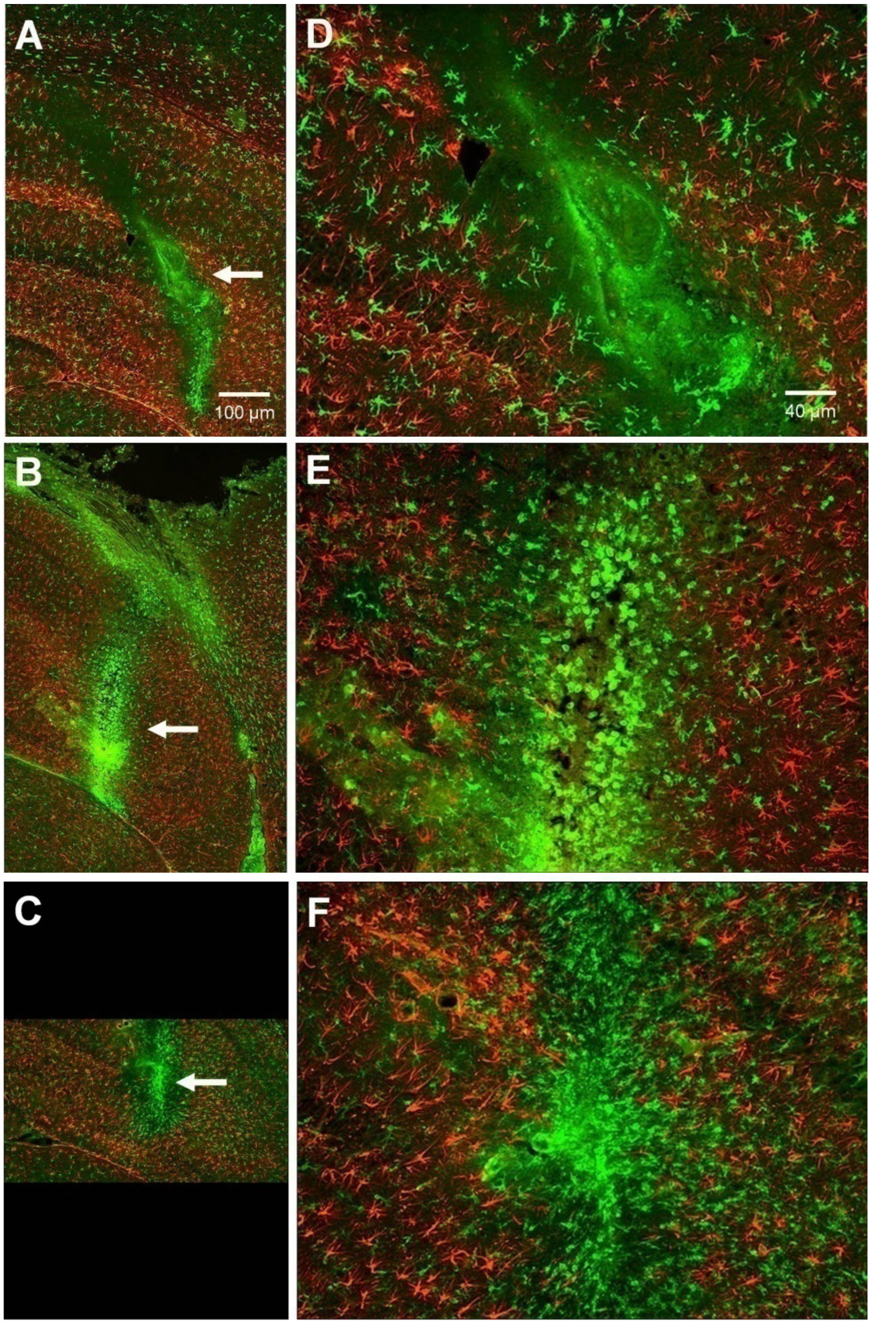

Figure 6.4: Tissue sections colabeled for GFAP and Iba1 at days 1, 3 and 7 after chronic MEA implantation. GFAP (red) and Iba1 (green) labeled tissue shown at day 1 (A, D), day 3 (B. E) and day 7(C, F) after surgery. Iba 1 staining is markedly elevated around the implant track. Scale A-C: 100 µm, Scale D-F: 40 µm. White arrows indicate track location.

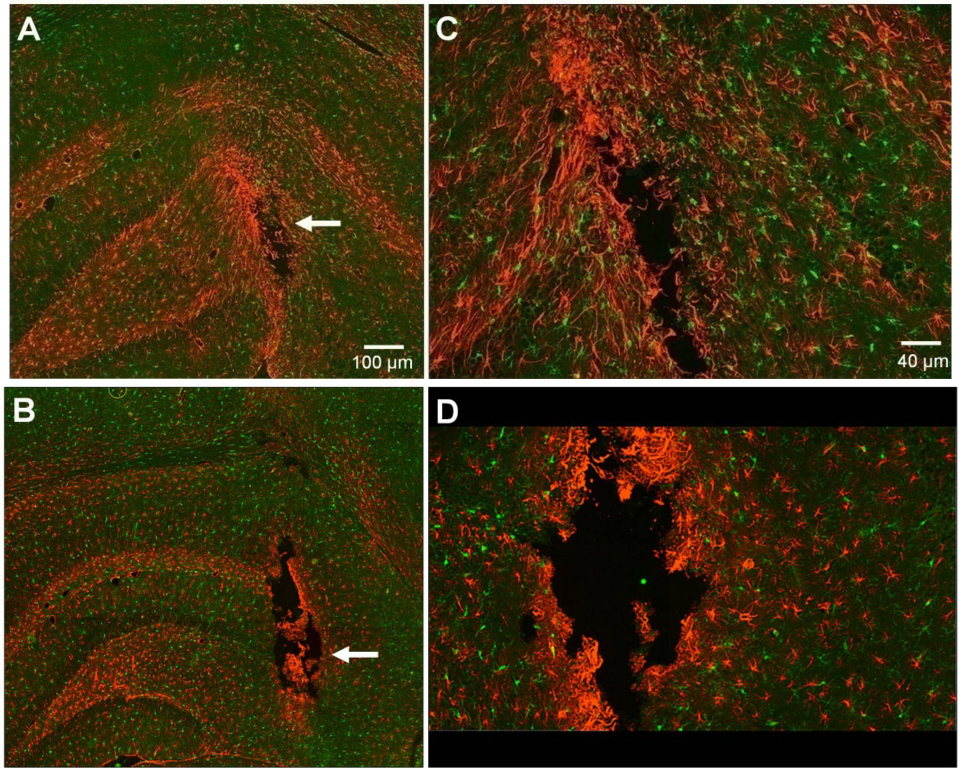

Figure 6.5: Tissue sections colabeled for GFAP and Iba1 at weeks 8 and 16 after chronic MEA implantation. GFAP (red) and Iba1 (green) labeled tissue shown at 8 weeks (A, C) and 16 weeks (B. D) after surgery. A well-defined glial scar is seen at 8 weeks. It becomes contracted and more compact by 4 months. Scale A-C: 100 µm, Scale D-F: 40 µm. White arrows indicate track location.

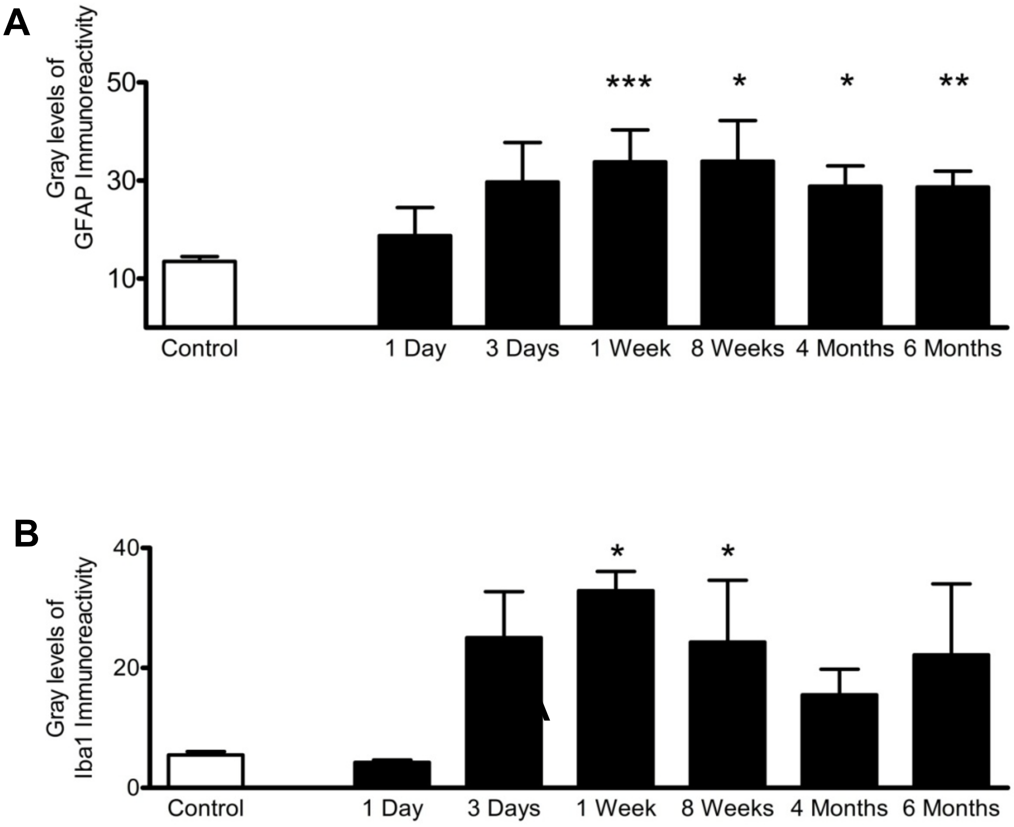

Figure 6.6: Quantitative analysis of mean GFAP and Iba1 immunoreactivity around MEA tracks in the rat hippocampus. Gray levels of GFAP (Panel A) and Iba1 (Panel B) immunoreactivity around the MEA track were compared for time points ranging from 1 day to 6 months following implantation in the rat hippocampus, relative to control tissue. Statistical comparisons were conducted using a One way ANOVA followed by Dunnet's Test. GFAP immunoreactivity was significantly higher by 1 week (33.8 ± 6.8) and remained elevated up to 6 months. Iba1 levels were also significantly elevated by 1 week (32.9 ± 3.2) but diminished after 8 weeks. Significance was defined as *: $p<0.05$, **: $p<0.01$, ***: $p<0.001$

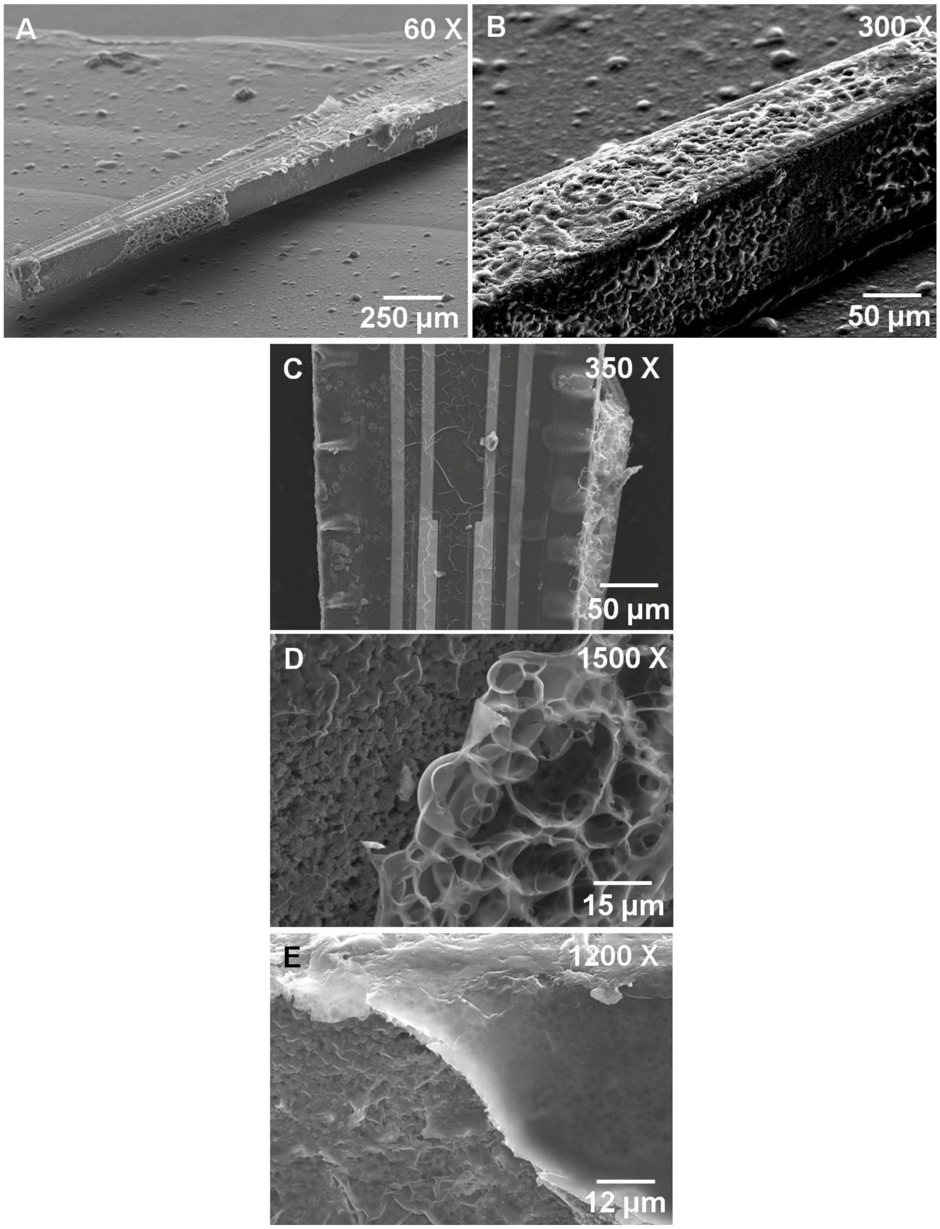

Figure 6.7: Scanning electron micrographs of biological material on MEA samples. The MEAs shown in panels A and B were removed 3 weeks after implantation in the rat hippocampus. Most MEA samples were similar in appearance to Panel A and had very little tissue on the ceramic and Pt surfaces. Only one other MEA resembled panel B and was fully covered with biological material. Panels C and D are high magnification electron micrographs showing tissue debris on the side of the MEA. Panel shows an amorphous cell-free layer that was also found on several MEA samples.

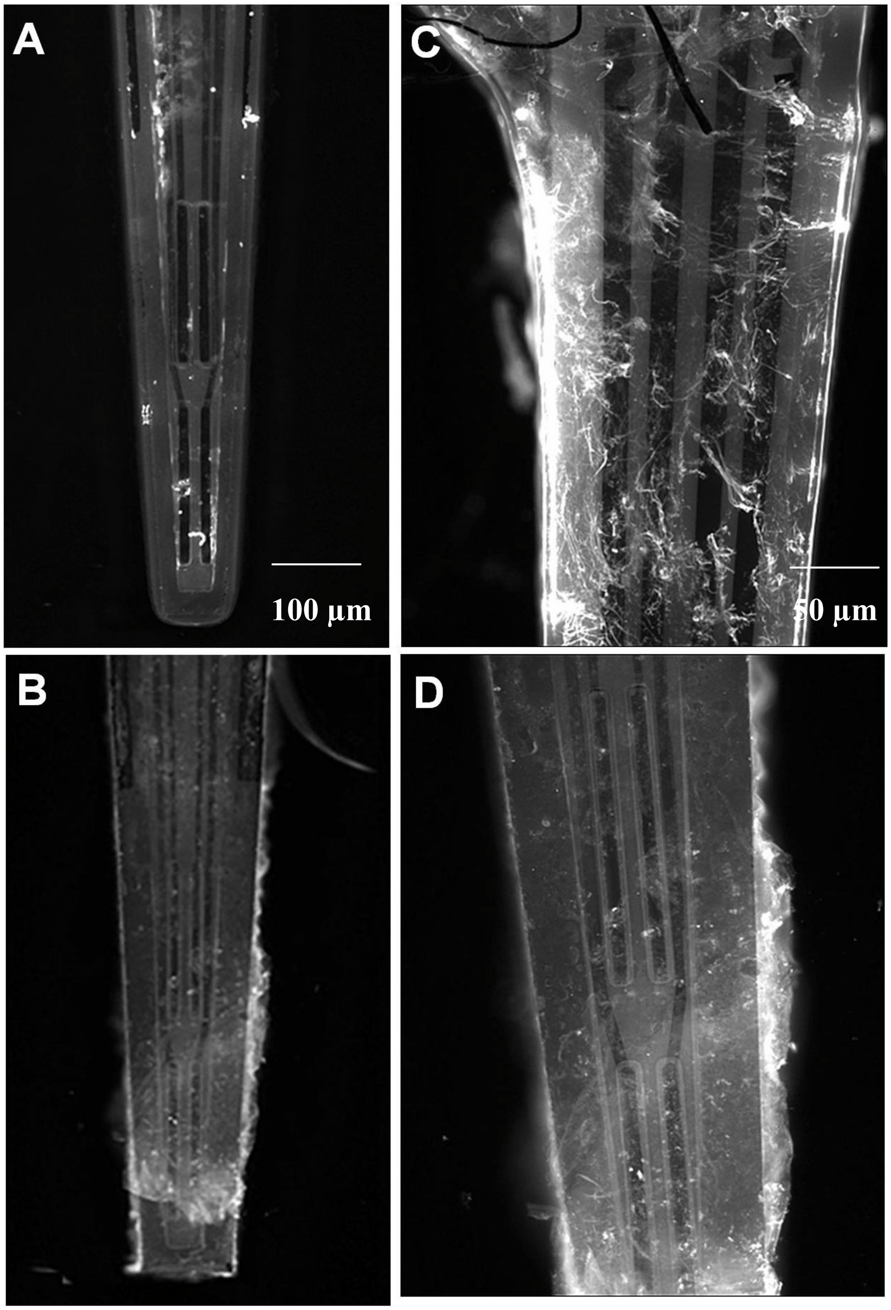

Figure 6.8: GFAP staining of tissue material on MEAs. Panels A and C correspond to low and high magnification images for a microelectrode that showed positive immunoreactivity to GFAP. Panels B and D correspond to a low and high magnification images of typical microelectrode following implantation. GFAP immunoreactivity was not observed. Scale bar: A, C = 100 µm; C, D = 50 µm.

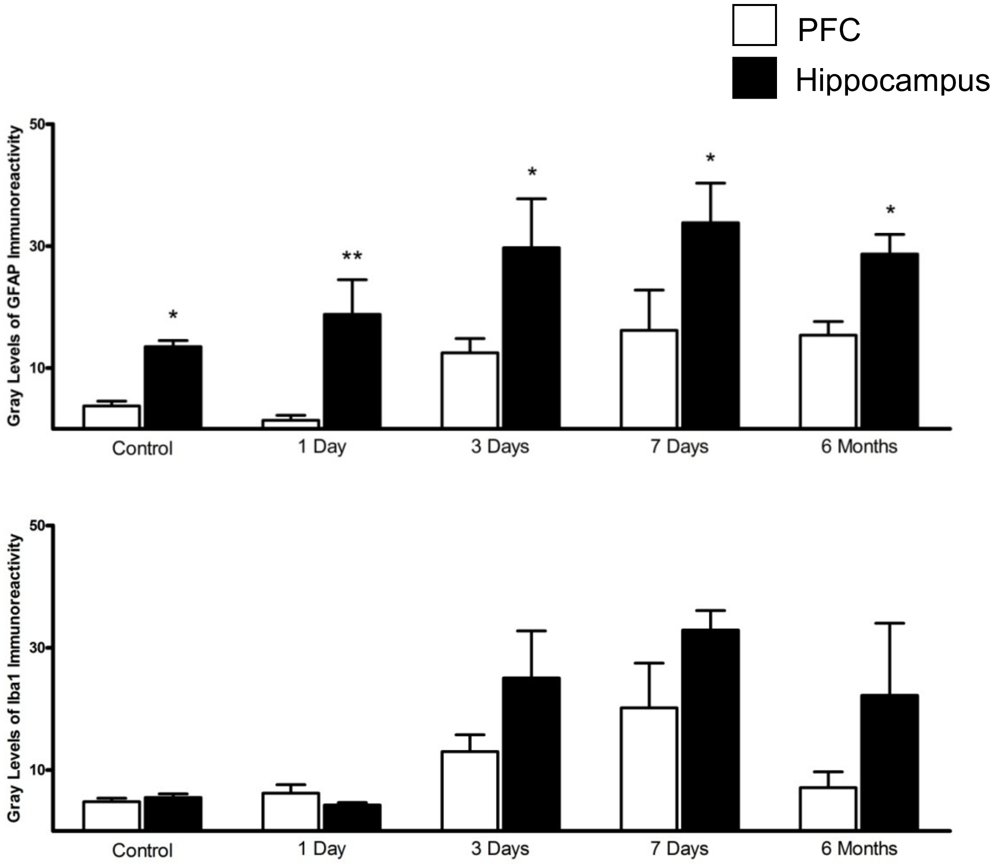

Figure 6.9: Comparison of mean GFAP and Iba1 immunoreactivity around MEA tracks in the PFC of Long Evans rats and hippocampus of F344 rats. Gray levels of GFAP (Panel A) and Iba1 (Panel B) immunoreactivity around the MEA track were compared for time points ranging from 1 day to 6 months following implantation in the hippocampus of F344 rats (black), and in the PFC of Long Evans rats (white) (data courtesy Erin Hascup), relative to respective control tissue samples. Statistical comparisons were conducted using a two way ANOVA followed by Bonferroni's post hoc test. Significance was defined as. *: $p<0.05$.

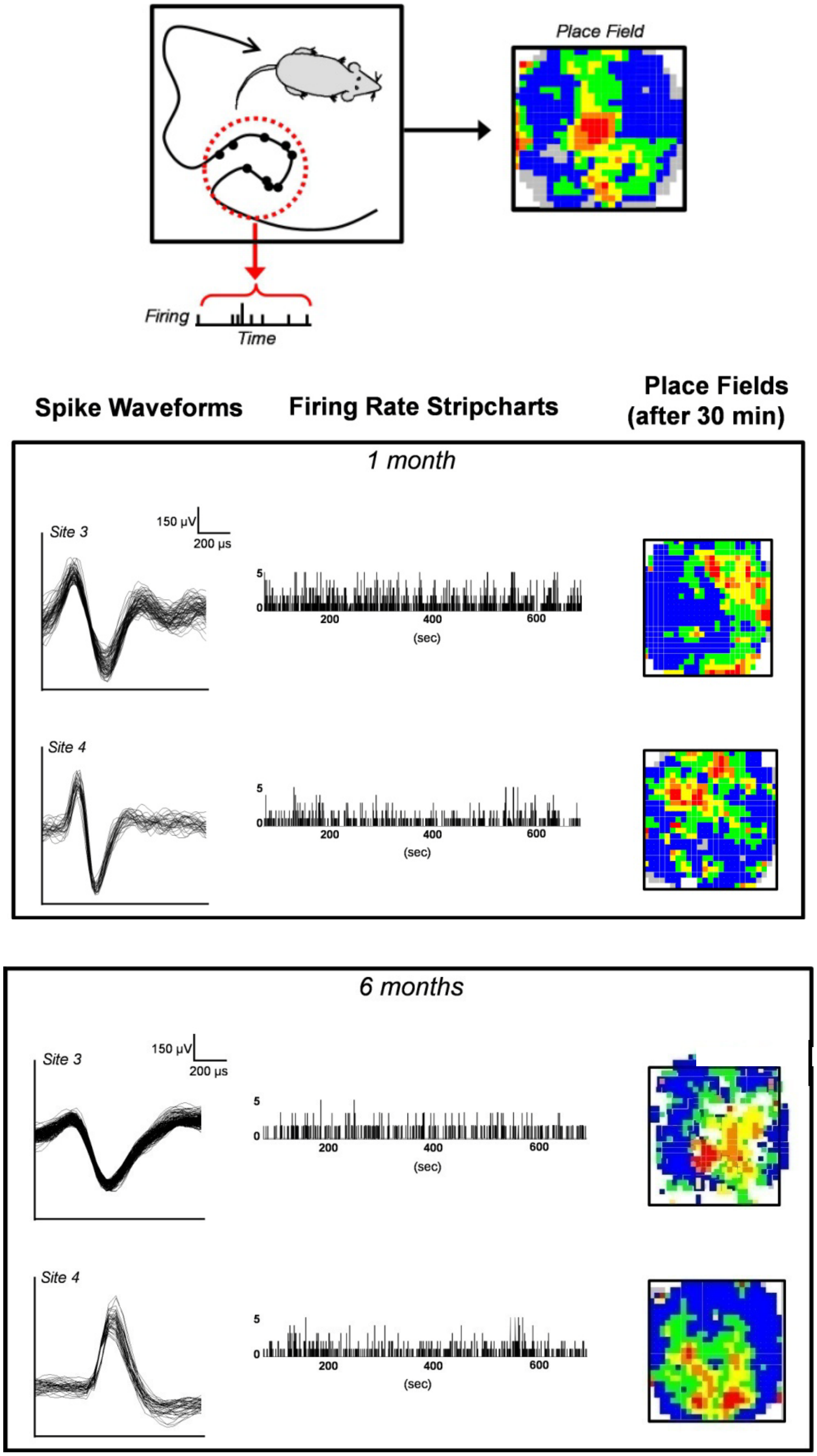

Figure 6.10: Chronic recordings of multiple single-neuron activity in the rat hippocampus using MEAs.

Figure 6.10 (contd.) Place field measurements were obtained in conjunction with hippocampal single unit neuronal recordings from chronically implanted rats. One month following implantation, discrete neuronal activity could be measured on all working sites, and place fields were generated within thirty minutes of placing an animal in a novel environment. Similar single unit recordings and place maps could be generated six months later from the same animals though the electrical signature measured by the sites was different from 1 month recordings. *(Data courtesy Sam Deadwyler and Rob Hampson)*

Conclusions

The studies described in this dissertation showed that the micrometer targeting capability of the novel W4-MEA in conjunction with rapid amperometric recordings is a powerful tool for investigations of *in vivo* glutamate regulation. Potassium stimulation of nerve terminals in discrete hippocampal subregions revealed that release and uptake of evoked glutamate is a fast process (5-10 seconds). Particularly in the DG and CA3, glutamate release appears to be under tight presynaptic control. Dissimilarities in regulation of glutamate observed in these studies have potentially provided direct evidence for distinct subregional roles in hippoampal processing of cognitive information. Though the trisynaptic circuit is widely suggested to be the primary pathway for information relay throughout the hippocampus, neuroscientists have shown that each subregion of the hippocampus is unique with respect to cellular distribution, subcellular content and synaptic connectivity. I believe that future work combining pharmacological investigations with glutamate recordings can elucidate the effect of these differences on the mechanism hippocampal function.

Our anesthetized studies did not include investigations of glutamate regulation during a disease process but are extremely relevant to understanding changes in hippocampal function in neurodegenerative conditions like Alzheimer’s disease. The entorhinal cortex (EC) is the first brain structures to be affected in Alzheimer’s disease (AD). Since perforant path projections from the EC to the DG are the primary excitatory input to the hippocampus, loss of EC axons is expected to affect the terminal end of these projections. However, the CA1 is the first hippocampal substructure to show neurodegenerative changes. Until now, a satisfactory explanation for the progressive loss of excitatory pyramidal neurons has not been available though an indirect excitatory component has been suggested. This hypothesis has received some support in the scientific community because partial blockade of NMDA receptors with low-affinity antagonists like Memantine have been shown to improve cognitive function in Alzheimer’s disease. At the same time, we do not know whether receptor dysregulation is due to changes in afferent inputs from the triysaptic or parallel excitatory projections from the EC through the alvear pathway, perhaps both. Future experiments involving selection deactivation or lesioning of individual pathways followed by real-time glutamate recordings have the potential to provide novel insight about the pathology of AD.

While acute studies can provide a wealth of data about hippocampal glutamatergic circuitry, we recognize that combined studies of glutamate and behavior offer the greatest potential for understanding the functional role of this excitatory neurotransmission. The experiments conducted in this dissertation support our current capability to measure resting glutamate from the CA1 subregion of unanesthetized rats for up to six days. Since resting glutamate was stable over multiple days, a second goal of this dissertation was characterization and optimization of our chronic MEA technology for extended hippocampal recordings in awake, behaving animals as long as six months.

Scanning electron microscopy and atomic force microscopy of Pt sites showed that the ceramic surface of the MEA has an inherent nanoscale roughness. Prior research has shown that this type of surface supports neuronal growth but does not permit astrocyte attachment (Polikov, Tresco and Reichert, 2003). We were able to verify the latter through immunohistochemical studies while collaborative investigations (with Dr. Ingrid Stromberg at the University of Umeá) to study neuronal distribution at the brain-MEA interface are already underway. We also initiated studies to improve our enzyme coating procedure. Presently, enzyme coatings on our MEAs are applied by hand. This method offers limited control over the coating thickness and uniformity both within and between MEAs. The Jetlab® microprinter (Microfab Technologies, Plano, TX) offers the capability to apply picoliter volumes of coating solutions onto discrete Pt sites. With respect to *in vitro* performance, our preliminary results have been extremely promising. We also achieved dual enzyme coatings that allowed for detection of two analytes by the MEA simultaneously. In summary, the studies presented in this dissertation have made several inroads towards our goal of conducting long-term neurotransmitter investigations. Some questions have been answered, at the same time, we are now presented with several exciting opportunities for future investigations.

Appendix: Custom Script for Jetlab Printing Trials

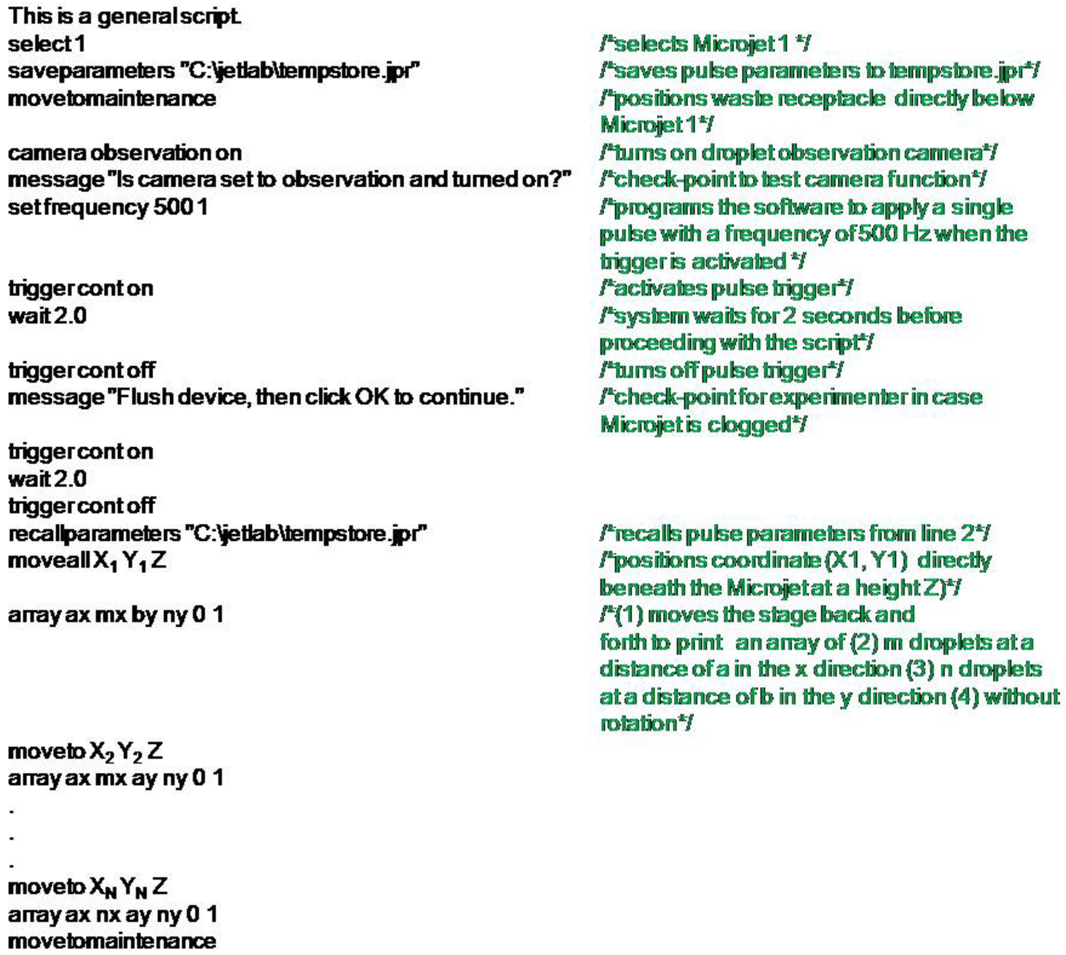

```
This is a general script.
select 1                                                  /*selects Microjet 1 */
saveparameters "C:\jetlab\tempstore.jpr"                  /*saves pulse parameters to tempstore.jpr*/
movetomaintenance                                         /*positions waste receptacle directly below
                                                          Microjet 1*/
camera observation on                                     /*turns on droplet observation camera*/
message "Is camera set to observation and turned on?"     /*check-point to test camera function*/
setfrequency 500 1                                        /*programs the software to apply a single
                                                          pulse with a frequency of 500 Hz when the
                                                          trigger is activated */
triggercont on                                            /*activates pulse trigger*/
wait 2.0                                                  /*system waits for 2 seconds before
                                                          proceeding with the script*/
triggercont off                                           /*turns off pulse trigger*/
message "Flush device, then click OK to continue."        /*check-point for experimenter in case
                                                          Microjet is clogged*/
triggercont on
wait 2.0
triggercont off
recallparameters "C:\jetlab\tempstore.jpr"                /*recalls pulse parameters from line 2*/
moveall X1 Y1 Z                                           /*positions coordinate (X1, Y1) directly
                                                          beneath the Microjet at a height Z)*/
array ax mx by ny 0 1                                     /*(1) moves the stage back and
                                                          forth to print an array of (2) m droplets at a
                                                          distance of a in the x direction (3) n droplets
                                                          at a distance of b in the y direction (4) without
                                                          rotation*/
moveto X2 Y2 Z
array ax mx ay ny 0 1
.
.
.
moveto XN YN Z
array ax nx ay ny 0 1
movetomaintenance
```

Figure A.1: General script that can be customized for jetlab-based enzyme coatings. The Jetlab® system is controlled by its namesake, the Jetlab® software. During a printing trial, the software can recall a custom-coded script that controls droplet formation from the jetting device while simultaneously directing the motion of the translation stages. The script shown above can be modified for a variety of MEA designs and coating solutions. It can also be used to control the motion of multiple jetting devices.

References

Ackl N, Ising M, Schreiber YA, Atiya M, Sonntag A, Auer DP. Hippocampal metabolic abnormalities in mild cognitive impairment and Alzheimer's disease. *Neurosci Lett.* Aug 12-19 2005;384(1-2):23-28.

Albensi BC. The NMDA receptor/ion channel complex: a drug target for modulating synaptic plasticity and excitotoxicity. *Curr Pharm Des.* 2007;13(31):3185-3194.

Alloway KD, Pritchard TC. Medical Neuroscience.Hayes Barton Press; (2007)

Amaral DG, Insausti R, Cowan WM. The commissural connections of the monkey hippocampal formation. *J Comp Neurol.* Apr 10 1984;224(3):307-336.

Amaral DG, Witter MP. The three-dimensional organization of the hippocampal formation: a review of anatomical data. *Neuroscience.* 1989;31(3):571-591.

Andersen P., Morris R., Amaral D., Bliss T., O'Keefe J. The Hippocampus Book. Oxford University Press, New York, New York (2007)

Andersen P, Blackstad TW, Lomo T. Location and identification of excitatory synapses on hippocampal pyramidal cells. *Exp Brain Res.* 1966;1(3):236-248.

Andin J, Hallbeck M, Mohammed AH, Marcusson J. Influence of environmental enrichment on steady-state mRNA levels for EAAC1, AMPA1 and NMDA2A receptor subunits in rat hippocampus. *Brain Res.* Oct 12 2007;1174:18-27.

Angulo MC, Kozlov AS, Charpak S, Audinat E. Glutamate released from glial cells synchronizes neuronal activity in the hippocampus. *J Neurosci.* Aug 4 2004;24(31):6920-6927.

Anwyl R. Metabotropic glutamate receptors: electrophysiological properties and role in plasticity. *Brain Res Brain Res Rev.* Jan 1999;29(1):83-120.

Anwyl R. Metabotropic glutamate receptor-dependent long-term potentiation.

Neuropharmacology. Mar 2009;56(4):735-740.

Araque A, Sanzgiri RP, Parpura V, Haydon PG. Astrocyte-induced modulation of synaptic transmission. *Can J Physiol Pharmacol.* Sep 1999;77(9):699-706.

Armstrong DM, Ikonomovic MD. AMPA-selective glutamate receptor subtype immunoreactivity in the hippocampal dentate gyrus of patients with Alzheimer disease. Evidence for hippocampal plasticity. *Mol Chem Neuropathol.* May-Aug 1996;28(1-3):59-64.

Armstrong DM, Sheffield R, Mishizen-Eberz AJ, et al. Plasticity of glutamate and GABAA receptors in the hippocampus of patients with Alzheimer's disease. *Cell Mol Neurobiol.* Oct 2003;23(4-5):491-505.

Arnold SE, Talbot K, Hahn CG. Neurodevelopment, neuroplasticity, and new genes for schizophrenia. *Prog Brain Res.* 2005;147:319-345.

Ashton D, Van Reempts J, Haseldonckx M, Willems R. Dorsal-ventral gradient in vulnerability of CA1 hippocampus to ischemia: a combined histological and electrophysiological study. *Brain Res.* May 22 1989;487(2):368-372.

Bagley J, Moghaddam B. Temporal dynamics of glutamate efflux in the prefrontal cortex and in the hippocampus following repeated stress: effects of pretreatment with saline or diazepam. *Neuroscience.* Mar 1997;77(1):65-73.

Barnes CA, McNaughton BL. Physiological compensation for loss of afferent synapses in rat hippocampal granule cells during senescence. *J Physiol.* Dec 1980;309:473-485.

Barnes CA, Rao G, Foster TC, McNaughton BL. Region-specific age effects on AMPA sensitivity: electrophysiological evidence for loss of synaptic contacts in hippocampal field CA1. *Hippocampus.* Oct 1992;2(4):457-468.

Baudry M, Lynch G. Remembrance of arguments past: how well is the glutamate receptor hypothesis of LTP holding up after 20 years? *Neurobiol Learn Mem.* Nov 2001;76(3):284-297.

Beal MF, Clevens RA, Chattha GK, MacGarvey UM, Mazurek MF, Gabriel SM. Galanin-like immunoreactivity is unchanged in Alzheimer's disease and

Parkinson's disease dementia cerebral cortex. *J Neurochem.* Dec 1988;51(6):1935-1941.

Beckstrom H, Julsrud L, Haugeto O, et al. Interindividual differences in the levels of the glutamate transporters GLAST and GLT, but no clear correlation with Alzheimer's disease. *J Neurosci Res.* Jan 15 1999;55(2):218-229.

Bellocchio EE, Reimer RJ, Fremeau RT, Jr., Edwards RH. Uptake of glutamate into synaptic vesicles by an inorganic phosphate transporter. *Science.* Aug 11 2000;289(5481):957-960.

Ben-Ari Y. Effects of anoxia and aglycemia on the adult and immature hippocampus. *Biol Neonate.* 1992;62(4):225-230.

Bickford PC, Adams CE, Boyson SJ, et al. Long-term treatment of male F344 rats with deprenyl: assessment of effects on longevity, behavior, and brain function. *Neurobiol Aging.* May-Jun 1997;18(3):309-318.

Biran R, Martin DC, Tresco PA. Neuronal cell loss accompanies the brain tissue response to chronically implanted silicon microelectrode arrays. *Exp Neurol.* Sep 2005;195(1):115-126.

Biran R, Martin DC, Tresco PA. The brain tissue response to implanted silicon microelectrode arrays is increased when the device is tethered to the skull. *J Biomed Mater Res A.* Jul 2007;82(1):169-178.

Biran R, Noble MD, Tresco PA. Characterization of cortical astrocytes on materials of differing surface chemistry. *J Biomed Mater Res.* Aug 1999;46(2):150-159.

Biran R, Noble MD, Tresco PA. Directed nerve outgrowth is enhanced by engineered glial substrates. *Exp Neurol.* Nov 2003;184(1):141-152.

Bliss TV, Collingridge GL. A synaptic model of memory: long-term potentiation in the hippocampus. *Nature.* Jan 7 1993;361(6407):31-39.

Borland LM, Shi G, Yang H, Michael AC. Voltammetric study of extracellular dopamine near microdialysis probes acutely implanted in the striatum of the anesthetized rat. *J Neurosci Methods.* Aug 15 2005;146(2):149-158.

Bortolotto ZA, Nistico R, More JC, Jane DE, Collingridge GL. Kainate receptors and mossy fiber LTP. *Neurotoxicology.* Oct 2005;26(5):769-777.

Boyan BD, Hummert TW, Dean DD, Schwartz Z. Role of material surfaces in regulating bone and cartilage cell response. *Biomaterials.* Jan 1996;17(2):137-146.

Braak H, Braak E. Evolution of neuronal changes in the course of Alzheimer's disease. *J Neural Transm Suppl.* 1998;53:127-140.

Burmeister JJ, Coates TD, Gerhardt GA. Multisite microelectrode arrays for measurements of multiple neurochemicals. *Conf Proc IEEE Eng Med Biol Soc.* 2004;7:5348-5351.

Burmeister JJ, Gerhardt GA. Self-referencing ceramic-based multisite microelectrodes for the detection and elimination of interferences from the measurement of L-glutamate and other analytes. *Anal Chem.* Mar 1 2001;73(5):1037-1042.

Burmeister JJ, Moxon K, Gerhardt GA. Ceramic-based multisite microelectrodes for electrochemical recordings. *Anal Chem.* Jan 1 2000;72(1):187-192.

Burmeister JJ, Palmer M, Gerhardt GA. L-lactate measures in brain tissue with ceramic-based multisite microelectrodes. *Biosens Bioelectron.* Mar 15 2005;20(9):1772-1779.

Burmeister JJ, Pomerleau F, Palmer M, Day BK, Huettl P, Gerhardt GA. Improved ceramic-based multisite microelectrode for rapid measurements of L-glutamate in the CNS. *J Neurosci Methods.* Sep 30 2002;119(2):163-171.

Cass WA, Gerhardt GA, Mayfield RD, Curella P, Zahniser NR. Differences in dopamine clearance and diffusion in rat striatum and nucleus accumbens following systemic cocaine administration. *J Neurochem.* Jul 1992;59(1):259-266.

Cavus I, Kasoff WS, Cassaday MP, et al. Extracellular metabolites in the cortex and hippocampus of epileptic patients. *Ann Neurol.* Feb 2005;57(2):226-235.

Chapman AG, Nanan K, Williams M, Meldrum BS. Anticonvulsant activity of two metabotropic glutamate group I antagonists selective for the mGlu5 receptor: 2-methyl-6-(phenylethynyl)-pyridine (MPEP), and (E)-6-methyl-2-styryl-pyridine (SIB 1893). *Neuropharmacology.* Jul 10 2000;39(9):1567-1574.

Chessell IP, Humphrey PP. Nicotinic and muscarinic receptor-evoked depolarizations recorded from a novel cortical brain slice preparation. *Neuropharmacology.* Oct 1995;34(10):1289-1296.

Clapp-Lilly KL, Roberts RC, Duffy LK, Irons KP, Hu Y, Drew KL. An ultrastructural analysis of tissue surrounding a microdialysis probe. *J Neurosci Methods.* Aug 15 1999;90(2):129-42

Cooley PW*,* Wallace DB, Antohe BV. Proceedings, SPIE Microfluidics and BioMEMS Conference, San Francisco CA, October 22-25, *2001*.

Csicsvari J, Henze DA, Jamieson B, et al. Massively parallel recording of unit and local field potentials with silicon-based electrodes. *J Neurophysiol.* Aug 2003;90(2):1314-1323.

Danbolt NC. Glutamate uptake. *Prog Neurobiol.* Sep 2001;65(1):1-105.

Daoudal G, Hanada Y, Debanne D. Bidirectional plasticity of excitatory postsynaptic potential (EPSP)-spike coupling in CA1 hippocampal pyramidal neurons. *Proc Natl Acad Sci U S A.* Oct 29 2002;99(22):14512-14517.

Day BK, Pomerleau F, Burmeister JJ, Huettl P, Gerhardt GA. Microelectrode array studies of basal and potassium-evoked release of L-glutamate in the anesthetized rat brain. *J Neurochem.* Mar 2006;96(6):1626-1635.

de Groot DM, Bierman EP. A critical evaluation of methods for estimating the numerical density of synapses. *J Neurosci Methods.* Oct 1986;18(1-2):79-101.

de Toledo-Morrell L, Morrell F. Electrophysiological markers of aging and memory loss in rats. *Ann N Y Acad Sci.* 1985;444:296-311.

Del Bigio MR, Becker LE. Microglial aggregation in the dentate gyrus: a marker of mild hypoxic-ischaemic brain insult in human infants. *Neuropathol Appl Neurobiol.* Apr 1994;20(2):144-151.

Diana G, Scotti de Carolis A, Frank C, Domenici MR, Sagratella S. Selective reduction of hippocampal dentate frequency potentiation in aged rats with impaired place learning. *Brain Res Bull.* 1994;35(2):107-111.

Dijk SN, Francis PT, Stratmann GC, Bowen DM. Cholinomimetics increase glutamate outflow via an action on the corticostriatal pathway: implications for Alzheimer's disease. *J Neurochem.* Nov 1995;65(5):2165-2169.

Du DM, Carlier PR. Development of bivalent acetylcholinesterase inhibitors as potential therapeutic drugs for Alzheimer's disease. *Curr Pharm Des.* 2004;10(25):3141-3156.

Duerson K, Woltjer RL, Mookherjee P, et al. Detergent-insoluble EAAC1/EAAT3 aberrantly accumulates in hippocampal neurons of Alzheimer's disease patients. *Brain Pathol.* Apr 2009;19(2):267-278.

Duineveld PC. The stability of ink-jet printed lines of liquid with zero receding contact angle on a homogeneous substrate. *J Fluid Mech.* Feb 25 2003;477:175-200.

During MJ, Spencer DD. Extracellular hippocampal glutamate and spontaneous seizure in the conscious human brain. *Lancet.* Jun 26 1993;341(8861):1607-1610.

Eastwood SL. The synaptic pathology of schizophrenia: is aberrant neurodevelopment and plasticity to blame? *Int Rev Neurobiol.* 2004;59:47-72.

Edwards FA, Konnerth A, Sakmann B. Quantal analysis of inhibitory synaptic transmission in the dentate gyrus of rat hippocampal slices: a patch-clamp study. *J Physiol.* Nov 1990;430:213-249.

Elkabes S, DiCicco-Bloom EM, Black IB. Brain microglia/macrophages express neurotrophins that selectively regulate microglial proliferation and function. *J Neurosci.* Apr 15 1996;16(8):2508-2521.

Flood DG, Coleman PD. Hippocampal plasticity in normal aging and decreased plasticity in Alzheimer's disease. *Prog Brain Res.* 1990;83:435-443.

Fordyce DE, Farrar RP. Enhancement of spatial learning in F344 rats by physical activity and related learning-associated alterations in hippocampal and cortical cholinergic functioning. *Behav Brain Res.* Dec 20 1991;46(2):123-133.

Francis PT. Glutamatergic systems in Alzheimer's disease. *Int J Geriatr Psychiatry.* Sep 2003;18(Suppl 1):S15-21.

Francis PT, Webster MT, Chessell IP, et al. Neurotransmitters and second messengers in aging and Alzheimer's disease. *Ann N Y Acad Sci.* Sep 24 1993;695:19-26.

Freedman R, Goldowitz D. Studies on the hippocampal formation: From basic development to clinical applications: Studies on schizophrenia. *Prog Neurobiol.* Oct 21 2009.

Friedemann MN, Gerhardt GA. Regional effects of aging on dopaminergic function in the Fischer-344 rat. *Neurobiol Aging.* Mar-Apr 1992;13(2):325-332.

Friedemann MN, Gerhardt GA. In vivo electrochemical studies of the dynamic effects of locally applied excitatory amino acids in the striatum of the anesthetized rat. *Exp Neurol.* Mar 1996;138(1):53-63.

Gagne J, Gelinas S, Martinoli MG, et al. AMPA receptor properties in adult rat hippocampus following environmental enrichment. *Brain Res.* Jul 13 1998;799(1):16-25.

Gallagher M, Nicolle MM. Animal models of normal aging: relationship between cognitive decline and markers in hippocampal circuitry. *Behav Brain Res.* Nov 30 1993;57(2):155-162.

Gegelashvili G and Schousboe A. Cellular distribution and kinetic properties of high-affinity glutamate transporters. *Brain Res Bull*. 2003, 45(3):233-8. Review.

Giovannini MG, Camilli F, Mundula A, Pepeu G. Glutamatergic regulation of acetylcholine output in different brain regions: a microdialysis study in the rat. *Neurochem Int.* Jul 1994;25(1):23-26.

Giulian D. Reactive glia as rivals in regulating neuronal survival. *Glia.* Jan 1993;7(1):102-110.

Giulian D, Corpuz M. Microglial secretion products and their impact on the nervous system. *Adv Neurol.* 1993;59:315-320.

Gosselin RD, Gibney S, O'Malley D, Dinan TG, Cryan JF. Region specific decrease in glial fibrillary acidic protein immunoreactivity in the brain of a rat model of depression. *Neuroscience.* Mar 17 2009;159(2):915-925.

Gottlieb DI, Cowan WM. Autoradiographic studies of the commissural and ipsilateral association connection of the hippocampus and detentate gyrus of the rat. I. The commissural connections. *J Comp Neurol.* Jun 15 1973;149(4):393-422.

Greenamyre JT, Maragos WF. Neurotransmitter receptors in Alzheimer disease. *Cerebrovasc Brain Metab Rev.* Summer 1993;5(2):61-94.

Greenamyre JT, Young AB. Excitatory amino acids and Alzheimer's disease. *Neurobiol Aging.* Sep-Oct 1989;10(5):593-602.

Greene JG, Borges K, Dingledine R. Quantitative transcriptional neuroanatomy of the rat hippocampus: evidence for wide-ranging, pathway-specific heterogeneity among three principal cell layers. *Hippocampus.* Mar 2009;19(3):253-264.

Hall SB, Khudaish EA, Hart AL. Electrochemical oxidation of hydrogen peroxide at platinum electrodes. Part IV: phosphate buffer dependence. *Electrochim Acta.* 1999;44(25):4573-4582.

Hascup ER, af Bjerken S, Hascup KN, et al. Histological studies of the effects of chronic implantation of ceramic-based microelectrode arrays and microdialysis probes in rat prefrontal cortex. *Brain Res.* Sep 29 2009;1291:12-20.

Hascup KN, Hascup ER, Pomerleau F, Huettl P, Gerhardt GA. Second-by-second measures of L-glutamate in the prefrontal cortex and striatum of freely moving mice. *J Pharmacol Exp Ther.* Feb 2008;324(2):725-731.

Hascup KN, Rutherford EC, Quintero JE, Day BK, Nickell JR, Pomerleau FP, Huettl P, Burmeister JJ, Gerhardt GA. Second-by-second measures of L-glutamate and other neurotransmitters using enzyme-based microelectrode arrays, in: Electrochemical Methods for Neuroscience. Michael A.C. and Borland L.M. (Eds.), CRC Press, Boca Raton, FL, 2007, pp. 407-450.

Hattiangady B, Rao MS, Shetty AK. Chronic temporal lobe epilepsy is associated with severely declined dentate neurogenesis in the adult hippocampus. *Neurobiol Dis.* Dec 2004;17(3):473-490.

Haugeto O, Ullensvang K, Levy LM, et al. Brain glutamate transporter proteins form homomultimers. *J Biol Chem.* Nov 1 1996;271(44):27715-27722.

Henze DA, Borhegyi Z, Csicsvari J, Mamiya A, Harris KD, Buzsaki G. Intracellular features predicted by extracellular recordings in the hippocampus in vivo. *J Neurophysiol.* Jul 2000;84(1):390-400.

Hjelmstad GO, Nicoll RA, Malenka RC. Synaptic refractory period provides a measure of probability of release in the hippocampus. *Neuron.* Dec 1997;19(6):1309-1318.

Holopainen I, Malminen O, Kontro P. Sodium-dependent high-affinity uptake of taurine in cultured cerebellar granule cells and astrocytes. *J Neurosci Res.* 1987;18(3):479-483.

Hu Y, Mitchell KM, Albahadily FN, Michaelis EK, Wilson GS. Direct measurement of glutamate release in the brain using a dual enzyme-based electrochemical sensor. *Brain Res.* Oct 3 1994;659(1-2):117-125.

Hulbert SF, Klawitte.Jj, Bowman LS. History of Ceramic Orthopedic Implants. *Mater Res Bull.* 1972;7(11):1239-&.

Hyman BT, Van Hoesen GW, Damasio AR. Alzheimer's disease: glutamate depletion in the hippocampal perforant pathway zone. *Ann Neurol.* Jul 1987;22(1):37-40.

Ishizuka N, Weber J, Amaral DG. Organization of intrahippocampal projections originating from CA3 pyramidal cells in the rat. *J Comp Neurol.* May 22

1990;295(4):580-623.

Jaquins-Gerstl A, Michael AC. Comparison of the brain penetration injury associated with microdialysis and voltammetry. *J Neurosci Methods.* Oct 15 2009;183(2):127-135.

Jung E, Manessis D, Neumann A, et al. Lamination and laser structuring for a microwell array. *Microsyst Technol.* Jul 2008;14(7):931-936.

Kang M, Trofin L, Mota OM, Martin CR, Analytical Chemistry. September 2005, *77* (19), pp 6243–6249

Karhunen H, Jolkkonen J, Sivenius J, Pitkanen A. Epileptogenesis after experimental focal cerebral ischemia. *Neurochem Res.* Dec 2005;30(12):1529-1542.

Keller EA, Borghese CM, Carrer HF, Ramirez OA. The learning capacity of high or low performance rats is related to the hippocampus NMDA receptors. *Brain Res.* Mar 27 1992;576(1):162-164.

Keller JN. Interplay between oxidative damage, protein synthesis, and protein degradation in Alzheimer's disease. *J Biomed Biotechnol.* 2006;2006(3):12129.

Kemp N, Bashir ZI. Induction of LTD in the adult hippocampus by the synaptic activation of AMPA/kainate and metabotropic glutamate receptors. *Neuropharmacology.* Apr 1999;38(4):495-504.

Kennedy RT, Watson CJ, Haskins WE, Powell DH, Strecker RE. In vivo neurochemical monitoring by microdialysis and capillary separations. *Curr Opin Chem Biol.* Oct 2002;6(5):659-665.

Kerwin RW, Patel S, Meldrum BS, Czudek C, Reynolds GP. Asymmetrical loss of glutamate receptor subtype in left hippocampus in schizophrenia. *Lancet.* Mar 12 1988;1(8585):583-584.

Kesner RP, Hopkins RO. Mnemonic functions of the hippocampus: a comparison between animals and humans. *Biol Psychol.* Jul 2006;73(1):3-18.

Kew JN, Koester A, Moreau JL, et al. Functional consequences of reduction in

NMDA receptor glycine affinity in mice carrying targeted point mutations in the glycine binding site. *J Neurosci.* Jun 1 2000;20(11):4037-4049.

Kiang-Ulrich M, Horvath SM. Age-related metabolic modifications in male F344 rats. *Exp Aging Res.* Summer 1984;10(2):89-93.

Kilbride J, Huang LQ, Rowan MJ, Anwyl R. Presynaptic inhibitory action of the group II metabotropic glutamate receptor agonists, LY354740 and DCG-IV. *Eur J Pharmacol.* Sep 4 1998;356(2-3):149-157.

Kinney GA, Overstreet LS, Slater NT. Prolonged physiological entrapment of glutamate in the synaptic cleft of cerebellar unipolar brush cells. *J Neurophysiol.* Sep 1997;78(3):1320-1333.

Klausnitzer J, Kulla A, Manahan-Vaughan D. Role of the group III metabotropic glutamate receptor in LTP, depotentiation and LTD in dentate gyrus of freely moving rats. *Neuropharmacology.* Feb 2004;46(2):160-170.

Kowall NW, Beal MF. Glutamate-, glutaminase-, and taurine-immunoreactive neurons develop neurofibrillary tangles in Alzheimer's disease. *Ann Neurol.* Feb 1991;29(2):162-167.

Kullmann DM, Erdemli G, Asztely F. LTP of AMPA and NMDA receptor-mediated signals: evidence for presynaptic expression and extrasynaptic glutamate spill-over. *Neuron.* Sep 1996;17(3):461-474.

Kwon HB, Castillo PE. Long-term potentiation selectively expressed by NMDA receptors at hippocampal mossy fiber synapses. *Neuron.* Jan 10 2008;57(1):108-120.

Landfield PW, Rose G, Sandles L, Wohlstadter TC, Lynch G. Patterns of astroglial hypertrophy and neuronal degeneration in the hippocampus of ages, memory-deficient rats. *J Gerontol.* Jan 1977;32(1):3-12.

Landis BJ, Dunn L. Adverse toxic reaction to aqueous procaine penicillin G. *Nurse Pract.* Nov 1984;9(11):36, 41-32, 44.

Leifer D, Kowall NW. Immunohistochemical patterns of selective cellular vulnerability in human cerebral ischemia. *J Neurol Sci.* Nov 1993;119(2):217-228.

Leung BK, Biran R, Underwood CJ, Tresco PA. Characterization of microglial attachment and cytokine release on biomaterials of differing surface chemistry. *Biomaterials.* Aug 2008;29(23):3289-3297.

Li LB, Toan SV, Zelenaia O, et al. Regulation of astrocytic glutamate transporter expression by Akt: evidence for a selective transcriptional effect on the GLT-1/EAAT2 subtype. *J Neurochem.* May 2006;97(3):759-771.

Li XG, Somogyi P, Ylinen A, Buzsaki G. The hippocampal CA3 network: an in vivo intracellular labeling study. *J Comp Neurol.* Jan 8 1994;339(2):181-208.

Lindner MD, Gribkoff VK. Relationship between performance in the Morris water task, visual acuity, and thermoregulatory function in aged F-344 rats. *Behav Brain Res.* Oct 25 1991;45(1):45-55.

Lingane JJ, Anson FC. Amperometry with 2 Platinum Electrodes with the Cuprous-Cupric Bromine-Bromide System. *Analytical Chemistry.* 1956;28(12):1871-1875.

Linnemann D, Skarsfelt T. Regional changes in expression of NCAM, GFAP, and S100 in aging rat brain. *Neurobiol Aging.* Sep-Oct 1994;15(5):651-655.

Lipp OV, Derakshan N. Attentional bias to pictures of fear-relevant animals in a dot probe task. *Emotion.* Sep 2005;5(3):365-369.

Lowe SL, Bowen DM. Glutamic acid concentration in brains of patients with Alzheimer's disease. *Biochem Soc Trans.* Jun 1990;18(3):443-444.

Lupien SJ, McEwen BS, Gunnar MR, Heim C. Effects of stress throughout the lifespan on the brain, behaviour and cognition. *Nat Rev Neurosci.* Jun 2009;10(6):434-445.

Lynch MA. Long-term potentiation and memory. *Physiol Rev.* Jan 2004;84(1):87-136.

Malenka RC, Nicoll RA. NMDA-receptor-dependent synaptic plasticity: multiple forms and mechanisms. *Trends Neurosci.* Dec 1993;16(12):521-527.

Manabe T. [Molecular mechanisms for memory formation]. *Brain Nerve.* Jul

2008;60(7):707-715.

Mann DM, Yates PO, Marcyniuk B. A comparison of nerve cell loss in cortical and subcortical structures in Alzheimer's disease. *J Neurol Neurosurg Psychiatry.* Mar 1986;49(3):310-312.

Manwaring ME, Biran R, Tresco PA. Characterization of rat meningeal cultures on materials of differing surface chemistry. *Biomaterials.* Dec 2001;22(23):3155-3168.

Martin LJ, Furuta A, Blackstone CD. AMPA receptor protein in developing rat brain: glutamate receptor-1 expression and localization change at regional, cellular, and subcellular levels with maturation. *Neuroscience.* Apr 1998;83(3):917-928.

Martinez-Serrano A, Borner C, Pereira R, Villalba M, Satrustegui J. Modulation of presynaptic calcium homeostasis by nitric oxide. *Cell Calcium.* Sep 1996;20(3):293-302.

Massieu L, Tapia R. Glutamate uptake impairment and neuronal damage in young and aged rats in vivo. *J Neurochem.* Sep 1997;69(3):1151-1160.

Mattson MP, Guthrie PB, Kater SB. Intracellular messengers in the generation and degeneration of hippocampal neuroarchitecture. *J Neurosci Res.* Oct-Dec 1988;21(2-4):447-464.

Mattson MP, Lee RE, Adams ME, Guthrie PB, Kater SB. Interactions between entorhinal axons and target hippocampal neurons: a role for glutamate in the development of hippocampal circuitry. *Neuron.* Nov 1988;1(9):865-876.

Mehraein P, Yamada M, Tarnowska-Dziduszko E. Quantitative study on dendrites and dendritic spines in Alzheimer's disease and senile dementia. *Adv Neurol.* 1975;12:453-458.

Meldrum BS. Glutamate as a neurotransmitter in the brain: review of physiology and pathology. *J Nutr.* Apr 2000;130(4S Suppl):1007S-1015S.

Meldrum BS. Why and when are seizures bad for the brain? *Trends Pharmacol Sci.* Sep 2001;22(9):445-446.

Michaelis T, de Biurrun G, Watanabe T, Frahm J, Ohl F, Fuchs E. Gender-specific alterations of cerebral metabolites with aging and cortisol treatment. *J Psychiatr Res.* Jul-Aug 2001;35(4):231-237.

Miele M, Berners M, Boutelle MG, Kusakabe H, Fillenz M. The determination of the extracellular concentration of brain glutamate using quantitative microdialysis. *Brain Res.* Jan 22 1996;707(1):131-133.

Miller DD, Arndt S, Andreasen NC. Alogia, attentional impairment, and inappropriate affect: their status in the dimensions of schizophrenia. *Compr Psychiatry.* Jul-Aug 1993;34(4):221-226.

Mitala CM, Wang Y, Borland LM, et al. Impact of microdialysis probes on vasculature and dopamine in the rat striatum: a combined fluorescence and voltammetric study. *J Neurosci Methods.* Sep 30 2008;174(2):177-185.

Mockett B, Coussens C, Abraham WC. NMDA receptor-mediated metaplasticity during the induction of long-term depression by low-frequency stimulation. *Eur J Neurosci.* Jun 2002;15(11):1819-1826.

Morris RG. Long-term potentiation and memory. *Philos Trans R Soc Lond B Biol Sci.* Apr 29 2003;358(1432):643-647.

Morrison JH, Hof PR. Life and death of neurons in the aging brain. *Science.* Oct 17 1997;278(5337):412-419.

Moulder KL, Meeks JP, Mennerick S. Homeostatic regulation of glutamate release in response to depolarization. *Mol Neurobiol.* Apr 2006;33(2):133-153.

Moulder KL, Mennerick S. Synaptic vesicles: turning reluctance into action. *Neuroscientist.* Feb 2006;12(1):11-15.

Mountcastle VB, Davies PW, Berman AL. Response properties of neurons of cat's somatic sensory cortex to peripheral stimuli. *J Neurophysiol.* Jul 1957;20(4):374-407.

Nagahara AH, Bernot T, Tuszynski MH. Age-related cognitive deficits in rhesus monkeys mirror human deficits on an automated test battery. *Neurobiol Aging.* Aug 27 2008.

Nakajima K, Kohsaka S. Microglia: activation and their significance in the central nervous system. *J Biochem.* Aug 2001;130(2):169-175.

Nelson MD, Saykin AJ, Flashman LA, Riordan HJ. Hippocampal volume reduction in schizophrenia as assessed by magnetic resonance imaging: a meta-analytic study. *Arch Gen Psychiatry.* May 1998;55(5):433-440.

Nicholls DG. The glutamatergic nerve terminal. *Eur J Biochem.* Mar 15 1993;212(3):613-631.

Nickell J, Pomerleau F, Allen J, Gerhardt GA. Age-related changes in the dynamics of potassium-evoked L-glutamate release in the striatum of Fischer 344 rats. *J Neural Transm.* Jan 2005;112(1):87-96.

Nickell J, Salvatore MF, Pomerleau F, Apparsundaram S, Gerhardt GA. Reduced plasma membrane surface expression of GLAST mediates decreased glutamate regulation in the aged striatum. *Neurobiol Aging.* Nov 2007;28(11):1737-1748.

Norris CM, Korol DL, Foster TC. Increased susceptibility to induction of long-term depression and long-term potentiation reversal during aging. *J Neurosci.* Sep 1 1996;16(17):5382-5392.

Ohnuma T, Kato H, Arai H, Faull RL, McKenna PJ, Emson PC. Gene expression of PSD95 in prefrontal cortex and hippocampus in schizophrenia. *Neuroreport.* Sep 28 2000;11(14):3133-3137.

Opris I, Hampson RE, Deadwyler SA. The encoding of cocaine vs. natural rewards in the striatum of nonhuman primates: categories with different activations. *Neuroscience.* Sep 29 2009;163(1):40-54.

Ozden M, Ekinci E, Karagozler AE. Electrochemical synthesis and optimization of poly(4-methoxyphenol) film as a sensor material. *J Appl Polym Sci.* Jun 20 1998;68(12):1941-1947.

Paralikar KJ and Clement RS. Collagenase-Aided Intracortical Microelectrode Array Insertion: Effects on Insertion Force and Recording Performance.

IEEE Transaction on Biomedical Engineering.2008, 55(9):2258-67.

Piedras-Renteria ES, Pyle JL, Diehn M, et al. Presynaptic homeostasis at CNS nerve terminals compensates for lack of a key Ca2+ entry pathway. *Proc Natl Acad Sci U S A.* Mar 9 2004;101(10):3609-3614.

Polikov VS, Tresco PA, Reichert WM. Response of brain tissue to chronically implanted neural electrodes. *J Neurosci Methods.* Oct 15 2005;148(1):1-18.

Pomerleau F, Day BK, Huettl P, Burmeister JJ, Gerhardt GA. Real time in vivo measures of L-glutamate in the rat central nervous system using ceramic-based multisite microelectrode arrays. *Ann N Y Acad Sci.* Nov 2003;1003:454-457.

Potier B, Lamour Y, Dutar P. Age-related alterations in the properties of hippocampal pyramidal neurons among rat strains. *Neurobiol Aging.* Jan-Feb 1993;14(1):17-25.

Potier B, Rascol O, Jazat F, Lamour Y, Dutar P. Alterations in the properties of hippocampal pyramidal neurons in the aged rat. *Neuroscience.* Jun 1992;48(4):793-806.

Procter AW, Lowe SL, Palmer AM, et al. Topographical distribution of neurochemical changes in Alzheimer's disease. *J Neurol Sci.* Apr 1988;84(2-3):125-140.

Procter AW, Palmer AM, Francis PT, et al. Evidence of glutamatergic denervation and possible abnormal metabolism in Alzheimer's disease. *J Neurochem.* Mar 1988;50(3):790-802.

Pyapali GK, Turner DA. Increased dendritic extent in hippocampal CA1 neurons from aged F344 rats. *Neurobiol Aging.* Jul-Aug 1996;17(4):601-611.

Quintero JE, Day BK, Zhang Z, et al. Amperometric measures of age-related changes in glutamate regulation in the cortex of rhesus monkeys. *Exp Neurol.* Dec 2007;208(2):238-246.

Raisman G, Cowan WM, Powell TP. An experimental analysis of the efferent projection of the hippocampus. *Brain.* Mar 1966;89(1):83-108.

Rall W. Theory of physiological properties of dendrites. *Ann N Y Acad Sci.* Mar 2 1962;96:1071-1092.

Rao KS, Vinay Kumar D, Bhaskar MS, Sripad G. On the 'active' molecules of DNA-polymerase beta in aging rat brain. *Biochem Mol Biol Int.* Sep 1994;34(2):287-294.

Rao MS, Hattiangady B, Shetty AK. Status epilepticus during old age is not associated with enhanced hippocampal neurogenesis. *Hippocampus.* 2008;18(9):931-944.

Rapp PR, Gallagher M. Preserved neuron number in the hippocampus of aged rats with spatial learning deficits. *Proc Natl Acad Sci U S A.* Sep 3 1996;93(18):9926-9930.

Ravikiran A. Transformation of polishing grooves into ridges on the worn surface of alumina. *J Am Ceram Soc.* Jan 1999;82(1):261-261.

Ravikiran A. Effect of sliding conditions on formation of grain-pits due to wear anisotropy. *J Mater Sci Lett.* Jun 2000;19(12):1041-1043.

Ravikiran A. Influence of apparent pressure on wear behavior of self-mated alumina. *J Am Ceram Soc.* May 2000;83(5):1302-1304.

Ravikiran A. Wear mechanism based on wear anisotropy. *Tribol T.* Apr 2000;43(2):287-292.

Reiner A, Steiger B, Scherer GG, Wokaun A. Influence of the morphology on the platinum electrode surface activity. *J Power Sources.* May 19 2006;156(1):28-32.

Richter JD, Klann E. Making synaptic plasticity and memory last: mechanisms of translational regulation. *Genes Dev.* Jan 1 2009;23(1):1-11.

Rosenthal F. Extracellular potential fields of single PT-neurons. *Brain Res.* Jan 28 1972;36(2):251-263.

Rosenzweig ES, Barnes CA. Impact of aging on hippocampal function: plasticity, network dynamics, and cognition. *Prog Neurobiol.* Feb 2003;69(3):143-

179.

Rossell S, Gonzalez LE, Hernandez L. One-second time resolution brain microdialysis in fully awake rats. Protocol for the collection, separation and sorting of nanoliter dialysate volumes. *J Chromatogr B Analyt Technol Biomed Life Sci.* Feb 5 2003;784(2):385-393.

Rothstein JD, Martin L, Levey AI, et al. Localization of neuronal and glial glutamate transporters. *Neuron.* Sep 1994;13(3):713-725.

Rousche PJ, Pellinen DS, Pivin DP, Jr., Williams JC, Vetter RJ, Kipke DR. Flexible polyimide-based intracortical electrode arrays with bioactive capability. *IEEE Trans Biomed Eng.* Mar 2001;48(3):361-371.

Rutherford EC, Pomerleau F, Huettl P, Stromberg I, Gerhardt GA. Chronic second-by-second measures of L-glutamate in the central nervous system of freely moving rats. *J Neurochem.* Aug 2007;102(3):712-722.

Rutishauser U, Mamelak AN, Schuman EM. Single-trial learning of novel stimuli by individual neurons of the human hippocampus-amygdala complex. *Neuron.* Mar 16 2006;49(6):805-813.

Sajikumar S, Frey JU. Anisomycin inhibits the late maintenance of long-term depression in rat hippocampal slices in vitro. *Neurosci Lett.* Feb 27 2003;338(2):147-150.

Sajikumar S, Frey JU. Resetting of 'synaptic tags' is time- and activity-dependent in rat hippocampal CA1 in vitro. *Neuroscience.* 2004;129(2):503-507.

Sandison ME, Anicet N, Glidle A, Cooper JM. Optimization of the geometry and porosity of microelectrode arrays for sensor design. *Analytical Chemistry.* Nov 15 2002;74(22):5717-5725.

Saransaari P, Oja SS. Age-related changes in the uptake and release of glutamate and aspartate in the mouse brain. *Mech Ageing Dev.* Jul 14 1995;81(2-3):61-71.

Savchenko VL, McKanna JA, Nikonenko IR, Skibo GG. Microglia and astrocytes in the adult rat brain: comparative immunocytochemical analysis demonstrates the efficacy of lipocortin 1 immunoreactivity. *Neuroscience.*

2000;96(1):195-203.

Scimemi A, Schorge S, Kullmann DM, Walker MC. Epileptogenesis is associated with enhanced glutamatergic transmission in the perforant path. *J Neurophysiol.* Feb 2006;95(2):1213-1220.

Segovia G, Porras A, Del Arco A, Mora F. Glutamatergic neurotransmission in aging: a critical perspective. *Mech Ageing Dev.* Jan 2001;122(1):1-29.

Shackelford JF. Bioceramics - An historical perspective. *Mater Sci Forum.* 1999;293:1-4.

Shackelford JF. Bioceramics - Current status and future trends. *Mater Sci Forum.* 1999;293:99-106.

Shimokawa I, Higami Y, Hubbard GB, McMahan CA, Masoro EJ, Yu BP. Diet and the suitability of the male Fischer 344 rat as a model for aging research. *J Gerontol.* Jan 1993;48(1):B27-32.

Shorvon SD, Perucca E, Fish DR, Dodson E. The Treatment of Epilepsy, Blackwell Science, Oxford 2004.

Smith MA, Perry G, Richey PL, et al. Oxidative damage in Alzheimer's. *Nature.* Jul 11 1996;382(6587):120-121.

Sonnewald U, Westergaard N, Schousboe A. Glutamate transport and metabolism in astrocytes. *Glia.* Sep 1997;21(1):56-63.

Soltman D, Subramanian V. Inkjet-Printed Line Morphologies and Temperature Control of the Coffee Ring Effect. *Langmuir*, 2008, 24 (5), 2224-2231

Squire LR. Memory and the hippocampus: a synthesis from findings with rats, monkeys, and humans. *Psychol Rev.* Apr 1992;99(2):195-231.

Stensaas SS, Stensaas LJ. The reaction of the cerebral cortex to chronically implanted plastic needles. *Acta Neuropathol.* 1976;35(3):187-203.

Stephens ML, Quintero JE, Pomerleau F, Huettl P, Gerhardt GA. Age-related changes in glutamate release in the CA3 and dentate gyrus of the rat hippocampus. *Neurobiol Aging.* Jun 15 2009.

Steward O, Scoville SA. Cells of origin of entorhinal cortical afferents to the hippocampus and fascia dentata of the rat. *J Comp Neurol.* Oct 1 1976;169(3):347-370.

Suaud-Chagny MF, Cespuglio R, Rivot JP, Buda M, Gonon F. High sensitivity measurement of brain catechols and indoles in vivo using electrochemically treated carbon-fiber electrodes. *J Neurosci Methods.* Jul 1993;48(3):241-250.

Sudhof TC. The synaptic vesicle cycle. *Annu Rev Neurosci.* 2004;27:509-547.

Szapiro G, Galante JM, Barros DM, et al. Molecular mechanisms of memory retrieval. *Neurochem Res.* Nov 2002;27(11):1491-1498.

Szarowski DH, Andersen MD, Retterer S, et al. Brain responses to micro-machined silicon devices. *Brain Res.* Sep 5 2003;983(1-2):23-35.

Szerb JC, Fine A. Is glutamate a co-transmitter in cortical cholinergic terminals? Effects of nucleus basalis lesion and of presynaptic muscarinic agents. *Brain Res.* May 7 1990;515(1-2):214-218.

Takahashi T, Amano N, Asamura H, et al. Correlation between glial fibrillary acidic protein-positive astrocytes and age in the human hippocampus. *Leg Med (Tokyo).* May 2006;8(3):161-165.

Takeda A, Minami A, Sakurada N, Nakajima S, Oku N. Response of hippocampal mossy fiber zinc to excessive glutamate release. *Neurochem Int.* Jan 2007;50(2):322-327.

Thomas TC, Grandy DK, Gerhardt GA, Glaser PE. Decreased dopamine D4 receptor expression increases extracellular glutamate and alters its regulation in mouse striatum. *Neuropsychopharmacology.* Jan 2009;34(2):436-445.

Thomas TC, Kruzich PJ, Joyce BM, et al. Dopamine D4 receptor knockout mice exhibit neurochemical changes consistent with decreased dopamine release. *J Neurosci Methods.* Nov 30 2007;166(2):306-314.

Thomson AM, Bannister AP, Hughes DI, Pawelzik H. Differential sensitivity to Zolpidem of IPSPs activated by morphologically identified CA1 interneurons in slices of rat hippocampus. *Eur J Neurosci.* Feb 2000;12(2):425-436.

Turner AM, Dowell N, Turner SW, et al. Attachment of astroglial cells to microfabricated pillar arrays of different geometries. *J Biomed Mater Res.* Sep 5 2000;51(3):430-441.

Turner JN, Shain W, Szarowski DH, et al. Cerebral astrocyte response to micromachined silicon implants. *Exp Neurol.* Mar 1999;156(1):33-49.

van Elst LT, Valerius G, Buchert M, et al. Increased prefrontal and hippocampal glutamate concentration in schizophrenia: evidence from a magnetic resonance spectroscopy study. *Biol Psychiatry.* Nov 1 2005;58(9):724-730.

Vandenberghe R, Tournoy J. Cognitive aging and Alzheimer's disease. *Postgrad Med J.* Jun 2005;81(956):343-352.

Vautrin J, Barker JL. Presynaptic quantal plasticity: Katz's original hypothesis revisited. *Synapse.* Mar 2003;47(3):184-199.

Veng LM, Granholm AC, Rose GM. Age-related sex differences in spatial learning and basal forebrain cholinergic neurons in F344 rats. *Physiol Behav.* Oct 2003;80(1):27-36.

Volterra A, Steinhauser C. Glial modulation of synaptic transmission in the hippocampus. *Glia.* Aug 15 2004;47(3):249-257.

Walker MC, Ruiz A, Kullmann DM. Do mossy fibers release GABA? *Epilepsia.* 2002;43 Suppl 5:196-202.

Watson CJ, Venton BJ, Kennedy RT. In vivo measurements of neurotransmitters by microdialysis sampling. *Anal Chem.* Mar 1 2006;78(5):1391-1399.

Westerink RH. Exocytosis: using amperometry to study presynaptic mechanisms of neurotoxicity. *Neurotoxicology.* Mar 2004;25(3):461-470.

Williams GJ, Edwards MR. The Effect of Surface-Treatment on the Strength of Dental Porcelain. *J Dent Res.* Apr 1989;68(4):578-578.

Wilson NR, Kang J, Hueske EV, et al. Presynaptic regulation of quantal size by the vesicular glutamate transporter VGLUT1. *J Neurosci.* Jun 29 2005;25(26):6221-6234.

Witgen BM, Lifshitz J, Grady MS. Inbred mouse strains as a tool to analyze hippocampal neuronal loss after brain injury: a stereological study. *J Neurotrauma.* Sep 2006;23(9):1320-1329.

Witter MP. Organization of the entorhinal-hippocampal system: a review of current anatomical data. *Hippocampus.* 1993;3 Spec No:33-44.

Yasuda RP, Ikonomovic MD, Sheffield R, Rubin RT, Wolfe BB, Armstrong DM. Reduction of AMPA-selective glutamate receptor subunits in the entorhinal cortex of patients with Alzheimer's disease pathology: a biochemical study. *Brain Res.* Apr 24 1995;678(1-2):161-167.

Yuen TG, Agnew WF. Histological evaluation of polyesterimide-insulated gold wires in brain. *Biomaterials.* Aug 1995;16(12):951-956.

Zarudi I, Zhang LC, Cockayne D. Subsurface structure of alumina associated with single-point scratching. *J Mater Sci.* Mar 15 1998;33(6):1639-1645.

Zhang Y, Loonam TM, Noailles PA, Angulo JA. Comparison of cocaine- and methamphetamine-evoked dopamine and glutamate overflow in somatodendritic and terminal field regions of the rat brain during acute, chronic, and early withdrawal conditions. *Ann N Y Acad Sci.* Jun 2001;937:93-120.

Zhang Z, Yoo R, Wells M, Beebe TP, Jr., Biran R, Tresco P. Neurite outgrowth on well-characterized surfaces: preparation and characterization of chemically and spatially controlled fibronectin and RGD substrates with good bioactivity. *Biomaterials.* Jan 2005;26(1):47-61.

Zhu XO, McCabe BJ, Aggleton JP, Brown MW. Differential activation of the rat hippocampus and perirhinal cortex by novel visual stimuli and a novel environment. *Neurosci Lett.* Jun 27 1997;229(2):141-143.

Zucker RS, Regehr WG. Short-term synaptic plasticity. *Annu Rev Physiol.* 2002;64:355-405.

VITA

Name: Pooja Mahendra Talauliker

Date of Birth: 07/25/1982

Birthplace: Dubai, United Arab Emirates

Education

07/04-10/09	Doctoral degree candidate Department of Anatomy and Neurobiology The Graduate School at the University of Kentucky
05/04	Bachelor of Technology, with Honors Biotechnology and Biochemical Engineering Indian Institute of Technology, Kharagpur, India
04/00	High School Diploma Indian High School, Dubai, U.A.E

Professional Experience

05/06-05/09	Training Course Instructor Center for Microelectrode Technology (CenMeT) University of Kentucky Lexington, Kentucky

01/07-10/09	Student representative NSF Engineering Research Center University of Southern California Los Angeles, California
01/09 - 10/09	Leader and Representative Cultural Competence in Medical Education University of Kentucky College of Medicine Lexington Kentucky
01/09 - 10/09	Graduate Student Representative Diversity Advisory Committee University of Kentucky College of Medicine Lexington Kentucky
01/05 – 12/05	Member Integrated Biomedical Sciences Advisory Committee University of Kentucky Lexington Kentucky
01/03 – 04/05	Member Council for Sarojini Naidu Hall of Residence Indian Institute of Technology Kharagpur India

01/02 – 12/03	Student financial auditor Sarojini Naidu Hall of Residence Indian Institute of Technology Kharagpur India
01/00	Attendee Self-Management & Leadership Course Oxford Leadership Academy Dubai, United Arab Emirates

Scholastic and Professional Honors

03/07	Outstanding presentation award University of Kentucky Graduate Students Interdisciplinary Conference Lexington, Kentucky
03/07	Outstanding presentation award Bluegrass Society for Neuroscience Lexington, Kentucky
01/07-04/07	Teaching assistantship Department of Anatomy and Neurobiology University of Kentucky Lexington, Kentucky

08/04-12/09	Research assistantship Department of Anatomy and Neurobiology University of Kentucky Lexington, Kentucky
04/98-03/00	Merit with means Scholarship Central Board on Secondary Education, India

Publications

Book Chapters:

M.L. Stephens, D.D. Spencer, I. Cavus, M. Hsiao, D.Song, S.H. Courellis, S. A. Deadwyler, R.E. Hampson, D. Putz, J.E. Quintero, M.K. Bensalem-Owen, K.N. Hascup, E.C. Rutherford, B.K. Day, J. R. Nickell, F. Pomerleau, P. Huettl, J. J. Burmeister, P.M. Talauliker, V.Z. Marmarelis, J.J. Granacki, T. Berger, and G. A. Gerhardt. Microelectrode-based Epilepsy Therapy: A hybrid neural prosthesis incorporating seizure prediction and intervention with biomimetic maintenance of Normal hippocampal function; Computational Neuroscience in Epilepsy, Editors: I. Soltesz and K. Staley; First Edition 2008; Academic Press.

Abstracts:

Talauliker PM, Rutherford EC, Pomerleau F, Huettl P, Hastings JT, Gerhardt GA. Surface Analysis of Ceramic- Based MEAs using Scanning Electron Microscopy. Society for Neuroscience Annual Meeting, Washington, D.C., Nov 2005.

Talauliker PM, Rutherford EC, Pomerleau F, Huettl P, Hastings JT, Gerhardt GA. Surface analysis of enzyme- based MEAs. Bluegrass Society for Neuroscience, Lexington, Kentucky, Mar 2006.

Talauliker PM, Rutherford EC, Pomerleau F, Huettl P, Hastings JT, Gerhardt GA. Analysis of ceramic- based MEAs using scanning electron microscopy. Translational Neuroscience: Conference on RNA Therapy for Neurodegenerative Disorders, Lexington, Kentucky, Apr 2006.

Talauliker PM, Rutherford EC, Pomerleau F, Huettl P, Stephens ML, Hastings JT, Gerhardt GA. MEA Studies of L-Glutamate Dynamics in the Rodent Hippocampus. In Vivo Methods in Neuroscience, Sardinia, Italy, May 2006.

Stephens ML, Quintero J, Talauliker PM, Pomerleau F, Huettl P, Gerhardt GA. Second-by-second glutamate recordings in the CA1 and CA3 regions of the young rats. Monitoring Molecules: In Vivo Methods in Neuroscience, Sardegna, Italy, May 2006.

Talauliker PM, Rutherford EC, Pomerleau F, Huettl P, Stephens ML, Hastings JT, Gerhardt GA. Multisite MEA studies of L-glutamate dynamics in the rodent hippocampus. Monitoring Molecules: In Vivo Methods in Neuroscience, Sardegna, Italy, May 2006

Gerhardt GA, Rutherford EC, Hascup KN, Quintero JE, Talauliker PM, Thomas TC, Stephens ML, Fuqua J, Coates TD, Burmeister JJ, Pomerleau F, Huettl P. Second-by-second measurements of L-glutamate and other neurochemicals in the CNS of animal models and humans. Institute for Biological Engineering Conference, St. Louis, Missouri, Mar 2007.

Talauliker PM, Rutherford EC, Pomerleau F, Huettl P, Hastings JT, Gerhardt GA. Evaluation of ceramic-based MEAs for in vivo recordings. Institute for Biological Engineering Conference, St. Louis, Missouri, Mar 2007.

Talauliker PM, Rutherford EC, Pomerleau F, Huettl P, Stephens ML, Hastings JT, Gerhardt GA. Multisite MEA studies of L-glutamate in the rat hippocampus. Bluegrass Society for Neuroscience Day, Lexington, Kentucky, Mar 2007.

Geddes JJ, Talauliker PM, Pomerleau F, Huettl P, Gerhardt GA. Characterization of a novel microelectrode for subregional recordings in the rat hippocampus. Bluegrass Chapter of Society for Neuroscience Day, Lexington, Kentucky, Mar 2007.

Talauliker PM, Rutherford EC, Pomerleau F, Huettl P, Stephens ML, Hastings JT, Gerhardt GA. MEA-based studies of L-glutamate dynamics in the rodent hippocampus. University of Kentucky Graduate School Interdisciplinary Conference, Lexington, Kentucky, Apr 2007.

Talauliker PM, Pomerleau F, Huettl P, Gerhardt GA. Second by second comparisons of Subregional glutamate in the rat hippocampus. Bluegrass Chapter of Society for Neuroscience Day, Lexington, Kentucky, Mar 2008.

Talauliker PM, Pomerleau F, Huettl P, Gerhardt GA. Subregional differences in hippocampal glutamate neurotransmission in Fischer 344 rats. Monitoring Molecules: In Vivo Methods in Neuroscience, Vancouver, British Columbia, Aug 2008.

Gerhardt GA, Pomerleau F, Huettl P, Hascup E, Hascup K, Talauliker PM, Quintero JE, Stephens ML, Burmeister JJ. Real-time measurements of neurotransmission *in vivo* using MEAs. Monitoring Molecules: In Vivo Methods in Neuroscience, Vancouver, British Columbia, Aug 2008.

Talauliker PM, Powell EJ, Coates TD, Pomerleau F, Huettl P, Gerhardt GA. Optimization of enzyme-based MEAs for rapid neurochemical measurements in the CNS. Society for Neuroscience, Lexington, Kentucky, Mar 2009.

Presentations

Talauliker PM. Plant-based inhibitors for Mammalian Matrix Metalloproteinases. Center for Biotechnology Dissertation Seminar, Indian Institute of Technology, Kharagpur, India, Apr 2004.

Talauliker PM. Dynamics & Regulation L-Glutamate in the Hippocampus of Animal Model of Epilepsy, Department of Anatomy and Neurobiology Seminar Series, University of Kentucky, Dec 2005.

Talauliker PM. RNAi: Future Outlook, Career Prospects and Investment Strategies, Department of Anatomy and Neurobiology Seminar Series, University of Kentucky, Apr 2006.

Talauliker PM. Evaluation of ceramic-based MEAs for *in vivo* recordings. Institute for Biological Engineering Conference, St. Louis, Missouri, Mar 2007.

Talauliker PM. Performance analysis of chronically implanted MEAs. Annual student retreat: Biomimetic Microelectronic Systems Engineering Research Center Student Retreat, Los Angeles. California, Apr 2007.

Talauliker PM. Subregional Glutamate Neurotransmission in the Anesthetized Rat Hippocampus. Department of Anatomy and Neurobiology Retreat, Lexington, Kentucky, Jun 2008.